

# Efficiency of RF plasma generation for fusion relevant ion sources

## Dissertation

zur Erlangung des akademischen Grades

Dr. rer. nat.

eingereicht an der

Mathematisch-Naturwissenschaftlich-Technischen Fakultät  
der Universität Augsburg

von

**David Rauner**

Augsburg, Juni 2018



Tag der mündlichen Prüfung: 22.11.2018

Erster Gutachter: apl. Prof. Dr.-Ing. U. Fantz

Zweiter Gutachter: Prof. Dr. W. Brütting

# Contents

<b>1</b>	<b>Introduction</b>	<b>5</b>
<b>2</b>	<b>Ion sources for negative hydrogen ions</b>	<b>9</b>
2.1	Production of negative ions in RF driven sources . . . . .	12
2.2	Requirements of ion sources in view of ITER and DEMO . . . . .	15
2.3	Investigation of the plasma generation efficiency at laboratory scale	17
<b>3</b>	<b>Properties of low pressure low temperature hydrogen plasmas</b>	<b>21</b>
3.1	General plasma characteristics . . . . .	21
3.2	Atomic and molecular properties of hydrogen isotopes . . . . .	26
3.3	Plasma processes . . . . .	29
3.4	Particle diffusion and balances . . . . .	35
3.5	Particle motion in a static magnetic field . . . . .	41
<b>4</b>	<b>RF plasma heating and power transfer mechanisms</b>	<b>45</b>
4.1	Impedance matching and RF power transfer efficiency . . . . .	45
4.2	Inductive heating . . . . .	48
4.3	Low field wave heating . . . . .	56
4.3.1	Helicon and Trivelpiece-Gould waves . . . . .	56
4.3.2	Antenna coupling and heating mechanism . . . . .	60
<b>5</b>	<b>Experimental setup and diagnostics</b>	<b>65</b>
5.1	The CHARLIE experiment . . . . .	65
5.2	Applied diagnostics . . . . .	70
5.2.1	Measurement of the RF power transfer efficiency . . . . .	70
5.2.2	Optical emission spectroscopy (OES) . . . . .	73
5.2.3	Floating double probe . . . . .	81
<b>6</b>	<b>Experimental approach and boundary conditions</b>	<b>87</b>
6.1	Impedance matching and discharge ignition . . . . .	87

---

6.2	Discharge operation, temporal stability and reproducibility . . . .	90
<b>7</b>	<b>Inductive discharges at 1 MHz</b>	<b>95</b>
7.1	RF power transfer efficiency . . . . .	95
7.2	Plasma characterization and heating mechanism . . . . .	97
7.2.1	Relative spatial plasma profiles . . . . .	97
7.2.2	Plasma parameters at varying pressure and RF power . . .	100
7.2.3	Inductive heating mechanism . . . . .	102
7.3	Isotopic effects: comparison of hydrogen and deuterium . . . . .	106
<b>8</b>	<b>Inductive discharges at varying excitation frequency</b>	<b>111</b>
8.1	RF power transfer efficiency . . . . .	111
8.2	Plasma parameters and heating mechanism . . . . .	114
8.2.1	Relative spatial plasma profiles . . . . .	114
8.2.2	Plasma parameters at varying pressure . . . . .	116
8.2.3	Inductive heating mechanism . . . . .	117
8.3	Assessment of an application to RF driven ion sources . . . . .	121
8.4	Effects of an external magnetic field . . . . .	127
<b>9</b>	<b>Discharges generated by a Nagoya-type helicon antenna</b>	<b>129</b>
9.1	Inductive operation without external magnetic field . . . . .	129
9.2	Discharge operation with external magnetic field . . . . .	131
9.2.1	RF power transfer efficiency . . . . .	132
9.2.2	Relative spatial plasma profiles . . . . .	133
9.2.3	Plasma parameters at varying pressure and magnetic field	136
9.2.4	RF heating by propagating waves . . . . .	140
9.2.5	Atomic density and dissociation balance . . . . .	144
9.3	Assessment of an application to RF driven ion sources . . . . .	148
<b>10</b>	<b>Summary</b>	<b>155</b>
	<b>Bibliography</b>	<b>163</b>
	<b>Acknowledgements</b>	<b>175</b>

# 1 Introduction

In view of a growing global energy demand, harnessing nuclear fusion as an energy source is an appealing prospect. The fusion experiment ITER aims to demonstrate the technological and scientific feasibility of a positive power balance via the thermonuclear fusion within a magnetically confined plasma. It is intended as an intermediate step towards a fusion power plant and will be followed by the DEMONstration power plant DEMO, envisaged to be the first fusion device to actually generate net electricity.

To achieve the high plasma temperatures ( $> 10^8$  K) required to sustain the fusion process in these devices, powerful heating systems such as the neutral beam injection based on negative ions (NNBI) are required. This system works as follows: in an ion source operating a low pressure deuterium plasma, negative deuterium ions are created. The negative ions are extracted, accelerated, subsequently neutralized and then injected into the fusion plasma, providing both heating power and the capability to externally drive a plasma current. For ITER, beams with a particle energy of 1 MeV and an accelerated ion current of 40 A have to be provided for pulse lengths of up to one hour. In view of DEMO, demands corresponding to or even exceeding the ITER parameters are expected. In particular, a higher pulse length of at least two hours and an increased wall-plug efficiency of the NNBI system up to 60% will be required. In addition, a high reliability of the reactor and all its sub-systems is a key issue, since DEMO is intended as a prototype for a fusion power plant. Hence, the NNBI systems have to rely on reliable sources for negative ions which are capable to meet these demands.

At NNBI ion sources for ITER, inductively coupled plasmas (ICPs) in  $D_2$  at a pressure of 0.3 Pa will be operated within so-called drivers, where electron densities of the order of  $10^{18} \text{ m}^{-3}$  and electron temperatures around 10 eV are reached. One source will comprise eight drivers, each supplied with an RF power up to 100 kW at an excitation frequency of 1 MHz in order to achieve the required parameters. Such a high power level poses strong demands on the RF generators and circuits and may thus limit the long term reliability of the ion source. In view of DEMO, it is therefore highly beneficial to reduce the RF power consumption, while retaining

the plasma parameters relevant for an efficient negative ion production. The latter mainly comprise a high density of both positive ions and atoms, which serve as reactants in the surface conversion process utilized to generate negative ions. In addition, a high RF power transfer efficiency is a prerequisite, which implies that a high fraction of the electrically provided RF power is coupled to the plasma itself, while the heat loads within the RF system due to ohmic losses - potentially limiting the reliability of the source - are low.

In this context, alternatives to ICPs driven at 1 MHz which are considered promising in view of an efficient plasma generation at ion sources are fundamentally assessed. Apart from deuterium, these investigations are also conducted in hydrogen, since ion source test beds are frequently operated in H<sub>2</sub> as well, mainly for diagnostic purposes. The main framework of the followed approach is that the general concept of the ITER ion source may not be fundamentally altered. This ensures an envisaged high return of experience from ITER NNBI to DEMO. Two alternative plasma generation methods are specifically considered: the first one are ICPs driven at a higher frequency. Investigations conducted in noble gases have shown that the excitation frequency can strongly affect the power absorption by the plasma. However, the driving frequency of the inductively heated ion source H<sub>2</sub>/D<sub>2</sub> plasma has never been specifically optimized regarding an efficient production of negative ions. The second assessed concept are helicon discharges operated at low magnetic fields ( $\leq 12$  mT), which rely on plasma heating via propagating electromagnetic waves. Due to their capability to reach high plasma densities with relatively moderate RF power at low pressures, they have raised interest regarding an application at ion sources for fusion among several groups. However, at conditions relevant for RF driven ion sources for NNBI, no investigations have been reported up to now which were capable to demonstrate the efficiency of H<sub>2</sub>/D<sub>2</sub> helicons in direct and quantitative comparison to ICPs.

Performing such a fundamental assessment directly at a large ion source experiment is not feasible due to the lack of flexibility and diagnostic access, though. The investigations within this work are therefore conducted at a versatile, small-scale laboratory setup which is operated at lower RF powers than ion sources. It can be equipped with a helical coil for inductive heating or with a Nagoya type-III antenna for low-field helicon operation, without changing the general discharge geometry. RF generated plasmas applying excitation frequencies between 1 and 4 MHz and RF powers up to 2 kW in H<sub>2</sub> and D<sub>2</sub> at operational

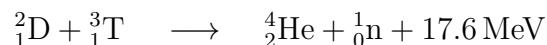
conditions relevant for ion sources are considered. Due to its comprehensive diagnostic setup, the RF power transfer efficiency and discharge parameters most crucial for an efficient and reliable plasma generation in view of ion sources for NNBI are accessible. This allows for a direct comparison of the proposed alternative plasma generation techniques to the baseline case of ICPs driven at 1 MHz and thus, for an assessment of their potential to reduce the RF power consumption.

The final aim of this fundamental approach is to identify whether any of the proposed alternative methods is promising enough to qualify for a further assessment and application at a larger scale. In order to ensure the resilience of such an evaluation, the fundamentals of the different heating mechanisms in the light molecular gases  $\text{H}_2/\text{D}_2$  need to be analysed thoroughly. Such has never been conducted up to now, since the basic characteristics of low pressure low temperature plasma heating are typically investigated in noble gas discharges like argon. In course of these novel studies, the dependences of the main discharge parameters on operational parameters like pressure, RF power and external magnetic field are regarded, with a particular focus on the isotopic differences between hydrogen and deuterium with respect to the plasma heating mechanisms.



## 2 Ion sources for negative hydrogen ions

The thermonuclear fusion of deuterium and tritium within a magnetically confined plasma is considered to be one of the most promising concepts aiming for future power generation via nuclear fusion. By heating up a plasma to temperatures of  $10^8$  K, the desired process



is taking place in sufficient amount [SCM<sup>+</sup>07]. The required magnetic confinement of such a plasma can be achieved in toroidal devices, whereas two basic experimental concepts are followed that are illustrated in figure 2.1: the tokamak and the stellarator. Tokamaks rely on the transformer principle, where the plasma itself serves as the secondary winding: by applying a current ramp through the central solenoid, a toroidal plasma current is driven. This current generates a transient poloidal magnetic field superimposing the constant toroidal magnetic field created via external magnetic field coils, which results in the desired magnetic confinement of the plasma. However, if the toroidal plasma current is only driven inductively, a tokamak can only be operated in a pulsed mode - an apparent drawback with respect to its intended application as a future power plant. In contrast to that, the particularly tailored geometry of the external magnetic field coils of a stellarator allows for a confinement without the requirement of a toroidal plasma current. This allows for steady state operation, but breaks the continuously rotational symmetry of the plasma and results in a significantly increased geometric complexity of the whole device. Therefore, the development of stellarators is currently still less progressed in comparison to tokamaks.

In order to achieve the required temperatures for a sufficient rate of the fusion process, both stellarators and tokamaks rely on external heating systems. Besides electron cyclotron resonance heating (ECRH) and ion cyclotron resonance heating (ICRH), the neutral beam injection (NBI) is of central importance. Not only

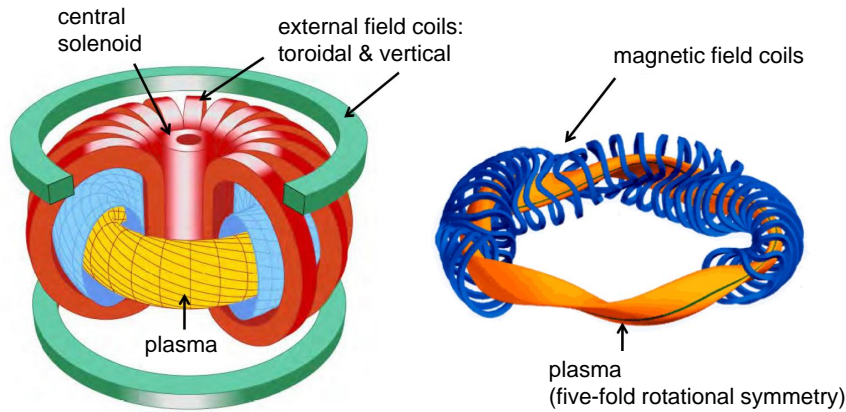


**Figure 2.1:** Schematic illustration of the typical geometry of a tokamak (left) and a stellarator (right) and the external magnetic coils required for the plasma confinement.

does it provide heating, but also the possibility to drive a toroidal plasma current externally, which is a vital ability especially for a tokamak in order to extend its limited pulse length. Therefore, NBI will also be a key system for the ITER fusion device<sup>1</sup>, which is currently build in Cadarache, France and will be, upon completion, the world’s largest tokamak. ITER is foreseen to start first plasma operation in 2025 and is intended to demonstrate the scientific and technological feasibility of a positive power balance via nuclear fusion [SCM<sup>+</sup>07, IAE02]. In order to achieve an envisaged pulse length of one hour, ITER will be supplied by two NBI systems, providing a total power of 33 MW for plasma heating and current drive [IAE02].

The first fusion device which is planned to actually generate net electricity will be the DEMONstration reactor DEMO [RBB<sup>+</sup>12], which is forseen to be the last step towards a commercial fusion power plant. With DEMO being still in the conceptual design status, presently two different scenarios are under consideration: either a pulsed, or a fully cw (continuous wave) driven device [FBB<sup>+</sup>15, FBB<sup>+</sup>16]. Depending largely on the individual scenario, different requirements for the envisaged heating and current drive systems arise that define present research and development needs [SBJ<sup>+</sup>12, FF13, McA14, SAB<sup>+</sup>17, FHF<sup>+</sup>18]. If applied at DEMO, the NBI system is foreseen to be based to a large extend on the design

<sup>1</sup>latin for *the way*

---

and technology of the ITER NBI. A general roadmap for DEMO has been established in 2012 [RBB<sup>+</sup>12], which is currently under revision to ensure the coherence with the timeline of ITER.

### Neutral beam injection

NBI heating of a fusion plasma is based on the injection of a high energetic particle beam consisting of hydrogen or deuterium atoms. As NBI systems are typically required to operate both isotopes, only hydrogen will be mentioned in the following if no distinctive isotopic difference has to be taken into account. Experimentally, this neutral hydrogen beam is produced as follows: First, positive or negative ions are created within an ion source operating a low pressure low temperature hydrogen plasma. The charged particles are subsequently extracted and accelerated to the required energies by an electrostatic multi-grid system. In order to be able to penetrate the magnetic structure of the fusion device itself, the ion beam is neutralized via charge exchange collisions within a gas target. The neutral particle beam is then injected into the fusion plasma, where the hydrogen atoms get confined after charge exchange and ionizing collisions and provide the desired heating and, particularly if injected tangentially, also the additional toroidal current drive.

Most of the presently operating fusion devices are utilizing NBI systems solely based on positive ions. However, in these cases the achieved particle energies are relatively moderate: at the up-to-date largest tokamak system JET (**J**oint **E**uropean **T**orus) for example, particle energies of up to 125 keV have been achieved with a total beam power of 34 MW delivered in short pulses within the range of several seconds [AJS<sup>+</sup>15]. However, for ITER and DEMO the NBI systems have to deliver the same or even higher total injected powers for up to one hour at particle energies until 1 MeV. At such an energy, the neutralization efficiency of positive hydrogen and deuterium ions by charge exchange collisions drops significantly to values below 10% [BPS75], which limits the achievable overall efficiency of the NBI system. Negative hydrogen ions ( $H^-$ ) on the other hand maintain a relatively high neutralization efficiency of about 60% even at high energy [BPS75], due to the weak affinity of the second electron of only 0.75 eV. At ITER, and analogously also at DEMO, the neutral beam injection systems will therefore rely on negative ions (NNBI) [IAE02, FBB<sup>+</sup>15, FBB<sup>+</sup>16]. However, the higher neutralization efficiency of negative hydrogen ions comes at the price of an increased complexity for the ion source and the extraction system. While positive

ions can be efficiently created by ionizing electron collisions in low pressure low temperature plasmas, negative hydrogen ions require additional measures to be produced sufficiently. In addition, they suffer a high destruction rate due to the low binding energy of the additional electron and when extracted from the ion source, electrons are inevitably co-extracted.

## 2.1 Production of negative ions in RF driven sources

To illustrate how negative ions can be efficiently produced in RF driven ion sources for NNBI, a brief overview of the main processes of negative ion formation is provided<sup>2</sup>. The formation processes of negative ions can be separated into two main regimes: the *volume production* and the *surface production*.

In the plasma volume,  $H^-$  is created via *dissociative attachment* of slow electrons ( $T_e \leq 1$  eV) to vibrationally excited hydrogen molecules<sup>3</sup>. In contrast to that, the *surface production* denotes the conversion of hydrogen atoms (H) and positive hydrogen ions ( $H_x^+$ ,  $x = 1, 2, 3$ ) to negative hydrogen ions at a plasma facing surface. The probability of this process is highly depending on the velocity of the impinging plasma particles as well as on several surface characteristics, but first and foremost its work function. Once  $H^-$  is created and enters the bulk plasma, a variety of processes can lead to its subsequent destruction: the most important ones are collisions with positive ions, hydrogen atoms and with fast electrons.

Experimentally, utilizing solely the volume production of negative ions alone has proven to be insufficient to achieve the requirements for a NNBI systems for ITER or DEMO [SFF<sup>+</sup>06]. Therefore, ion sources have to rely on the surface production of  $H^-$ .

### The RF driven prototype source for negative ions

Figure 2.2 shows the RF driven prototype source for ITER NNBI, which was developed at Max-Planck-Institut für Plasmaphysik (IPP) in Garching. It is described in detail in [SFF<sup>+</sup>06] and has 1/8 of the extraction area of the ion source

<sup>2</sup>Detailed information about the production and destruction processes of negative hydrogen ions in a low pressure plasma can be found for example in [Bac06].

<sup>3</sup>Conventionally, the temperature  $T$  denotes the corresponding energy equivalent  $k_B T$  ( $k_B$  is the Boltzmann constant) and is given in units of eV.

to be applied at ITER [HDG<sup>+</sup>09, IAE02]. In general, it consists of three different regions:

Within the plasma heating regime, commonly referred to as the *driver*, a low pressure (0.3 Pa) hydrogen plasma is generated via inductive coupling at 1 MHz at an RF power of up to 100 kW utilizing an external helical coil. The cylindrical driver vessel mainly comprises of a metallic backplate, a dielectric tube (typically made of quartz or Al<sub>2</sub>O<sub>3</sub>) and a Faraday screen in order to suppress capacitive coupling and shield the dielectric vessel from fast ions. Within the driver, high electron densities ( $n_e \geq 10^{18} \text{ m}^{-3}$ ) and electron temperatures ( $T_e \geq 10 \text{ eV}$ ) are present [FFF<sup>+</sup>06, MDCK<sup>+</sup>09]. At such parameters, a significant dissociation of molecular hydrogen to atoms due to collisions with electrons is achieved. The ratio  $n_{\text{H}}/n_{\text{H}_2}$  of the atomic and molecular densities reaches values of the order of 0.3 to 0.6, implying that the atomic density  $n_{\text{H}}$  is of the order of  $10^{18} - 10^{19} \text{ m}^{-3}$  [FSW<sup>+</sup>13]. The plasma generated in the driver expands into the *expansion region* where it passes a magnetic filter field of the order of a several mT. Due to this field, both the electron temperature and density of the expanding plasma are reduced [SMF<sup>+</sup>12]. Thereby, the probability for the destruction of negative hydrogen ions by fast electrons is significantly reduced, which provides favourable conditions for an efficient production of H<sup>-</sup>. Passing the expansion region and the filter field, the plasma reaches the plasma grid (PG), which is the first grid of a multi-grid system constituting the *extraction region* where a negative hydrogen ion beam is extracted via multiple apertures.

The actual production of negative ions occurs on the plasma grid. For an efficient surface production of negative ions, the work function of the converter surface (the PG) has to be very low. This is achieved by utilizing caesium, which has a work function of 2.14 eV considering the bulk material [Lid05]. The required Cs is constantly evaporated into the source volume by a Cs oven and subsequently deposited on the walls of the source and on the plasma grid in order to reduce its work function. Positive hydrogen ions and hydrogen atoms originating from the driver region hit the PG and are converted to negative ions with a high conversion probability [LS92, SCI<sup>+</sup>96, IKS92]. Due to the magnetic filter field, the H<sup>-</sup>-destruction rate in the plasma in front of the PG is low enough to provide sufficiently long lifetimes of the created negative ions, allowing them to reach the apertures of the PG where they are extracted.

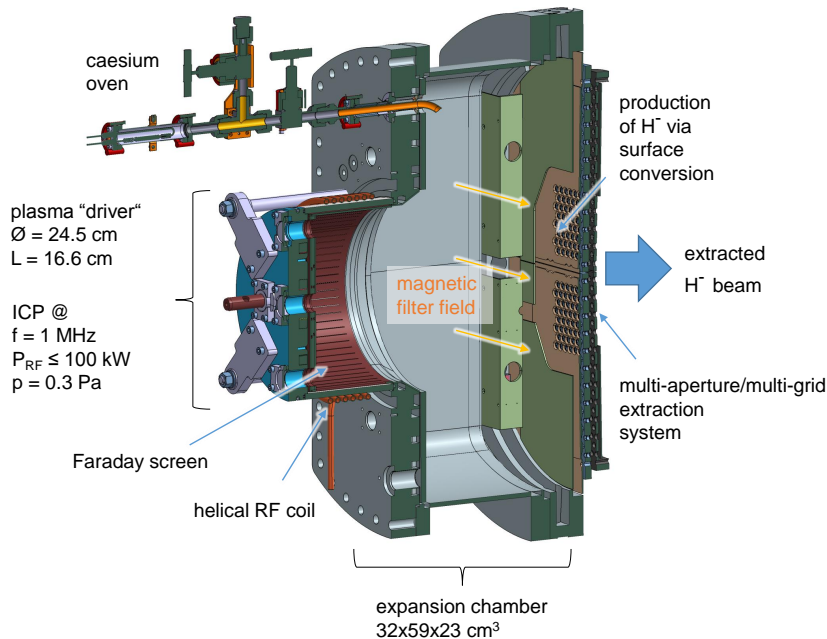


**Figure 2.2:** Scheme of the RF driven prototype ion source for ITER NNBI.

### Figures of merit of the driver plasma

Modelling of the positive ion and atom transport onto the PG at the typical source parameters has shown that the conversion of atoms is expected to be the dominating production process of  $H^-$  [WGF09, WSM<sup>+</sup>12]: the surface conversion rate of H is approximately four times higher than for the ions. However, the conversion of atoms to negative ions at the PG leads to the build up of a negative space charge in front of the grid. This results in a potential well, which hinders negative ions of leaving the surface in order to reach the extraction apertures and thus, effectively limits the extracted negative ion current. To compensate for the space charge limitation of the  $H^-$  emission from the surface, a high positive hydrogen ion density near the PG is required [WGF09].

The main task of the driver plasma is therefore to deliver a high flux of both positive ions and hydrogen atoms towards the PG. Hence, the crucial parameters in the driver bulk plasma are the electron density  $n_e$  and the atomic density  $n_H$ : On the one hand, a high electron density implies a high positive ion density due to the quasineutrality of the plasma. On the other hand, a high  $n_e$  is a prerequisite to reach high atomic fractions since atoms are mainly produced via electron impact dissociation of molecules. The quantities  $n_e (= n_{ion})$  and  $n_H$  are therefore considered to be the the main figures of merit of the driver plasma.

In addition to those, the so-called *RF power transfer efficiency*  $\eta$  is of central importance: it quantifies how much of the RF power delivered by the generator is actually deposited in the plasma itself, compared to power losses within the RF system due to ohmic heating. The knowledge of  $\eta$  provides valuable information to describe and assess the efficiency of the plasma heating and its dependence on external operational parameters like RF power and pressure. In addition, it allows to directly quantify the power losses within the RF system, which demand for cooling measures and directly influence the reliability of the ion source. In summary, the provision of high electron and atomic densities in combination with a high RF power transfer efficiency can therefore be generally considered as an “efficient” plasma generation regarding the requirements of an ion source for NNBI.

## 2.2 Requirements of ion sources in view of ITER and DEMO

At ITER, the NNBI system will comprise of two separate beamlines, each with a heating power of 16.5 MW at a beam energy of 1 MeV per D atom [IAE02]. To reach these parameters, an accelerated negative ion ( $D^-$ ) current of 40 A is required per beamline. For the steady state operation of ITER, a homogeneous neutral beam with the posed parameters has to be stably delivered for one hour. In order to satisfy these requirements, specific boundary conditions for the operation of the ion source arise:

Firstly, the maximum filling pressure within the source has to be limited to a value of 0.3 Pa to reduce stripping losses during beam acceleration. Secondly, the plasma admission onto the PG (which is of a size of  $1.9 \times 0.9 \text{ m}^2$  at ITER NNBI) has to be as uniform as possible to ensure an equally uniform  $H^-$  production and hence, a homogeneous beam. Thirdly, the ratio between the co-extracted electron current density and the extracted negative deuterium current density has to be smaller than unity, since the implicit co-extraction of electrons requires their deflection within the grid system leading to an associated heat load.

Regarding DEMO, the NNBI system design studies are favoured to be as much as possible based on the ITER NNBI in order to ensure an optimum *return of experience* [RBB<sup>+</sup>12, FBB<sup>+</sup>16]. Accordingly, the described requirements may be considered at least as the minimal requirements for DEMO. However, additional requirements for the operation of NNBI arise in the latter case, which depend largely on the discussed scenario [SAB<sup>+</sup>17, FHF<sup>+</sup>18]:

- The envisaged total injected power is increased to a range between 50 MW (pulsed scenario) and 135-200 MW (cw scenario) at beam energies between 0.8 and 1 MeV.
- The pulse lengths are prolonged since either a fully cw operation or at least 2 hour pulses are required.
- The NNBI system for DEMO is required to achieve a high wall-plug efficiency between 40 % (pulsed) and 60 % (cw), which is a significant increase compared to the approximated 26 % at ITER [SAB<sup>+</sup>17].
- In addition, it is recently discussed that the NNBI system for DEMO may have to be operated with an even lower source filling pressure of 0.2 Pa [SAB<sup>+</sup>17].

In order to fulfill these additional demands, all components of the NNBI system have to be reviewed for DEMO. An overview of the associated research and development needs and the followed concepts are for example provided by [SAB<sup>+</sup>17]. The specific requirements regarding the RF plasma generation within the ion source are further assessed in the following.

Considering the ITER scenario as the starting point, an RF power of 100 kW per driver will be applied to for the plasma heating, adding up to a total RF power of about 800 kW per beamline where 8 individual drivers illuminate the large area of the PG. At DEMO, the required power may exceed these values due to the possibility that a lower operating pressure is required. In general, such a high level of RF power poses strong demands on the components of the RF circuit, since high alternating currents and voltages are present. Due to the high currents, considerable ohmic losses arise which require for intense cooling measures. The occurrence of high voltages demands for sophisticated and robust insulation measures in order to avoid breakdowns and arcing, i.e. between the coil windings. In summary, a high RF power requires for substantial countermeasures and dedicated maintenance efforts in order to ensure the reliability of the ion source. This is generally critical in view of DEMO though, since the NNBI system has to fulfil the so-called RAMI issues, which implies the provision of a high reliability, availability, maintainability and a facilitated inspectability [FBB<sup>+</sup>15, FBB<sup>+</sup>16, FAA<sup>+</sup>17].

It would therefore be highly beneficial to reduce the amount of RF power required for the plasma generation, while retaining the plasma parameters relevant

for negative ion production. Apart from an envisaged higher reliability of the source, this would also entail an increase of the wall-plug efficiency of the NNBI system. However, this can only be considered as a favourable side effect, since the share of the RF power in the total required power for NNBI is in the range of about 1-2%. A practical possibility to reduce the RF power consumption of the ion source is to increase the efficiency of the plasma generation itself. This imposes the necessity of assessing alternative RF plasma generation techniques regarding their potential application at ion sources.

## **2.3 Investigation of the plasma generation efficiency at laboratory scale**

The aim of this work is to investigate promising alternatives for the currently applied ICPs driven at 1 MHz and assess their potential regarding a reduced RF power consumption at ion sources. The main boundary condition of the present approach is that the basic geometry and concept of the ion source is not fundamentally changed with respect to the prototype source for ITER, in order to ensure the envisaged technology and experience transfer from ITER to DEMO. Within this work, two different alternatives are specifically investigated:

### **Inductive heating at a different excitation frequency**

The first possibility which is assessed is inductive heating at a different excitation frequency. The currently applied frequency of 1 MHz is a remnant from RF driven sources for positive ions, where it has been proven to be a sufficient and reliable choice [SCF<sup>+</sup>99]. However, the particular influence of the excitation frequency on the plasma parameters of the driver plasma and its figures of merit regarding the H<sup>-</sup> production has never been specifically optimized. The excitation frequency of inductive discharges is well known to influence the power absorption by the plasma and thus the RF power transfer efficiency [LL05, CB11], which has been reported for noble gas ICPs various times [PGA92, EB04, LL05, KRP<sup>+</sup>16]. This correlation is caused by the dependence of the power absorption capabilities of a low pressure discharge on the frequency dependent plasma conductivity, which is further influenced by the applied gas type and pressure. However, the frequency dependent plasma generation efficiency of ICPs has never been experimentally investigated for deuterium or hydrogen discharges at the ion source relevant low pressure of 0.3 Pa.

### Wave heated “helicon” discharges

The second alternative to be assessed are RF discharges heated by propagating waves, which are commonly referred to as helicon discharges. In the presence of a static magnetic field, so-called helicon wave modes can be excited to propagate within a low pressure plasma applying an RF signal in the MHz range via specifically tailored antennas [BC97b, CB97, Che15]. Due to an interaction of these waves with the plasma electrons, very high plasma densities at relatively moderate RF powers can be achieved at pressures below 1 Pa. Typically, helicon discharges are operated in noble gases (mostly argon) within long cylindrical tubes applying axial magnetic fields ranging from a few up to several 100 mT. At these parameters, they have been extensively studied and are applied for example in semiconductor manufacturing and ion thruster systems for space propulsion. Generally, helicon discharges can also be efficiently operated at low magnetic fields of a few mT, even though the achievable plasma density is generally lower in this case due to a reduced magnetic confinement of the plasma. In this low field regime, a prominent feature of helicon discharges is known to occur: the so-called low field peak, which describes a local enhancement of the RF power transfer efficiency or the electron density at certain magnetic fields [Che92, Cho06].

Within the recent years, an increasing number of experiments have shown that helicon discharges can be efficiently used to reach high densities also in light molecular gases like hydrogen or deuterium: applying magnetic fields up to 1 T and RF powers of several 10 kW at a pressure around 1 Pa, the achievement of electron densities of up to  $10^{19} \text{ m}^{-3}$  and simultaneously low electron temperatures ( $\approx 5 \text{ eV}$ ) has been reported several times, foremost by experiments aiming for an investigation of plasma-material interactions like MAGPIE [BCS<sup>+</sup>12, CB16] or Proto-MPEX [GCR<sup>+</sup>17]. Due to their capability to reach high plasma densities at low pressure and low electron temperatures, the utilization of helicon discharges at ion sources for NNBI appears as a promising alternative for inductive plasma generation. However, an application of high magnetic fields of several 100 mT is not feasible at an ion source for NNBI: the transient magnetic fields of a high-field helicon discharge are strong enough to modify the magnetic fields patterns within the ion extraction and acceleration region of the source, which needs to be avoided. Helicon discharges operated at low or moderate magnetic fields in hydrogen and deuterium which may potentially exploit the low-field peak phenomenon therefore appear as the most promising candidate for a further assessment, and are hence investigated within this work.

Before the specific approach followed in this work is described, a short overview about recent research and development activities is provided. Investigations aiming for the assessment of an application of low field helicons at ion sources have been reported by different groups, mostly in the low power range. In hydrogen discharges generated at the MAGPIE plasma device at magnetic fields up to 8.5 mT, an RF power of 1 kW ( $f = 13.56$  MHz) and a pressure of 1.33 Pa the occurrence of a peak of the electron density ( $\approx 10^{17} \text{ m}^{-3}$ ) at roughly 3 mT has been observed [SMO<sup>+</sup>15]. Similar results at comparable parameters were achieved at a precursory version of the experimental setup utilized in this work and are reported by [BGR<sup>+</sup>16]. Up to now, the probably most advanced investigations regarding ion sources driven by low-field helicons were performed at the RAID experiment [FAF<sup>+</sup>17, MAD<sup>+</sup>17]. Applying an RF power of 5 kW ( $f = 13.56$  MHz) and a magnetic field of 15 mT at the ITER relevant pressure of 0.3 Pa, H<sub>2</sub> and D<sub>2</sub> discharges were observed to achieve electron densities up to  $10^{18} \text{ m}^{-3}$  at electron temperatures around 5 eV. Towards the parameters required at ion sources, this already appears as a very promising result. However, the plasma generated at RAID forms a long ( $\approx 1.5$  m) and relatively narrow (diameter  $\leq 0.1$  m) column. Such a plasma geometry is not compatible with the geometry of the ITER relevant ion sources, which require a homogeneous plasma admission onto the large extraction grids. The discharges generated by RAID are therefore envisaged to be applied as a part of a whole new ion source and injector concept, known as Cybele [SAB<sup>+</sup>16]. Therefore, these investigations follow a fundamentally different approach than the current work, which aims for a high return of experience from ITER NNBI, as already stated above.

### Present experimental approach

Within this work, two possible alternatives to the currently utilized inductive plasma heating at 1 MHz are fundamentally assessed: ICPs driven at a different (higher) excitation frequency and low-field helicon discharges. Performing such an assessment directly at a large scale ion source is not feasible due to a lack of flexibility and diagnostic access, though. The investigations are therefore conducted at the laboratory experiment CHARLIE, which is described in detail in chapter 5.1.

Due to its flexibility, the experiment can be equipped with different antennas while retaining the geometry of the plasma vessel. In the present case, a helical coil for inductive plasma heating and a Nagoya type-III antenna [WHK<sup>+</sup>78] for

helicon operation (both in hydrogen and deuterium) are utilized. The plasma volume is significantly reduced in comparison to the driver volume of the prototype source. This allows to reduce the totally required RF power to a maximum of 2 kW, while maintaining discharge parameters close to the ion source conditions. The investigated excitation frequencies range from the current baseline case of 1 MHz up to 4 MHz, for both inductive and wave heated discharges. In contrast to ion sources, no Faraday shield is applied, which significantly simplifies plasma ignition at lower RF power. In addition, the setup is equipped with versatile diagnostics providing access to the plasma parameters most crucial for an efficient driver plasma, foremost to the introduced figures of merit  $n_e$ ,  $n_H$  and  $\eta$ .

The features of this laboratory setup therefore allow for the dedicated and fundamental investigation of the described alternative plasma generation methods in comparison to the baseline case of ICPs driven at 1 MHz. The possibility of a direct and quantitative comparison of differently heated  $H_2/D_2$  discharges at ion source relevant parameters is considered as a unique capability of this setup with respect to other experiments aiming to explore alternative RF generation methods in view of ion sources for fusion.

Being part of a stepwise approach, the final goal of this experimental work is to provide the first and fundamental assessment whether any of the proposed alternative plasma generation techniques are promising enough to qualify for further investigations at larger scale, e.g. at an ion source test bed. In order to ensure the resilience of such an evaluation, the fundamental characteristics of the different heating mechanisms in low pressure hydrogen and deuterium plasmas have to be investigated. Therefore, the dependences of the introduced crucial discharge parameters on operational parameters like pressure, RF power and external magnetic field are studied, as well as the isotopic differences between hydrogen and deuterium regarding the plasma heating mechanisms.

## 3 Properties of low pressure low temperature hydrogen plasmas

A plasma is an at least partially ionized gas, thus consisting of both neutral and charged particles, which exhibits collective behaviour in response to electric and magnetic fields. In low pressure low temperature hydrogen plasmas  $\text{H}_2$  molecules, H atoms, three different species of positive ions ( $\text{H}^+$ ,  $\text{H}_2^+$ ,  $\text{H}_3^+$ ), negative hydrogen ions and electrons are present. Analogously, deuterium discharges comprise the corresponding species based on the heavier isotope D. The descriptions within this chapter will mainly refer to hydrogen for simplicity, implying that the mentioned concepts are equally valid for deuterium. In case there are significant isotopic differences present, they will be addressed specifically.

### 3.1 General plasma characteristics

In principle, laboratory low pressure low temperature plasmas are generated by applying an electric field to a neutral gas in the pressure range of a few Pa<sup>1</sup>. Primary electrons respond to the applied field, are accelerated to energies of the order of a few eV and subsequently ionize the gas particles. In equilibrium, a steady degree of ionization is achieved as the produced charged particles recombine again at the reactor walls, leading to a plasma which is, on a macroscopic scale, *quasi-neutral*, i.e. the sum of the positive charge density equals the sum of the negative charge density. With respect to the charged species present in a hydrogen plasma and their corresponding densities  $n$  this yields

$$n_{\text{H}^+} + n_{\text{H}_2^+} + n_{\text{H}_3^+} = n_e + n_{\text{H}^-}, \quad (3.1)$$

which reduces to  $n_{\text{ion}} = n_e$  if negative hydrogen ions can be neglected and the

---

<sup>1</sup>The following summary of the basic plasma characteristics required in the present work is mainly based on [LL05] and [CB11], where the underlying concepts are described in further details.

effective ion density  $n_{\text{ion}}$  is defined, comprising the three different positive ion species. In a plasma, electrostatic deviations from quasi-neutrality are effectively shielded by the free charge carriers as they respond to occurring E-fields. The characteristic screening length of Coulomb potentials in a plasma is designated as the *Debye length*  $\lambda_D$ . Only within the scale of  $\lambda_D$  can deviations from quasi-neutrality and electrostatic fields persist.

### Distribution functions and temperature

The characterization of the various particle ensembles within a plasma and the description of the occurring processes can be performed in general via distribution functions  $f(\mathbf{r}, \mathbf{v}, t)$ , which consider the probability that a certain particle occupies a given differential region of space at the position  $\mathbf{r}$  and has a velocity of  $\mathbf{v}$  at an instant of time  $t$ .

If an ensemble of the density  $n$  and the particle mass  $m$  is in thermal equilibrium, its isotropic velocity distribution function is given by the *Maxwell-Boltzmann distribution* (or short *Maxwellian distribution*)

$$f_M(v) = \left( \frac{m}{2\pi k_B T} \right)^{3/2} 4\pi v^2 \exp\left( -\frac{mv^2}{2k_B T} \right), \quad (3.2)$$

where  $k_B$  denotes the Boltzmann constant and a temperature  $T$  in the thermodynamic meaning can be assigned to the ensemble. Analogously, the Maxwellian distribution can be written in its energy dependent form

$$f_M(E) = \frac{2}{\sqrt{\pi}} \left( \frac{1}{k_B T} \right)^{3/2} \sqrt{E} \exp\left( -\frac{E}{k_B T} \right). \quad (3.3)$$

The mean velocity  $\langle v \rangle$  and mean energy  $\langle E \rangle$  of the ensemble are then respectively given by

$$\langle v \rangle = \sqrt{\frac{8k_B T}{\pi m}}, \quad (3.4)$$

$$\langle E \rangle = \frac{3}{2} k_B T. \quad (3.5)$$

In most laboratory low pressure low temperature plasmas, mainly the plasma electrons are heated by an external power supply and subsequently distribute their kinetic energy among themselves, the neutral gas particles and the ions via collisions. For the electron ensemble, a sufficient collision frequency for ther-

malization is assumed. In consequence, the *electron energy distribution function* EEDF can be characterized by a Maxwellian distribution and the corresponding electron temperature  $T_e$  in a first approximation. Regarding the energy transfer to the heavy neutral and ion particles however, high collision frequencies are required for a mutual thermalization with electrons due to the large difference in mass. Since this is typically not achieved in low pressure plasmas, the heavy particle temperatures  $T_{\text{gas}}$  of neutrals and  $T_{\text{ion}}$  of ions are much lower than the electron temperature, defining a low pressure low temperature plasma to be a non-equilibrium plasma. The typical electron temperatures at these parameters are of the order of eV whereas heavy particle temperatures are usually between one or two orders of magnitude lower and approximately equal, i.e.  $T_{\text{gas}} \approx T_{\text{ion}}$ . In the present case, also for the heavy particle ensembles a Maxwellian energy distribution is generally assumed with measured temperatures in the range between 0.03 and 0.07 eV ( $\approx 400 - 800$  K).

### Collision processes and rate coefficients

Within the plasma volume, a multitude of different processes occur, e.g. elastic and inelastic collisions leading to a transfer of momentum or the excitation, ionization and dissociation of particles. Quantitatively, these processes can be described by 0-dimensional reaction rates  $r$  accounting for the number of reactions per volume and time unit. The reaction rates of plasma processes can be interpreted as the source (+) and sink (−) terms of a certain state or particle density  $n_j$ , allowing to formulate balance rate equations of the form

$$\frac{dn_j}{dt} = \sum_{\text{sources}} r_+ - \sum_{\text{sinks}} r_-. \quad (3.6)$$

Regarding two-body collision processes involving the species  $j$  and  $k$ , the reaction rate can be calculated by the product of the reactant densities  $n_j$  and  $n_k$  and the characteristic *rate coefficient*  $X_{jk}$  of the specific reaction. The rate coefficient is depending on the corresponding *collision cross section*  $\sigma_{jk}(v_{\text{rel}})$  which is in turn depending on the relative velocity  $v_{\text{rel}}$  of the reactants. Assuming a Maxwell-Boltzmann velocity distribution for both species, the rate coefficient of a binary collision process can be approximated by

$$X_{jk} = \int_0^\infty \sigma(E_{\text{rel}}) \sqrt{\frac{2E_{\text{rel}}}{\mu_{jk}}} f_M(E_{\text{rel}}) dE_{\text{rel}}, \quad (3.7)$$

introducing the center of mass energy  $E_{\text{rel}} = \frac{\mu_{jk}}{2} v_{\text{rel}}^2$  and the reduced mass given by  $\mu_{jk} = \frac{m_j m_k}{m_j + m_k}$ . For the specific example of electron collisions with heavy particles, the reduced mass can be approximated by the much smaller electron mass  $m_e$  and the center of mass energy equals the kinetic energy  $E_e$  of the electrons. The rate coefficient is then provided by

$$X(T_e) = \int_0^\infty \sigma(E_e) \sqrt{\frac{2E_e}{m_e}} f_M(E_e, T_e) dE_e. \quad (3.8)$$

Based on the rate coefficients of a specific reaction, the average collision frequency  $\nu_{jk}$  of particles  $j$  with the corresponding collision partners  $k$  of a density  $n_k$  is provided:

$$\nu_{jk} = n_k X_{jk}. \quad (3.9)$$

Subsequently, the mean free path  $\lambda_j$  of particles  $j$  with a thermal velocity  $v_j$  between two collisions is given by

$$\lambda_j = \frac{v_j}{\nu_{jk}}. \quad (3.10)$$

### Particle diffusion and plasma boundaries

The flux  $\mathbf{\Gamma} = n\mathbf{v}$  of particles of the density  $n$  and velocity  $\mathbf{v}$  in a plasma can be caused by diffusion due to density gradients  $\nabla n$  in general and specifically for charged particles by the presence of electric fields  $\mathbf{E}$ . Accordingly, the flux can be written as

$$\mathbf{\Gamma} = \mu n \mathbf{E} - D \nabla n, \quad (3.11)$$

with the *diffusion coefficient*  $D = k_B T / m \nu_{\text{coll}}$  and the *mobility*  $\mu = q / m \nu_{\text{coll}}$  for particles of mass  $m$ , temperature  $T$  and charge  $q$  that experience collisions with the frequency  $\nu_{\text{coll}}$ .

In general, the diffusion of particles superimposes their random movement and can be a governing process that affects the population density of particles with sufficiently long lifetimes in the plasma volume. Due to the quasi-neutrality of a plasma, the diffusion of the heavy and slow ions and the light and fast electrons is coupled, which is known as *ambipolar diffusion*: in an anisotropic plasma, the faster diffusion of electrons eventually leads to the build-up of E-fields effectively pulling the plasma ions with them, or inversely retarding the electron movement. The effect of ambipolar diffusion on the particle balance in a low pressure low

temperature plasma is further assessed in section 3.4.

At the immediate plasma boundaries, e.g. an insulated object placed into the plasma, the differences of electron and ion diffusion have analogous consequences. The initially higher electron flux directly leads to a higher flux of negative charges on the object. Its charging results in a retarding potential for electrons that inversely attracts ions until an equilibrium is reached where the fluxes of electrons and ions are the same. The potential of the insulated object corresponding to this steady state is referred to as the *floating potential*  $\phi_{\text{fl}}$ , whereas the relatively higher potential of the bulk plasma is called the *plasma potential*  $\phi_{\text{pl}}$ .

### Plasma response to electromagnetic waves

The dynamic response of a plasma to an external oscillating electric field, e.g. an electromagnetic wave with the angular frequency  $\omega$ , is generally described by the dispersion relation of electromagnetic waves in a plasma. In analogy to dielectrics, a refractive index  $n_{\text{ref}}^2 = \epsilon_{\text{p}}$  can be defined with the complex permittivity of the plasma  $\epsilon_{\text{p}}$ . Considering the accordingly complex nature of the refractive index, i.e.  $n_{\text{ref}} = n_{\text{real}} + in_{\text{imag}}$  with the imaginary unit  $i$ , it can be written as

$$n_{\text{real}}^2 - n_{\text{imag}}^2 = 1 - \frac{\omega_{\text{p}}^2}{\omega^2(1 + (\nu_{\text{coll}}/\omega)^2)}, \quad (3.12)$$

with the collision frequency  $\nu_{\text{coll}}$  of the considered charged particles and the characteristic, so-called *plasma frequency*  $\omega_{\text{p}}$ . In general, the latter is defined by

$$\omega_{\text{p}} = (\omega_{\text{pe}}^2 + \omega_{\text{pi}}^2)^{1/2}, \quad (3.13)$$

being composed by the *electron plasma frequency*  $\omega_{\text{pe}}$  and the *ion plasma frequency*  $\omega_{\text{pi}}$ . Those are defined according to

$$\omega_{\text{pe}} = \sqrt{\frac{e^2 n_{\text{e}}}{\epsilon_0 m_{\text{e}}}} \quad \text{and} \quad \omega_{\text{pi}} = \sqrt{\frac{e^2 n_{\text{e}}}{\epsilon_0 m_{\text{ion}}}}, \quad (3.14)$$

with the vacuum permittivity  $\epsilon_0$  and the ion mass  $m_{\text{ion}}$ . Due to the mass difference, the electron plasma frequency is much larger than the ion plasma frequency (in hydrogen by a factor of 100), leading to the common approximation  $\omega_{\text{p}} = \omega_{\text{pe}}$ . With respect to the plasma frequency, two basic domains that describe the response of a plasma to an electromagnetic wave can be separated: at a frequency  $\omega > \omega_{\text{p}}$ , the plasma behaves as a dielectric ( $n_{\text{real}}^2 \approx 1 - \omega_{\text{pe}}^2/\omega^2$ ) and the wave propagates with very weak attenuation ( $n_{\text{imag}} \approx 0$ ). At lower frequencies of

$\omega < \omega_p$ , the waves are absorbed by the charged particles and decay, depending on the *collisionality ratio*  $\nu_{\text{coll}}/\omega$ . In consequence, the perturbations due to an incident wave are evanescent and diminish within a characteristic scale in the plasma, the so-called *skin depth*  $\delta$ . This is also the typical domain where radio-frequency discharges are operated, as for heating charged particles in the plasma those must be able to react to electromagnetic fields in general. The details of the power transfer between externally provided electromagnetic fields and the plasma are discussed in chapter 4.

## 3.2 Atomic and molecular properties of hydrogen isotopes

Many of the governing processes in low pressure low temperature plasmas lead to the (re-)distribution of internal energies of the neutral hydrogen particles H and H<sub>2</sub>. The basic concepts and designations regarding their internal energy and quantum mechanical state that are required and incorporated in the present work are summarized in the following paragraphs. Further and much more detailed information can be found in corresponding literature, e.g. [Her50, Ber05].

### Atomic hydrogen

If fine structure splitting of the electronic levels of the hydrogen atom is neglected, the energy of its states  $E_n$  with the principle quantum number  $n$  is given by

$$E_n = 13.60 \text{ eV} \times \left(1 - \frac{1}{n^2}\right). \quad (3.15)$$

Due to disregarding fine structure splitting, the states are degenerate by a degree of  $2n^2$ . The ionization limit of 13.60 eV is reached for  $n \rightarrow \infty$ . The atomic ground state has an electron affinity of  $E_a$  of 0.75 eV, which allows the formation of the stable H<sup>-</sup> ion. In the right part of figure 3.1, the energy levels of atomic hydrogen are depicted. Optical transitions are allowed between all states  $E_n$ . Exemplarily included in figure 3.1 are the two most intense and well known transition series of H, namely the Lyman series which terminates on the ground state  $n = 1$ , and the Balmer series with the lower quantum number  $n = 2$ . The emission lines of the Lyman series are located in vacuum ultraviolet spectral range, while the Balmer series emits in the visible range, thus providing diagnostic access via optical emission spectroscopy.

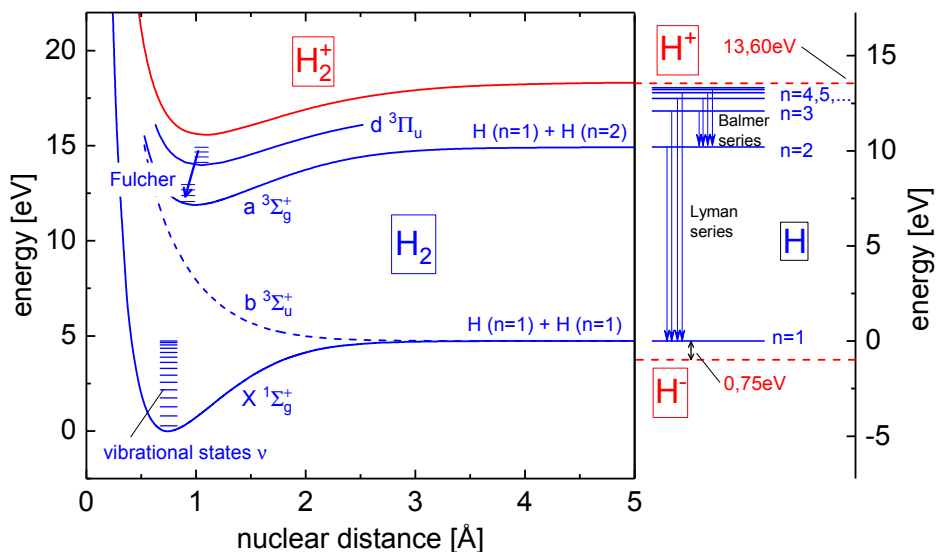


**Figure 3.1:** Potential energy curves of selected electronic states of the hydrogen molecule and the  $H_2^+$  ion [Sha70, Sha71], including exemplary vibrational levels [FW06]. On the right side, energy levels of the hydrogen atom are shown [KRR18]. In order to illustrate the correlation of the dissociation products, its energy axis is shifted with respect to the left part.

## Molecular hydrogen

For the homonuclear hydrogen molecule  $H_2$ , internal energy can also be stored via the relative motion of the two nuclei, thus resulting in a far more complex structure of the internal energy levels compared to the atom. Applying the Born-Oppenheimer approximation implying that the motion of the nuclei is decoupled from the electron motion, the internal energy  $E$  of the molecules can be described by the sum of its separate contributions, namely the electronic energy  $E_{\text{el}}$ , the vibrational energy  $E_{\text{vib}}(\nu)$  and the rotational energy  $E_{\text{rot}}(J)$ .  $\nu$  and  $J$  denote the vibrational and rotational quantum numbers, respectively.

The discrete electronic states of the molecule are determined by the coupling of the orbital angular momentum and the spin of the two electrons. Depending on the resulting total spin, for hydrogen a singlet system (antiparallel spins) and a triplet system (parallel spins) exist. Due to quantum mechanical selection rules, optical transitions are only allowed within both systems, and not between each other. The states of the singlet system are typically denoted by capital letters, the ones of the triplet system by lower case. The electronic ground state is conventionally designated  $X^1\Sigma_g^+$ . A description of the systematic spectroscopic notation applied within this work can be found in [Her50].

In the left part of figure 3.1, selected states of  $\text{H}_2$  and the corresponding potential energy curves depending on the nuclear distance are depicted [Sha70, Sha71]. The potential curve of a stable, binding state like the ground state  $\text{X}^1\Sigma_g^+$  possesses at least one distinct minimum, while repulsive states like the  $\text{b}^3\Sigma_u^+$  state are characterized by a monotonic decrease with increasing nuclear distance.

For the binding states, a discrete set of vibrational states designated by the vibrational quantum number  $\nu \in \mathbb{N}_0$  exists. For hydrogen, the energetic difference between these is of the order of 0.5 eV, decreasing with increasing  $\nu$ . Exemplary vibrational levels are included in figure 3.1 [FW06]. In turn, each vibrational state comprises of discrete rotational levels characterized by the rotational quantum number  $J \in \mathbb{N}_0$ . The respective energy difference between rotational levels in  $\text{H}_2$  is of the order of 0.01 eV.

The excitation into a repulsive state via electron impact or a sufficiently high vibrational excitation leads to a dissociation of the molecule. In order to indicate the corresponding reactants and products of dissociation, the energy scales of the molecular states and the atomic states in figure 3.1 are shifted with respect to each other. Furthermore, the potential curve of the ground state of the  $\text{H}_2^+$  molecule (ionization energy 15.4 eV), as well as the upper and lower state of the Fulcher- $\alpha$  transition ( $\text{d}^3\Pi_u, \nu', J' \rightarrow \text{a}^3\Sigma_g^+, \nu'', J''$ ) are depicted in the graph. The latter is the most intensely emitting transition of  $\text{H}_2$  in the visible spectrum, located between 590 nm and 650 nm and provides diagnostic accessibility to the distribution of rotational and vibrational states within the  $\text{H}_2$  molecule via optical emission spectroscopy.

### Isotopic variations between hydrogen and deuterium

In a first approximation neglecting the influence of the nuclear spin, the electronic structure is independent of the nuclear mass, which refers to both atoms and molecules. Significant isotopic deviations are therefore negligible for the atoms and restricted to the vibrational and rotational levels of the molecules. The higher mass of deuterium generally leads to a smaller difference between the vibrational and rotational energy levels compared to hydrogen [Die58, FSC85, FW06]. This implies furthermore that the wavelengths of corresponding ro-vibronic emission lines are located closer to each other and the total number of possible states within the potential of a distinct binding state is larger. Regarding the processes in  $\text{H}_2/\text{D}_2$  discharges, isotopic differences are thus expected if a pronounced dependence on the ro-vibronic state of the involved reactants is given.

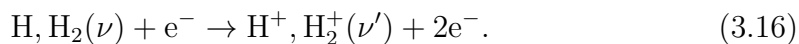
### 3.3 Plasma processes

In hydrogen, a multitude of different processes can take place due to the variety of different neutral and ion species. Collision processes can occur in the plasma volume as well as at surfaces in direct contact to the plasma. An extensive review of the collision processes in low temperature hydrogen plasmas is given in [JRS03]. In the present work, the main focus lies on the plasma heating region where the externally provided energy is transferred to the electrons, which distribute it further via subsequent ionization, dissociation and excitation processes. In correspondence, this region is conventionally also denoted as an *ionizing plasma*, in contrast to a *recombining plasma*, typical e.g. for the downstream or expansion region of a discharge.

A selection of the most relevant processes of the discharges at hand including corresponding cross sections and rate coefficients is provided in the following. In order to identify the governing processes, experimentally measured parameters are required. The investigated hydrogen and deuterium plasmas in a pressure range from 0.3 to 10 Pa are characterized by electron densities roughly between  $10^{16} \text{ m}^{-3}$  and  $10^{18} \text{ m}^{-3}$ , electron temperatures of 2 – 6 eV and heavy particle temperatures of 400 – 800 K.

#### Ionization and ion recombination

The formation of the positive ion species  $\text{H}^+$  and  $\text{H}_2^+$  is dominated by electron impact ionization of hydrogen atoms and molecules



In figure 3.2, the corresponding cross sections are shown in the energy region near the ionization threshold, which is the region of interest in low temperature hydrogen discharges. Due to its lower threshold energy, the ionization cross section of atomic hydrogen/deuterium [SEG87] exceeds those of the molecules  $\text{H}_2$  and  $\text{D}_2$  [YSH<sup>+</sup>08, YKK<sup>+</sup>10] at energies lower than 20 eV, whereas the molecules are easier to ionize at higher energies. Since the electronic structure of deuterium and hydrogen is virtually equivalent, the isotopic differences are only marginal for the molecules (with  $\text{D}_2$  slightly exceeding  $\text{H}_2$ , due to the small influence of the differences regarding ro-vibronic states). Regarding the atoms, the cross sections are typically assumed to be identical.

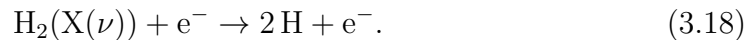
Subsequent to the formation of ions via equation (3.16), the triatomic molecule  $\text{H}_3^+$  is produced by the collision of the heavy particles  $\text{H}_2$  and  $\text{H}_2^+$ :



The reverse process of ionization - the recombination of positive ions and electrons to neutrals - is typically negligible in the plasma volume. Hence, the main loss mechanism of ions and electrons is the diffusion to the walls of the discharge chamber followed by a recombination at the wall [Beh91]. The balancing of both processes yields the ionization balance, which is specifically addressed in section 3.4. Furthermore, the volume production of negative ions is neglected in the present case, as the destruction rate of  $\text{H}^-$  due to collisions with fast electrons and atomic hydrogen is very high in an ionizing plasma [Bac06], leading to a negligibly low steady state  $\text{H}^-$  density.

### Molecular dissociation and recombination

Atomic hydrogen is dominantly produced in the plasma via electron impact dissociation of molecular hydrogen in the electronic ground state:



As described in section 3.2, the dissociation proceeds mainly via the intermediate excitation of repulsive states (predominantly  $\text{H}_2(\text{b}^3\Sigma_u^+)$ ) and is strongly dependent on the vibrational state  $\nu$  of the hydrogen molecule, as the probability of this process increases for higher  $\nu$ . This is illustrated in figure 3.3, where the rate coefficients  $X_{\text{diss},\nu}(T_e)$  of the electron impact dissociation of  $\text{H}_2$  and  $\text{D}_2$  are depicted for the first three vibrational states of hydrogen and the first four of deuterium, respectively. Based on cross section data provided by [TT02a, TT02b] and assuming a Maxwellian EEDF, the rate coefficients are calculated according to equation (3.8). There is a significant isotopic difference, as the rate coefficients are systematically higher in deuterium than in hydrogen within the whole electron temperature region of relevance. This leads to the typical observation that the degree of dissociation in low pressure low temperature discharges is significantly higher in deuterium compared to hydrogen.

The reverse process of dissociation is the recombination of atoms to hydrogen molecules. It is negligible in the plasma volume and takes place in the form of surface catalytic reactions solely at the walls of the discharge chamber [HK81,

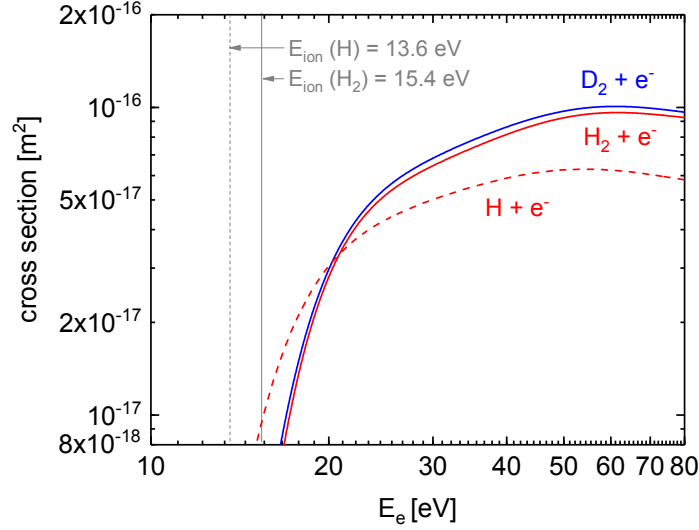


**Figure 3.2:** Cross sections of electron impact ionization of the hydrogen and the deuterium molecule [YSH<sup>+</sup>08, YKK<sup>+</sup>10] and of atomic hydrogen [SEG87]. Additionally, the process thresholds given by the corresponding ionization energies of the particles are indicated.

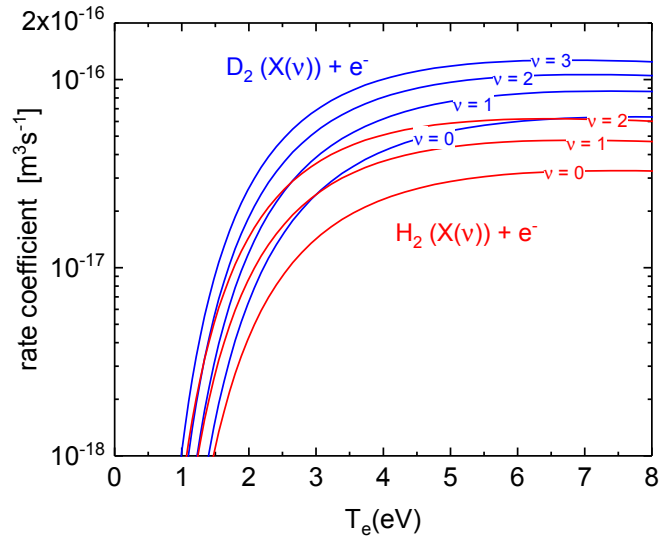
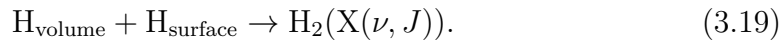
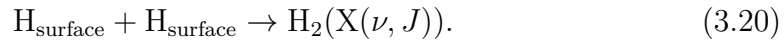


**Figure 3.3:** Rate coefficients of electron impact dissociation of  $H_2$  and  $D_2$ , depending on the vibrational state of the electronic ground state and calculated based on cross section data by [TT02a, TT02b] assuming a Maxwellian EEDF. Included are the coefficients until  $\nu = 2$  for  $H_2$  and until  $\nu = 3$  for  $D_2$ .

Chr88]. The recombination processes require the preceding adsorption of hydrogen atoms at the surface, commonly also referred to as *sticking*. Due to their reactivity, the hydrogen radicals are able to form strong bonds with the surface at hand, typically denoted as chemical adsorption or chemisorption, in short. This leads to a certain coverage of the surfaces with adsorbed hydrogen, depending on the properties of both the surface and the plasma. The actual recombination process itself can then proceed via two main reactions pathways. First, the so-called *Eley-Rideal mechanism* describes the reformation of a molecule via the collision of an impinging atom from the plasma volume with an adsorbed atom on the surface  $H_{\text{surface}}$ :



Second, the *Langmuir-Hinshelwood mechanism* denotes the recombination of two adsorbed atoms:



Both processes lead to the formation of ro-vibrationally excited hydrogen molecules in the ground state. In order to quantitatively assess the process of atomic recombination on the surface, the *recombination coefficient*  $\gamma$  is introduced, equal to the ratio of atoms impinging on the surface that recombine to the total number impinging on the surface [SL49]. However, the reliable experimental determination of  $\gamma$  is challenging, as it is highly depending on the surface material, its roughness and temperature as well as on the actual atomic coverage of the surface at hand. The coverage itself is in turn influenced by the material and temperature of the surface as well, and in general also dependent on the total influx of atomic hydrogen from the volume, thus on the volume density and temperature of atomic hydrogen. Furthermore, the presence of impurities and the physical sputtering due to ion bombardment from the bulk plasma can play a role as well. The consideration of absolute values of  $\gamma$  from literature in order to

**Table 3.1:** Values of the recombination coefficient  $\gamma$  of hydrogen on different surfaces as reported by the indicated sources.

Material	$\gamma$ ( $T \approx 500$ K)	Sources
quartz	$10^{-4} - 10^{-2}$	[GJL <sup>+</sup> 59], [KB91], [MM71], [WW62]
Al <sub>2</sub> O <sub>3</sub>	$10^{-4} - 10^{-3}$	[GJL <sup>+</sup> 59]
stainless steel	$\approx 0.1$	[MDZ99], [MM71]
other metals	$0.05 - 0.5$	[MM71], [WW61]

quantify the rate of surface recombination in a specific discharge therefore requires a critical assessment. This is illustrated by the fact that the reported values of  $\gamma$  for the same material sometimes deviate by orders of magnitude. In table 3.1, typical values of  $\gamma$  reported for the materials relevant in the present work in the temperature region of 500 K are presented. The values of the dielectric materials quartz and  $\text{Al}_2\text{O}_3$ , both a frequent choice for insulating vessels and windows for RF discharges, are typically about two orders of magnitude lower than all metallic surfaces. Consequently, the recombination rate in experiments predominantly applying dielectric surfaces is typically lower than in metallic vessels and thus, higher atomic densities are observed in equilibrium. If a combination of dielectric and metallic surfaces is present (as it is the case in most RF experiments), the global probability for a recombination is depending on the properties and the area of each surface in contact with the plasma. In practice, already a small metallic surface in an otherwise dielectric vessel can effectively dominate the recombination rate, since the recombination probability on metals is orders of magnitude higher compared to dielectrics.

For the recombination of hydrogen atoms on quartz surfaces, an empirical expression for the temperature dependence of  $\gamma$  is provided by [Bel72], based on measurement data by [WW62]:

$$\gamma(T) = 0.151 \exp\left(\frac{-1.09 \times 10^3}{T}\right). \quad (3.21)$$

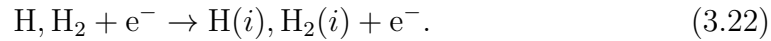
Even though the provided absolute value is, as already discussed, not necessarily transferable without limitations, it describes well the typical behaviour observed for  $\gamma(T)$ , which increases with increasing  $T$  in the present temperature region above room temperature.

Regarding an occurrence of isotopic effects within the recombination process, unfortunately no resilient investigations comparing hydrogen isotopes are found in literature. However, since both the chemical adsorption at the surface as well as the recombination process itself (i.e. the molecular binding energy) are mainly depending on the electronic properties of the particles, virtually no difference between deuterium and hydrogen is expected in this case.

### Excitation and spontaneous emission

The dominating population channel of electronically excited states of atoms  $\text{H}(i, k)$  and molecules  $\text{H}_2(i, k)$  in an ionizing plasma is given by electron impact

excitation of the corresponding particles in the ground state:



In case there are optically allowed transitions, the excited states  $i$  are mainly depopulated by spontaneous emission into a lower electronic state  $k$  by emission of a photon of the energy  $E_i - E_k$ . The rate of an optical transition  $i \rightarrow k$  is called emissivity  $\epsilon_{ik}$  and is defined by the product of the density of the upper state  $n_i$  and the transition probability given by the *Einstein coefficient for spontaneous emission*  $A_{ik}$ :

$$\epsilon_{ik} = n_i A_{ik}. \quad (3.23)$$

Consequently, information regarding the excited states of hydrogen atoms and molecules can be gained from their characteristic emission, which provides the basis for optical emission spectroscopy.

Regarding the hydrogen atom however, additional excitation channels apart from electron impact excitation from the atomic ground state can be present. First, the population of excited states can also occur via recombination processes of ions, which are generally negligible in the present case of an ionizing plasma, though. Second, also so-called *dissociative excitation* of  $\text{H}_2$  can contribute. The latter describes that not all the molecules taking part in the dissociation process of equation (3.18) are dissociating via the dominating channel involving the repulsive  $\text{b}^3\Sigma_{\text{u}}^+$  state, but via electronically higher excited repulsive states that dissociate into excited hydrogen atoms in turn. Therefore, a part of the excited population of atomic hydrogen, and subsequently of the emitted atomic radiation, can be coupled to the ground state of the molecules.

### Elastic collisions and electron-neutral collision frequency

In contrast to the inelastic collisions of electrons with neutrals leading to their respective excitation, ionization or dissociation, elastic collisions do not have a threshold energy. Therefore, elastic scattering of electrons is typically the most frequent collision process in weakly ionized low pressure discharges and predominately defines the mean free path of electrons, especially at lower energy. In figure 3.4 the rate coefficients for elastic scattering of electrons with the neutral species H and  $\text{H}_2$  are depicted, which are calculated according to equation (3.8) based on the respective momentum change cross sections provided

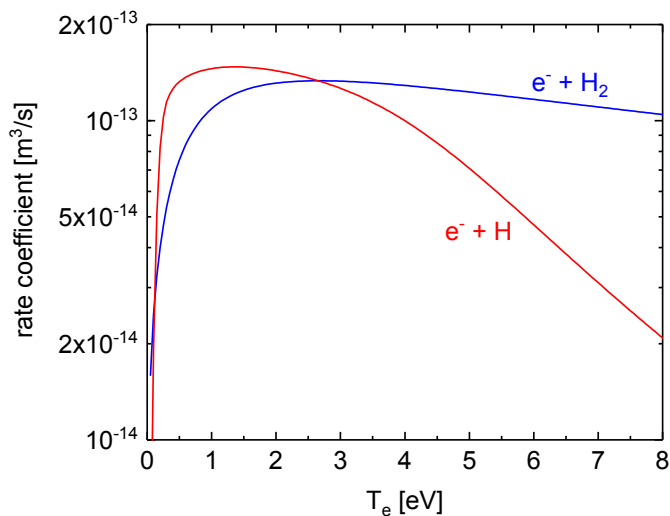


**Figure 3.4:** Rate coefficients  $X(T_e)$  for elastic collisions of electrons with neutrals  $H$  and  $H_2$ , determined based on momentum change cross sections provided by [Iti74, YSH<sup>+</sup>08] and assuming a Maxwellian EEDF.

by [Iti74, YSH<sup>+</sup>08] and assuming a Maxwellian EEDF. As illustrated, both rate coefficients cross at 2.6 eV and are fairly comparable in the region between 1 and 4 eV. At lower energies, the rate coefficient of the collision with  $H$  is higher than with  $H_2$ , at higher energies the situation is inverse. For deuterium, the momentum transfer cross sections are virtually the same as for hydrogen [YKK<sup>+</sup>10], thus no isotopic difference is present in this case. Based on these rate coefficients, the characteristic collision frequencies of electrons with atoms  $\nu_{eH}$  and molecules  $\nu_{eH_2}$  can be determined according to equation (3.9), which are central quantities of the RF heating mechanism described in section 4.

### 3.4 Particle diffusion and balances

As already mentioned in the previous chapter, for both positive ions and hydrogen atoms, diffusion to the vessel walls and subsequent recombination are the dominant loss mechanisms. Setting up balance rate equations for these species allows to assess and interpret experimentally observed dependencies of crucial plasma parameters. To do so, an assessment of the diffusion rates of these particles at the present conditions is necessary. The following descriptions are based on a review by [Möl93]<sup>2</sup>.

<sup>2</sup>A general description of the diffusion of neutral and charged particles within a low temperature plasma can be found in various publications and textbooks, e.g. [LL05, MM88, Fru09].

In general, the diffusion rate  $r_{\text{diff},j}$  of a particle species  $j$  of the density  $n_j$  to the wall can be written as

$$r_{\text{diff},j} = \frac{n_j}{\tau_j}, \quad (3.24)$$

where  $\tau_s$  denotes the mean *confinement time* of particles within the plasma. Depending on their mean free path  $\lambda_j$  between two collisions (predominantly with the background gas) and the typical vessel dimensions, different regimes of diffusion are given.

At sufficiently low pressure,  $\lambda_j$  is much larger than the dimensions of the vessel and thus, most particles directly collide with the wall subsequent to their creation via ionization or dissociation. This regime is referred to as the *molecular* or the *free fall regime*. At higher pressures, the probability for collisions is much larger. In consequence, the mean free path of the regarded species becomes significantly smaller than the vessel dimensions and the regime of *laminar diffusion* is reached.

### Diffusion of atoms and dissociation balance

For the investigated discharges, the most frequent collision processes of atomic hydrogen in the bulk plasma are elastic collisions with hydrogen molecules and other atoms. Taking into account cross sections of these collisions provided by [Phe90, KS98], the mean free path of atoms at the present parameters can be estimated according to equation (3.10). Such an evaluation yields that  $\lambda_{\text{H}}$  is of the order of cm and thus, comparable to the vessel dimensions (see chapter 5.1). Therefore, the relevant diffusive regime is an intermediate one, where both molecular and laminar diffusion have to be considered equally.

In the free fall regime, the mean confinement time  $\tau_{\text{mol,H}}$  of atoms is given by

$$\tau_{\text{mol,H}} = \frac{\Lambda_{\text{mol}}}{\langle v_{\text{H}} \rangle}, \quad (3.25)$$

with the mean velocity of atoms  $\langle v_{\text{H}} \rangle$  and the *mean diffusion length*  $\Lambda_{\text{mol}}$ . The latter depends on the volume  $V$  and surface area  $A$  of the plasma vessel at hand and is given by<sup>3</sup>

$$\Lambda_{\text{mol}} = \frac{2V(2 - \gamma)}{A\gamma}. \quad (3.26)$$

In this case,  $\gamma$  is the recombination coefficient introduced in the previous chapter,

---

<sup>3</sup>This expression is provided by [Cha87], the respective one in [Möl93] is incorrect.

which quantifies the probability that an atom hitting the wall is lost due to its recombination to a hydrogen molecule. In this 0-dimensional assessment, the recombination coefficient is treated as a global, isotropic parameter. This is an approximation, since  $\gamma$  can actually be influenced by a variety of factors in a real plasma such as wall material and temperature, as described in section 3.3.

In the laminar regime, the mean confinement time of atoms  $\tau_{\text{lam,H}}$  can be estimated according to

$$\tau_{\text{lam,H}} = \frac{\Lambda_{\text{lam}}^2}{D_{\text{H}}} \quad \text{with} \quad D_{\text{H}} = \frac{3\sqrt{\pi}}{8} \lambda_{\text{H}} \sqrt{k_{\text{B}} T_{\text{gas}} \frac{m_{\text{H}} + m_{\text{H}_2}}{2m_{\text{H}}m_{\text{H}_2}}}. \quad (3.27)$$

In the equation above,  $D_{\text{H}}$  denotes the *normal* diffusion coefficient of hydrogen atoms. The laminar mean diffusion length  $\Lambda_{\text{lam}}$  is given by

$$\Lambda_{\text{lam}}^2 = \left( \frac{8}{\rho^2} + \frac{3}{L_c^2} \right)^{-1} + \frac{2V(2-\gamma)}{3A\gamma} \lambda_{\text{H}}, \quad (3.28)$$

with the radius  $\rho$  and the length  $L_c$  of a cylindrical plasma vessel. In the present case, where an intermediate diffusion regime has to be treated, the total confinement time of hydrogen atoms  $\tau_{\text{H}}$  can be approximated by the sum  $\tau_{\text{mol,H}} + \tau_{\text{lam,H}}$ .

In order to investigate the equilibrium density ( $\frac{dn_{\text{H}}}{dt} = 0$ ) of atoms, the production and destruction processes of H have to be balanced. A simplified dissociation rate balance can be set up by equating the production rate  $r_{\text{diss}}$  of atoms via electron impact dissociation with the loss rate  $r_{\text{diff,H}}$  of atoms at the walls, accounting for the confinement times of atoms deduced above. In a first approximation, the dependence of the dissociation process on the vibrational states  $\nu$  of  $\text{H}_2$  can be eliminated by introducing an effective rate coefficient  $X_{\text{diss}}$ . This yields

$$\frac{1}{2} n_{\text{H}_2} n_{\text{e}} X_{\text{diss}}(T_{\text{e}}) = \frac{n_{\text{H}}}{\tau_{\text{mol,H}} + \tau_{\text{lam,H}}}. \quad (3.29)$$

The factor  $\frac{1}{2}$  on the left accounts for the fact that two atoms are created for each dissociation process of  $\text{H}_2$ . Cross sections for the calculation of  $X_{\text{diss}}(T_{\text{e}})$  are provided by [JLE<sup>+</sup>87]. In practice, the evaluation of this rate equation allows to check whether the experimentally obtained values of  $n_{\text{H}}/n_{\text{H}_2}$  can be correlated to simultaneously measured variations of the plasma parameters, e.g.  $n_{\text{e}}$  and  $T_{\text{e}}$ . Thereby, an implicit access regarding the (directly inaccessible) recombination processes of H at the walls is provided.

### Ion diffusion and ionization balance

As qualitatively introduced in section 3.1, the diffusion of ions in a quasineutral plasma is coupled to the electrons. Due to their higher mass and lower temperature, the diffusion of ions is slower, limits the diffusion of electrons and therefore effectively dominates the loss rate of charged particles to the chamber walls.

In order to assess the diffusion regime for ions within the discharges investigated in this work, the mean free path of the different hydrogen ion species are estimated in analogy to the atoms. The collisional cross sections required for this assessment are provided by [Phe90, KS98]. In the pressure region of relevance between 0.3 Pa and 10 Pa, this estimation yields that  $\lambda_{\text{ion}}$  is globally smaller than the radius  $\rho = 4.5$  cm of the cylindrical discharge vessel in use (see chapter 5.1). At pressures above 1 Pa, the mean free path is well below the vessel radius and the assumption of a laminar ion transport is a valid approach. Below 1 Pa however, the mean free path of ions approaches the order of the vessel radius of a few cm. Consequently, the low pressure discharges in this work are located in an intermediate regime of ion diffusion, where neither molecular nor laminar diffusion are strictly valid. In contrast to the treatment of atoms, the ion transport in the free fall regime is neglected in the present case, though. This approach is followed since the free fall ion transport can no longer be properly assessed in a 0-dimensional approach once the effects of static magnetic fields need to be included (see chapter 3.5). Therefore, only the laminar ion transport is considered, which leads to the frequently discussed description of ambipolar diffusion. The confinement time of ions  $\tau_{\text{ion}}$  is then given by

$$\tau_{\text{ion}} = \frac{\Lambda_{\text{ion}}^2}{D_{\text{a}}} \quad \text{with} \quad D_{\text{a}} = \frac{3\sqrt{\pi}}{8} \frac{T_{\text{e}}}{T_{\text{gas}}} \lambda_{\text{ion}} \sqrt{\frac{k_{\text{B}} T_{\text{gas}}}{m_{\text{ion}}}}, \quad (3.30)$$

where  $D_{\text{a}}$  denotes the ambipolar diffusion coefficient. Due to the presence of different positive ion species in hydrogen/deuterium plasmas,  $m_{\text{ion}}$  is in the present case considered as an effective ion mass. The mean diffusion length  $\Lambda_{\text{ion}}$  depends on the geometry of the discharge vessel and on the spatial density profiles within the discharge. In cylindrical plasmas, the ambipolar diffusion of electrons and ions is radially symmetric and leads to characteristic density profiles with a maximum at the central axis and a decrease towards the radial walls that are described by zero-order Bessel functions [TL29, Beh91]. For a finite cylindrical vessel with radius  $\rho$  and length  $L_{\text{c}}$ ,  $\Lambda_{\text{ion}}$  can be approximated by

$$\frac{1}{\Lambda_{\text{ion}}^2} = \left( \frac{2.405}{\rho} \right)^2 + \left( \frac{\pi}{L_c} \right)^2. \quad (3.31)$$

Since the free fall ion transport is generally neglected, the application of ambipolar diffusion according to equation (3.30) has to be considered as an approximation at pressures below 1 Pa. It is well capable of reflecting the qualitative dependencies of the ion diffusion on the plasma parameters, but insufficient for a quantitative description. Since the collisionless loss mechanisms of ions is not included, the confinement time in this intermediate regime is generally underestimated [Möl93].

Equating the derived expression for the ion loss via ambipolar diffusion to the walls with the ion production via electron impact ionization yields to the so-called *ionization balance*. A simplified consideration accounting for the total positive ion density  $n_{\text{ion}}$  and only one neutral species of a neutral particle density  $n_0$  leads to

$$n_e n_0 X_{\text{ion}}(T_e) = \frac{n_{\text{ion}}}{\tau_{\text{ion}}}, \quad (3.32)$$

where the rate coefficient  $X_{\text{ion}}(T_e)$  is given by equation (3.8). Applying quasineutrality and neglecting the inverse linear dependence of  $\tau_{\text{ion}}$  on  $T_e$  compared to the high temperature sensitivity of the rate coefficient  $X_{\text{ion}}(T_e)$ , the following proportionality is derived:

$$X_{\text{ion}}(T_e) = \frac{1}{n_0 \tau_{\text{ion}}} \propto \frac{\lambda_{\text{ion}}}{n_0 \sqrt{m_{\text{ion}}}}. \quad (3.33)$$

This provides the qualitative description of the typical pressure dependent behaviour of  $T_e$  observed in low pressure low temperature discharges: with decreasing pressure, the neutral density decreases and the mean free path increases, leading to an increase of the electron temperature. This arises from the higher losses of ions due to their faster diffusion which has to be compensated by an increasing ionization rate.

### Power balance

The power  $P_{\text{plasma}}$  that is absorbed by the discharge itself mainly heats the electrons in the plasma. The specific heating and power transfer mechanisms of the discharges investigated in this work will be discussed explicitly in section 4. When the discharge reaches steady state, the power  $P_{\text{plasma}}$  is balanced by different loss channels. The equation of those losses with the absorbed power is commonly

referred to as the (electron) *power balance* of the plasma. Via this power balance, characteristic dependencies of the electron density can be qualitatively described. The power losses within the plasma volume mostly occur due inelastic collisions of electrons with neutrals leading to their subsequent excitation, dissociation or ionization [Beh91], i.e.

$$P_{\text{plasma}} = P_{\text{excitation}} + P_{\text{dissociation}} + P_{\text{ionization}}. \quad (3.34)$$

The amount of the provided energy which is transferred to neutral particles by elastic collisions or lost to the wall by convection is typically small compared to these dominant loss mechanisms [Beh91]. In general, the quantitative formulation of a detailed power balance requires to consider a variety of different atomic and molecular states, corresponding energy levels and the calculation of rate coefficients for each process specifically. For qualitative purposes however, this situation can be strongly simplified. Assuming only one species in the ground state, only one positive ion species and only one possible dissociation process, the individual power losses can be written as [Beh91]

$$P_{\text{excitation}} = V_{\text{plasma}} n_e n_0 \sum_j X_{\text{exc},j}(T_e) E_j, \quad (3.35)$$

$$P_{\text{dissociation}} = V_{\text{plasma}} n_e n_0 X_{\text{diss}}(T_e) E_{\text{diss}}, \quad (3.36)$$

$$P_{\text{ionization}} = V_{\text{plasma}} n_e n_0 X_{\text{ion}}(T_e) E_{\text{ion}}. \quad (3.37)$$

$V_{\text{plasma}}$  is the plasma volume.  $E_j$ ,  $E_{\text{diss}}$  and  $E_{\text{ion}}$  are the threshold energies of excitation (to a state  $j$ ), dissociation and ionization with  $X_{\text{exc},j}$ ,  $X_{\text{diss}}$  and  $X_{\text{ion}}$  denoting the corresponding rate coefficients. Applying these expressions to equation (3.34) in combination with the ionization balance provided in equation (3.32) yields

$$P_{\text{plasma}} = \frac{V_{\text{plasma}} n_e}{\tau_{\text{ion}}} \left( \frac{\sum_j X_{\text{exc},j}(T_e) E_j}{X_{\text{ion}}(T_e)} + \frac{X_{\text{diss}}(T_e) E_{\text{diss}}}{X_{\text{ion}}(T_e)} + E_{\text{ion}} \right). \quad (3.38)$$

Due to the pronounced dependencies of the rate coefficients on  $T_e$ , the actual distribution of the absorbed power to the different loss channels depends significantly on  $T_e$  and thus, on the operating parameters of the discharge in general. If the electron temperature is assumed to be constant however, the expression in brackets is constant as well. In this case, the proportionality

$$V_{\text{plasma}} n_e \propto P_{\text{plasma}} \tau_{\text{ion}} \quad (3.39)$$

is obtained. According to this simple approximation, the electron density in a constant plasma volume is therefore expected to rise if the absorbed power  $P_{\text{plasma}}$  or the confinement time  $\tau_{\text{ion}}$  is increased.

### 3.5 Particle motion in a static magnetic field

In the present work, the discharges are exposed to an externally generated, static magnetic field  $\mathbf{B}_0$  of a magnitude  $B_0$  in the mT range. This affects both the particle motion as well as the propagation of electromagnetic waves in the plasma. The latter will be specifically assessed later within chapter 4.3. Due to the magnetic field, a spatial anisotropy depending on the direction of  $\mathbf{B}_0$  is present. To account for this, vector quantities are expressed by a linear combination of their components parallel (subscript  $\parallel$ ) and perpendicular (subscript  $\perp$ ) to the direction of  $\mathbf{B}_0$ . The direction of the magnetic field is defined to be parallel to the  $\hat{z}$ -axis of a cylindrical plasma vessel, i.e.  $\mathbf{B}_0 = B_0 \hat{z}$ .

The presence of static magnetic fields significantly alters the motion of charged particles in a plasma and thus, the plasma transport in general<sup>4</sup>. Being affected by the Lorentz force (and the centrifugal force due to inertia), moving charged particles describe a circular orbit perpendicular to  $\mathbf{B}_0$  around a guiding center travelling along the direction of  $\mathbf{B}_0$ . This movement is commonly referred to as *gyration* and characterized by the *gyration* or *cyclotron frequency*  $\omega_c$

$$\omega_c = \frac{|q|B_0}{m}. \quad (3.40)$$

The *gyration radius*  $r_c$  of this orbital motion around the magnetic field lines is given by

$$r_c = \frac{v_{\perp}}{\omega_c}, \quad (3.41)$$

with  $v_{\perp}$  denoting the particle's speed perpendicular to  $\mathbf{B}_0$ . The dependence of the gyration frequency on the particle mass  $m$  and charge  $q$  leads to different gyration frequencies and radii for electrons and ions at the same magnetic field.

---

<sup>4</sup>The description in this paragraph is mainly based on [LL05] and [CB11], where the underlying concepts are described in further detail.

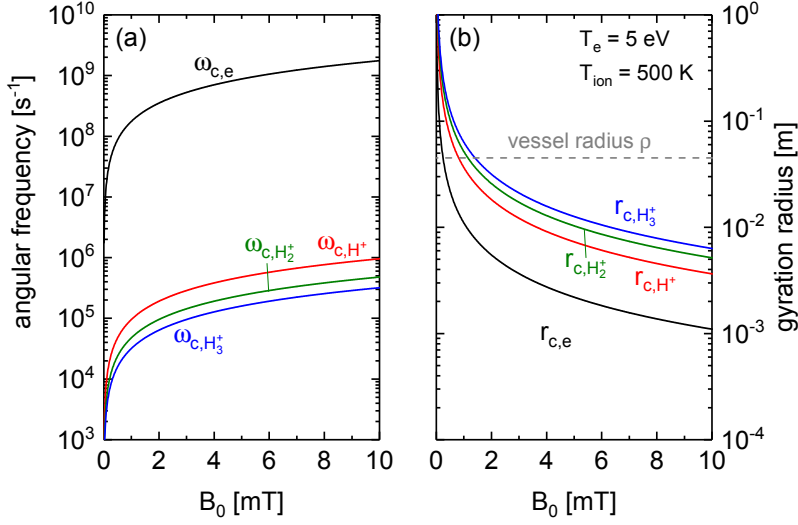


**Figure 3.5:** Gyration frequencies (a) and radii (b) of electrons and positive hydrogen ions  $H^+$ ,  $H_2^+$ ,  $H_3^+$  at varying magnetic field. In (b), the radius of the cylindrical discharge vessel applied in this work is indicated for a comparison.

Figure 3.5 (a) shows the gyration frequencies of electrons and hydrogen ions at magnetic fields between 0 and 10 mT. The gyration frequency of electrons  $\omega_{c,e}$  is of the order of 1 GHz while the frequency  $\omega_{c,ion}$  of the ions is in the range of several hundred kHz, decreasing with increasing ion mass. Assuming thermal velocity distributions for both electrons ( $T_e \approx 5$  eV) and ions ( $T_{ion} \approx T_{gas} \approx 500$  K), the respective gyration radii are depicted in figure 3.5 (b). The values  $r_{c,e}$  for the electrons are in the mm range whereas those of the ions range from mm up to a few cm. If the dimensions of the plasma chamber perpendicular to the magnetic field are large compared to the gyration radii, the charged particles are confined to the magnetic field lines, which is frequently referred to as being *magnetized*. For the present setup and parameters, this applies well for the electrons even for low magnetic fields, while the hydrogen ions are only partly magnetized at low fields since their gyration radii are of the same order as the vessel radius, as illustrated in figure 3.5 (b). For deuterium, the ion mass is a factor of two higher, leading to lower gyration frequencies and higher gyration radii, respectively.

### Ion diffusion in the presence of a magnetic field

Due to gyration, the transport of charged particles perpendicular to  $\mathbf{B}_0$  in a plasma is fundamentally changed: it is only possible via collisions, allowing to effectively shift the guiding center of their cycloidal motion from one magnetic

field line to another. The characteristic length scale for this transport is given by the respective gyration radius  $r_c$ . Since the transport in direction of the magnetic field is unaffected and typically considered to be the same as in the field free case, the charged particle transport in plasmas exposed to external magnetic fields is in general anisotropic [LL05, Fru09].

Accordingly, the description of ambipolar diffusion provided in chapter 3.4 has to be extended. In consequence of the large difference between the gyration radii of electrons and ions, the behaviour of the field-free ambipolar diffusion is qualitatively inverted: due to the strong magnetic confinement of electrons, their diffusion perpendicular to the magnetic field is strongly slowed down, now effectively limiting the ion diffusion [LL05].

To account for the influence of a magnetic field oriented parallel to the axis of a cylindrical discharge vessel, the provided expressions for the ion transport are adapted. The ion confinement time remains to be given by equation (3.30), while applying a modified mean diffusion length  $\Lambda = \Lambda_{\perp}$  [Möl93]:

$$\frac{1}{\Lambda_{\perp}^2} = (1 + \mu_e \mu_{\text{ion}} B_0^2)^{-1} \left( \frac{2.405}{R_c} \right)^2 + \left( \frac{\pi}{L_c} \right)^2. \quad (3.42)$$

where  $\mu_e = e/(m_e \nu_{e,n})$  and  $\mu_{\text{ion}} = e/(m_{\text{ion}} \nu_{\text{ion},n})$  denote the mobilities of electrons and ions, respectively. In this approximation, the diffusion in axial direction remains unchanged, while the perpendicular diffusion length is effectively elongated. This elongation is proportional to the factor  $B_0^2/n_0^2$ , since both the ion-neutral and the electron-neutral collision frequency depend linearly on  $n_0$ . In the limit of a sufficiently high magnetic field, the perpendicular diffusion of ions is therefore negligible and the ion transport occurs solely parallel to the magnetic field lines due to the strong magnetization of charged particles. If the neutral density increases on the other hand - i.e. due to an increasing pressure - the influence of the magnetic field on the radial ion diffusion is weakened and eventually vanishes.

In consistency with the descriptions of the field-free diffusion in chapter 3.4, the ion transport in the presence of a magnetic field within the discharges investigated in this work is assumed to be given by the described concept of ambipolar diffusion. As already discussed in section 3.4, this is valid at high pressure, but only an approximation at pressures below 1 Pa, since these discharges are located in an intermediate regime between laminar and molecular diffusion. In the free fall regime, the influence of a magnetic field on the ion confinement time is difficult to assess in a 0-dimensional, analytic consideration. If collisions are entirely neglected for simplification, all ions which are created near the radial vessel boundaries

in a layer of the thickness of  $2 \times r_{c,\text{ion}}$  will eventually hit the wall due to their gyration. In contrast, all ions created at the center of the vessel are magnetized and only contribute to the axial transport [Möl93]. If the gyration radius of ions is additionally of the same order as the vessel radius (which applies to the present case), the confinement time of ions strongly depends on the location where the ions are actually created. In consequence, an appropriate consideration of this process has to radially resolve the ionization process itself. This can be provided by spatially resolved numerical approaches, but exceeds the capabilities of 0-dimensional approximations. In consequence, the ion transport in the collisionless regime is neglected in the present case analogous to the field-free case in section 3.4.

### **Effects on the ionization and power balance**

Since an external magnetic field effectively increases the confinement time of ions in the plasma, it influences both the ionization balance as well as the power balance described in chapter 3.4: due to the ionization balance (equation (3.33)), a higher confinement time can result in a decreasing electron temperature in a first approximation, if changes of the neutral particle density can be neglected. According to the power balance, a higher confinement of ions leads to a higher electron density, assuming that both the plasma volume and the power absorbed by the plasma remain constant.

## 4 RF plasma heating and power transfer mechanisms

Discharges driven by radio frequency heating can generally operate in different *modes*, referring to the actual coupling and power transfer mechanism between the externally generated electromagnetic fields and the plasma itself. In the present work, the main focus lies on inductively coupled plasmas (designated as ICPs or discharges operating in the electromagnetic *H-mode*) and plasmas generated due to the excitation of propagating electromagnetic waves, hence operating in the *W-mode*. Frequently, the latter are often referred to as *helicon* plasmas or just *helicons*, in consideration of the associated wave modes. Furthermore, also the operation of RF discharges within the electrostatic *E-mode* is briefly treated in the present case due to their importance during the discharge ignition phase. In principle, all of these RF discharges are driven by applying a sinusoidal AC voltage signal of a generator operating in the megahertz range to an antenna or coil, thereby generating the required electromagnetic fields for plasma ignition and heating. The following descriptions regarding the basics of the RF power transfer are valid for all RF discharges, independent of the actual heating mode of the plasma.

### 4.1 Impedance matching and RF power transfer efficiency

In order to maximize the power transfer from an AC generator to a load, the input impedance  $Z_{\text{load}}$  of the load has to match a characteristic value depending on the applied generator<sup>1</sup>. In the present case the generator is designed to achieve its maximum power output at  $50\ \Omega$ , which is the standard value typically provided by industrial manufacturers. The load consists of the applied antenna or coil,

---

<sup>1</sup>Further and much more detailed information regarding the concepts used in the following is found in textbooks sources treating electromagnetism and RF engineering, e.g. [Dem13, Zim00]

the plasma and a matching network. In the present work, the term *impedance matching* specifically denotes the process of tuning the impedance of this load to the value of  $50\ \Omega$  required by the generator:

$$Z_{\text{load}} = (R_{\text{load}} + iX_{\text{load}}) \stackrel{!}{=} 50\ \Omega, \quad (4.1)$$

with the resistance  $\text{Re}(Z_{\text{load}}) = R_{\text{load}}$  and the reactance  $\text{Im}(Z_{\text{load}}) = X_{\text{load}}$ . The total reactance  $X_{\text{load}}$  includes the reactive contributions of all components of the load, which can be both inductive ( $X = \omega L$ ) and capacitive ( $X = -\frac{1}{\omega C}$ ), with  $L$  denoting the inductivity,  $C$  the capacitance and  $\omega = \omega_{\text{RF}}$  the applied angular frequency. Consequently, impedance matching according to equation (4.1) is achieved for  $\text{Re}(Z_{\text{load}}) = 50\ \Omega$  and  $\text{Im}(Z_{\text{load}}) = 0$ .

In practice, the resistive and reactive contributions of the antenna and the plasma are given for a specific setup or operational scenario. Typically, they do not directly fulfil the required matching equality. By tuning the required matching network, which is basically a resonant circuit consisting of a combination of resistive, capacitive and inductive components, the impedance matching is achieved, and the power  $P_{\text{RF}}$  that is coupled to the load is maximized. In this case, the angular phase shift  $\varphi$  between the voltage and the current delivered to the load is zero. The specific circuits applied in this work are presented in detail in section 6.1.

### RF power transfer efficiency

In case of an ideal match to  $50\ \Omega$ , no reactive power between the generator and the load occurs and the delivered power  $P_{\text{RF}}$  is consumed by the resistive components of the load. On the one hand, this leads to the desired transfer of the power fraction  $P_{\text{plasma}}$  to the plasma, proportional to the so-called *plasma equivalent resistance*  $R_{\text{plasma}}$  [CB11]. On the other hand, a certain share of the delivered power is always dissipated due to the finite resistances of the antenna and the entire RF network. For simplification, those contributions are combined in the present work, thus defining the integral loss resistance  $R_{\text{loss}}$  and the corresponding power losses  $P_{\text{loss}}$ . Subsequently, the delivered power is given by the sum  $P_{\text{RF}} = P_{\text{plasma}} + P_{\text{loss}}$  and the RF power transfer efficiency  $\eta$  can be defined according to

$$\eta = \frac{P_{\text{plasma}}}{P_{\text{RF}}} = \frac{P_{\text{RF}} - P_{\text{loss}}}{P_{\text{RF}}}. \quad (4.2)$$

As already introduced in chapter 2, the RF power transfer efficiency designates the relative fraction of the delivered RF power which is actually deposited in the plasma [CB11]. In opposition to the simple assumption that the RF power delivered by the generator approximately equals the power absorbed by the plasma, it has been conclusively shown by a variety of groups in the past decades that the occurring transmission power losses in RF discharges can in fact be quite substantial [PGA92, Hop94, SNO<sup>+</sup>98, GPA99, Kra08].

### Power losses

In practice, the power losses  $P_{\text{loss}}$  occur on the one hand due to the ohmic heating of all components of a finite resistance leading current. This includes as mentioned the antenna and the components of the matching network itself, as well as all connections and transmission lines that are part of the applied RF setup. On the other hand, also the occurrence of *eddy currents* can contribute to  $P_{\text{loss}}$  and  $R_{\text{loss}}$ , respectively. Eddy currents are current loops within conducting material that are induced by a changing magnetic field. Regarding RF driven discharges, they can occur for example within all metallic parts in the vicinity of the antenna, the RF transmission lines or the matching network. The finite resistance of these surrounding conductors results in ohmic heating due to the induced eddy currents and subsequently in the dissipation of power.

Consequently, the integral resistance  $R_{\text{loss}}$  is expected to display the typical characteristics of AC/DC resistors. First, it is depending on the electrical resistivity of the conducting material and its temperature, whereas in the present work only metallic conductors are of relevance. Accordingly, the resistance increases linearly with the temperature of the conductor in the first order. Second, in the RF range it increases with increasing applied frequency  $\omega_{\text{RF}}$  of the current due to the *skin effect*, which describes the reduction of the effective cross section of a conductor leading an AC current [Jac99]. The assumption of a resistor with a circular cross section leads to the approximation that its AC resistance is proportional to the square root of  $\omega_{\text{RF}}$ .

## 4.2 Inductive heating

The basic principle of an inductive discharge is the induction of an RF current in a plasma by driving an alternating current in an adjacent coil<sup>2</sup>. In the present case, specifically cylindrical ICPs utilizing an external helical coil wrapped around a dielectric tube are considered. By applying an RF voltage in the low MHz range to the coil, a corresponding RF current is driven and the coil acts as an antenna radiating an electromagnetic field. Since the angular excitation frequency  $\omega_{\text{RF}}$  is typically much smaller than the plasma frequency  $\omega_{\text{p}}$ , the charged particles of the plasma are able to follow the RF fields and can, in principle, gain energy. Moreover, the typical assumption for low pressure low temperature ICPs is that solely the electrons respond to the RF field and are heated, while the heavier ions are not able to follow. In case of inductive discharges in hydrogen and deuterium driven at lower frequencies of a few MHz however, this is not necessarily valid, since the heavy particles are in fact considerably light compared to most noble gases, e.g. argon. Consequently, the ion plasma frequency  $\omega_{\text{pi}}$  defined in equation (3.14) can be higher than  $\omega_{\text{RF}}$  and the ions are actually responding to the applied fields. Nevertheless, the descriptions within the following paragraphs adopt the typical assumption that only the electrons are heated in general, while the possibility and relevance of ion heating is specifically addressed afterwards if necessary.

In general, an RF discharge generated in the way described above can operate in both the electrostatic E-mode and the electromagnetic H-mode. The E-mode describes the direct interaction of the charged particles with the E-fields occurring due to the RF voltage applied to the coil<sup>3</sup>. Typically, an ICP starts in the E-mode where the electron density is low and performs a E-H-mode transition when  $n_{\text{e}}$  increases and reaches the critical threshold required for an operation in the H-mode, e.g. by increasing the RF power. In other words, the electrostatic E-mode can be mandatory to achieve the minimum electron density required by an inductively coupled plasma in the first place. If the E-mode is suppressed (e.g. by a Faraday shield [LL05]) or very inefficient (e.g. at low frequency or low antenna impedance resulting in a low voltage drop), additional external sources for ionization like glow discharges or filaments are required to provide a sufficient electron density for an operation in the H-mode. If the E-mode is not suppressed however, real

<sup>2</sup>The following section is mainly based on the descriptions provided by [CB11, LL05].

<sup>3</sup>Discharges typically designed for an operation in the E-mode are known as capacitively coupled plasmas (CCPs) and typically utilize separated electrodes instead of a coil or antenna [CB11]

plasmas can also be operated in an intermediate region where both modes are present simultaneously, particularly at lower power.

### Discharges operating in the H-mode

In the following, an idealized inductive discharge operating solely in the H-mode in steady state is considered qualitatively. The derivation of this electromagnetic model of an inductive discharge is provided in the corresponding literature in extensive detail [LL05, CB11, Jac99]. The exemplary scheme of the considered cylindrical geometry is presented in figure 4.1. The electromagnetic fields excited by the oscillating azimuthal current  $I_{\text{ant}}(t)$  through the coil must obey the Maxwell equations and are indicated respectively. First, an oscillating axial magnetic field  $B_z(r, t)$  is excited in the plasma according to Ampère's circuital law. Faraday's law of induction furthermore requires an oscillating azimuthal electric field  $E_\varphi(r, t)$  oriented in opposing direction of the coil current. Since the excitation frequency is smaller than the plasma frequency, the fields are continuously attenuated as they penetrate into the plasma within the characteristic decay length  $\delta$ , in this case also denoted as the *RF skin depth*. Accordingly, the induced azimuthal E-field leads to an alternating current of charged particles within the skin depth layer at the plasma surface, oriented in the reverse direction of the external coil current. Within this layer, the RF power is deposited and the electrons are heated. The described picture displays significant analogy to a transformer, where the primary coil is the external RF coil and the plasma is regarded as the one-turn secondary coil [PGA92].

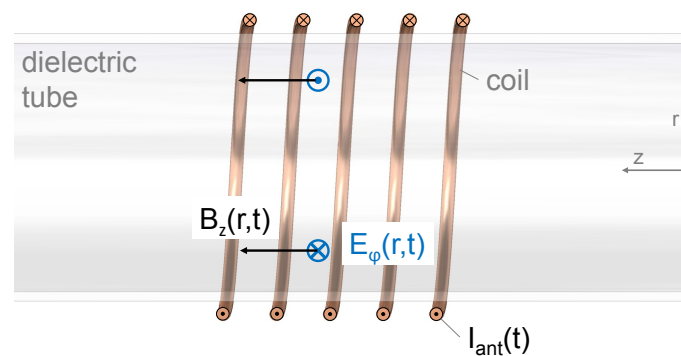


**Figure 4.1:** Schematic of an inductive discharge in a cylindrical vessel and the corresponding electromagnetic fields generated by an alternating RF current running through an external helical coil.

The actual mechanism of power dissipation within the RF skin depth layer of an inductively coupled plasma depends on the specific parameters of the discharge, namely on the collisionality, i.e. the ratio of the collision frequency of electrons with neutrals  $\nu_{\text{en}}$  and the excitation frequency  $\omega_{\text{RF}}$  of the applied generator. As introduced in chapter 3.3, in hydrogen discharges electron-neutral collisions generally imply the collisions of electrons with both atomic ( $\nu_{\text{eH}}$ ) and molecular hydrogen ( $\nu_{\text{eH}_2}$ ), hence  $\nu_{\text{en}} = \nu_{\text{eH}} + \nu_{\text{eH}_2}$ . Collisions of electrons with ions can be neglected due to their lower density. With respect to the operational parameters of a discharge, the electron-neutral collision frequency is mainly depending on the pressure and the gas temperature, which yield together the neutral particle density according to the ideal gas law. In the present case of low pressure plasmas in the range between 0.3 and 10 Pa, the electron-neutral collision frequencies are typically of the order of  $10^7 \text{ s}^{-1}$  and therefore well comparable with the applied angular excitation frequencies, which requires a sensitive distinction between different heating regimes.

### Collisional plasma heating

At sufficiently high pressures, i.e. if the collision frequency  $\nu_{\text{en}}$  of electrons with neutrals is much larger than the applied frequency  $\omega_{\text{RF}}$ , the dominant mechanism of power dissipation in an ICP is *collisional heating*: the electrons follow the applied RF field in the skin depth layer, are accelerated and collide with neutral particles, leading to thermalization via randomization of momentum, and consequently to the deposition of power. It is frequently also referred to as *ohmic* or *joule* heating as it is described in principle by treating the plasma as a conductor and using Ohm's law.

In general, the RF excitation is sinusoidal with the characteristic angular frequency  $\omega_{\text{RF}} = 2\pi/T$  and the oscillation period  $T$ , allowing for a Fourier transformation of all correspondingly oscillating quantities with respect to the time. Subsequently, the time-average power per unit volume absorbed by the plasma  $p_{\text{plasma}}$  can be written as [LL05]

$$p_{\text{plasma}} = \frac{1}{T} \int_0^T \mathbf{J}_p(t) \cdot \mathbf{E}_{\text{RF}}(t) dt = \frac{1}{2} \text{Re}(\tilde{\mathbf{J}}_p \cdot \tilde{\mathbf{E}}_{\text{RF}}^*) = \frac{1}{2} \text{Re}(\tilde{\mathbf{J}}_p^* \cdot \tilde{\mathbf{E}}_{\text{RF}}), \quad (4.3)$$

with the plasma current density  $\mathbf{J}_p$  driven by the induced electric field  $\mathbf{E}_{\text{RF}}$  and their corresponding complex Fourier amplitudes  $\tilde{\mathbf{J}}_p$  and  $\tilde{\mathbf{E}}_{\text{RF}}$ . The asterix

denotes the complex conjugation of the respective quantity. Applying Ohm's law furthermore yields the proportionality [LL05]

$$\tilde{\mathbf{J}}_p = \tilde{\sigma}_p \tilde{\mathbf{E}}_{\text{RF}}, \quad (4.4)$$

where  $\tilde{\sigma}_p$  is the spatially dependent complex plasma conductivity

$$\tilde{\sigma}_p = \frac{\epsilon_0 \omega_{\text{pe}}^2}{i\omega_{\text{RF}} + \nu_{\text{en}}} = \frac{n_e e^2}{m_e (i\omega_{\text{RF}} + \nu_{\text{en}})}. \quad (4.5)$$

Using Ohm's law (4.4) in equation (4.3) now yields the power absorption in the plasma, which is given by

$$p_{\text{plasma}} = \frac{1}{2} \text{Re}(\tilde{\sigma}_p) |\tilde{\mathbf{E}}_{\text{RF}}|^2, \quad (4.6)$$

with the real part of the complex plasma conductivity

$$\text{Re}(\tilde{\sigma}_p) = \frac{n_e e^2}{m_e} \frac{\nu_{\text{en}}}{\omega_{\text{RF}}^2 + \nu_{\text{en}}^2}. \quad (4.7)$$

As a result, the power dissipated in the plasma due to collisional heating is characterized by a quadratic proportionality to the amplitude of the induced RF field and linearly depending on the real part of the plasma conductivity. According to Maxwell's equations,  $|\tilde{\mathbf{E}}_{\text{RF}}|$  is proportional to the amplitude and the frequency of the externally applied current in a first approximation neglecting the influence of the plasma.  $\text{Re}(\tilde{\sigma}_p)$  is depending on the electron density and both the electron collision frequency  $\nu_{\text{en}}$  and the excitation frequency  $\omega_{\text{RF}}$ . The fraction of these frequencies in equation (4.7) yields a characteristic behaviour of  $\text{Re}(\tilde{\sigma}_p)$ , which is displayed in figure 4.2 where the conductivity is plotted versus the electron-neutral collision frequency for different excitation frequencies at a typical electron density of  $10^{17} \text{ m}^{-3}$ . Depending on  $\nu_{\text{en}}$ , the conductivity describes a maximum for  $\nu_{\text{en}} = \omega_{\text{RF}}$ . Accordingly, the position of the maximum is shifted with the applied excitation frequency. For high collision frequencies, i.e. at high pressure, the dependence of  $\text{Re}(\tilde{\sigma}_p)$  on the excitation frequencies vanishes. In the region of lower  $\nu_{\text{en}}$  where the dependence on  $\omega_{\text{RF}}$  appears to be more prominent, the discussed concept of collisional heating is in fact not valid anymore, since  $\nu_{\text{en}} < \omega_{\text{RF}}$ . Based on this characteristic behaviour, the power transfer of an inductive discharge can be optimized in principle by choosing the appropriate excitation frequency for an operation in the desired pressure range. Since the actual electron-neutral collision frequency is dependent on the cross sections of the neutral species at hand, the

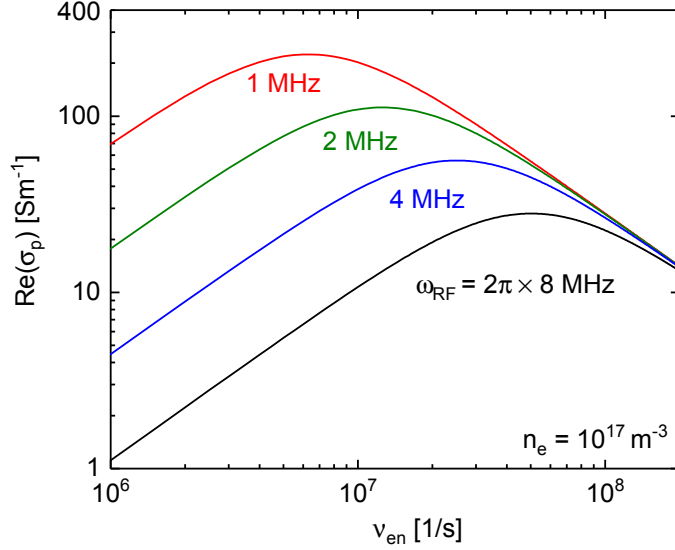


**Figure 4.2:** Real part of the complex plasma conductivity calculated according to equation (4.7) for a varying electron-neutral collision frequency at different excitation frequencies  $\omega_{\text{RF}}$ .

observed behaviour is in general depending on the gas type of the discharge. For inductively coupled noble gas discharges, corresponding investigations have been reported e.g. by [Kra08, KRP<sup>+</sup>16]. As shown therein, a maximum of the RF power transfer can be expected if the electron collision frequency is comparable to the angular excitation frequency.

In the specific case of collisional heating where  $\nu_{\text{en}} \gg \omega_{\text{RF}}$  is valid, the skin depth  $\delta$  is given by the collisional skin depth  $\delta_{\text{coll}}$ , which is defined according to

$$\delta_{\text{coll}} = \sqrt{\frac{2c^2\nu_{\text{en}}}{\omega_{\text{RF}}\omega_{\text{pe}}^2}}, \quad (4.8)$$

where  $c$  is the speed of light in vacuum. This illustrates well the typical behaviour of attenuated electromagnetic fields within in the collisional regime of a plasma: while their penetration depth increases for a higher collision frequency, it decreases for a higher excitation frequency and a higher electron density ( $\omega_{\text{pe}}^2 \propto n_e$ ). The frequency dependent RF skin depth provides also a practical boundary condition for the design of inductively driven discharges: if the skin depth of the RF field exceeds the dimensions of the discharge itself, the potential volume for plasma heating is restricted and the heating efficiency is limited [LL05]. In order to avoid that in practice, the geometry and the desired driving frequency of a discharge

have to be matched up.

Up to now, only the collisional heating of electrons has been considered. As already mentioned however, in hydrogen ICPs an analogous response of ions to the applied RF fields cannot be neglected a priori. At a typical plasma density of about  $10^{17} \text{ m}^{-3}$  and an excitation frequency of 1 MHz, the ion plasma frequency  $\omega_{\text{pi}}$  is in fact more than one order of magnitude larger than  $\omega_{\text{RF}}$ . In consequence, the ions can indeed follow the RF field. In order to estimate the relevance of RF power deposition via collisional ion heating however, the ion-neutral collision frequency has to be evaluated in analogy to the case of electrons. Therefore, the collision of the hydrogen ion species  $\text{H}^+$ ,  $\text{H}_2^+$  and  $\text{H}_3^+$  with neutral particles is considered based on cross section data provided by [KS98, Phe90]. Assuming ion temperatures in the range of the gas temperature (500 to 1000 K), this yields ion-neutral collision frequencies which are typically between one and two orders of magnitude lower than  $\omega_{\text{RF}}$ . Consequently, the requirement for collisional ion heating is clearly missed and its contribution to the total RF power deposition can be well neglected compared to the contribution of electron heating.

### Collisionless (stochastic) heating

In the low pressure region of inductive discharges, where the collision frequency of electrons with neutrals is smaller than the angular excitation frequency, collisional heating is ineffective. However, inductive discharges are well capable of achieving considerably high densities in this low pressure region nonetheless, which is due to a process typically referred to as *collisionless heating* [Wei67, Tur93, LL05]. Frequently it is also called *stochastic heating*, due to its analogy to the non-local heating mechanism of the same denotation known from capacitive discharges.

In principle, collisionless heating is a warm plasma effect, i.e. requiring a certain kinetic energy of the electrons (and assuming a Maxwellian EEDF subsequently a certain electron temperature  $T_e$ ) [Tur93]. Considering the opposite case of a cold collisionless plasma ( $T_e = 0$ ), each electron samples the induced electric field at a single location in the RF skin depth layer of the width  $\delta$ . Since the fields vary harmonically in time, the integral field seen by the electrons averages to zero everywhere and no energy can be gained. However, if the electrons have a finite temperature  $T_e > 0$ , they are in thermal motion and sample the field along their trajectories. Since the induced RF field is non-uniform and concentrated within the skin depth layer at the plasma surface, it does not average to zero along a trajectory in general. If the transit time of electrons through the skin depth layer

is much shorter than the RF period, the electrons are able to gain net energy from the field in consequence. The corresponding inequality to be fulfilled is given by [Tur93]:

$$\omega_{\text{RF}} \delta \lesssim \sqrt{k_{\text{B}} T_{\text{e}} / m_{\text{e}}}. \quad (4.9)$$

In analogy to collisional heating at higher pressures, this process can also be qualitatively understood in the form that bulk plasma electrons are "colliding" with the oscillating fields in the RF layer, as they are accelerated and subsequently thermalized [LL05]. Therefore, a *stochastic collision frequency*  $\nu_{\text{stoc}}$  can be defined analogous to the electron-neutral collision frequency. In order to calculate  $\nu_{\text{stoc}}$  for the present case, an analytical approach proposed by [VLD<sup>+</sup>95] is followed.

First, rewriting the inequality given in equation (4.9), a characteristic parameter  $\alpha$  is introduced:

$$\alpha := \frac{4\delta^2 \omega_{\text{RF}}^2}{\pi v_{\text{e}}^2}, \quad (4.10)$$

where  $v_{\text{e}}$  is the mean electron velocity. This parameter describes the square of the fraction of the transit time of a thermal electron through the skin depth  $\delta$  and the RF period. Taking into account the parameters  $\omega_{\text{RF}}$  and  $v_{\text{e}}$ , a distinction between different expressions for the stochastic collision frequency based on the resulting value of  $\alpha$  has to be made.

In the first case, the applied frequency is much lower than the inverse electron transit time, yielding  $\alpha \ll 1$ . Consequently, the stochastic collision frequency and the corresponding skin depth  $\delta$  in this regime are given by

$$\nu_{\text{stoc}} = \frac{1}{2\pi} \frac{v_{\text{e}}}{\delta} \quad \text{and} \quad \delta = \left( \frac{c^2}{\omega_{\text{pe}}^2} \frac{v_{\text{e}}}{\pi \omega_{\text{RF}}} \right)^{1/3}. \quad (4.11)$$

The above expression for the skin depth is equally derived by [Tur93, LL05], and frequently called the *anomalous skin depth*.

In the second case considered here, the applied frequency is roughly in the order of the electron transit frequency, yielding a value for  $\alpha$  in the range of  $0.03 \leq \alpha \leq 10$ . In consequence,  $\nu_{\text{stoc}}$  and  $\delta$  are given by

$$\nu_{\text{stoc}} = \frac{1}{4} \frac{v_{\text{e}}}{\delta} \quad \text{and} \quad \delta = \frac{c}{\omega_{\text{pe}}}. \quad (4.12)$$

This expression for the skin depth  $\delta$  is commonly referred to as the *inertial skin depth*, as it approximates the attenuation of the RF field to be determined solely

by the inertia of the plasma electrons without the occurrence of any collisions. In the case of  $\alpha \gg 1$ , the applied frequency is much higher than the electron transit frequency and collisionless heating of electrons is no longer possible. Depending on the individual plasma parameters of the discharges investigated in the present work, the parameter  $\alpha$  can be calculated, which allows to identify the valid expression for the stochastic collision frequency.

However, for hydrogen discharges driven at low excitation frequencies the provided description requires some additional remarks. In the derivation of the concept described above, it is assumed that the ions do not respond to the RF fields [VLD<sup>+</sup>95]. As already mentioned, this is in contradiction to the discharges at hand. Since up to now no resilient description of stochastic heating in the regime of  $\omega_{\text{RF}} < \omega_{\text{pi}}$  is available to the authors knowledge, the provided concept assuming stationary ions is applied nonetheless. This is justified, since also the collisionless heating of ions can be neglected, assuming an analogous mechanism compared to the electrons: the transit time of ions through the RF skin depth layer is about 100 times longer than the duration of an RF period at 1 MHz, due to their low temperature between 500 and 1000 K. Consequently, the ions follow the harmonic oscillation of the induced field, but without any relevant gain of energy, in analogy to the collisional case at higher pressure. Thus, the typical assumption in low pressure low temperature ICPs that electrons are the only species with a relevant contribution to the total power absorption holds in the present case, independent of the collisionality regime.

In order to account for both collisional as well as collisionless heating of electrons simultaneously, an effective collision frequency  $\nu_{\text{eff}} = \nu_{\text{en}} + \nu_{\text{stoc}}$  can be defined. The validity of this assumption which considers both local and non-local heating mechanisms in inductive discharges over a broad collisionality regime has been conclusively shown by [LL05, VLD<sup>+</sup>95]. The plasma conductivity given in equation (4.7) can then be written as

$$\text{Re}(\tilde{\sigma}_{\text{p}}) = \frac{n_{\text{e}}e^2}{m_{\text{e}}} \frac{\nu_{\text{eff}}}{\omega_{\text{RF}}^2 + \nu_{\text{eff}}^2} \equiv \sigma_{\text{eff}}, \quad (4.13)$$

thus defining the effective plasma conductivity  $\sigma_{\text{eff}}$ . According to the equations (4.3) and (4.13) the power absorption of the plasma is - in a simplified 0-dimensional consideration neglecting the influence of the electric field  $\tilde{\mathbf{E}}$  as well as spacial variations of the involved plasma parameters - proportional to  $n_{\text{e}}$  and the fraction  $\nu_{\text{eff}}/(\omega^2 + \nu_{\text{eff}}^2)$ , that reaches its maximum at  $\nu_{\text{eff}} = \omega_{\text{RF}}$  analogously to the behaviour of  $\nu_{\text{en}}$  presented in figure 4.2.

## 4.3 Low field wave heating

As already introduced in chapter 2.3, wave heating within magnetized low pressure discharges in the RF range relies on the excitation and propagation of certain wave modes, conventionally denoted and summarized as *helicons*. The following description of the conditions and mechanisms of wave propagation, excitation and damping is mainly focused on the low field regime ( $B \lesssim 12$  mT) of relevance for the present work<sup>4</sup>.

### 4.3.1 Helicon and Trivelpiece-Gould waves

As discussed in section 3.1, in an unmagnetized plasma electromagnetic waves of a frequency  $\omega$  smaller than the plasma frequency cannot propagate due to the dynamic screening via free charge carriers. The application of an external magnetic field changes this situation fundamentally, as the gyration of charged particles not only changes the plasma transport but also enables the propagation of a variety of different electromagnetic waves within the plasma at low frequencies of  $\omega \ll \omega_{pe}$ . Among these waves are also the desired helicons, which will be further discussed in the following<sup>5</sup>.

#### Frequency range and unbounded dispersion relation

The frequency range where the excitation of helicon waves is possible is located at the low-frequency limit of electron cyclotron waves [CB11]. Considering the basic assumptions that the ion gyration is sufficiently slow to be neglected and that the electron inertia is small leads to the condition [CB11, ST96, Che15]

$$\omega_{ci} \ll \omega \ll \omega_{ce} \ll \omega_{pe}. \quad (4.14)$$

In practice, the excitation frequency and the externally applied magnetic field have to be adjusted, accordingly. Usually, excitation frequencies in the RF range of some MHz and magnetic fields of the order of a few up to 100 mT fulfil this inequality well, as in the present case: At typical parameters of  $n_e \approx 5 \times 10^{17} \text{ m}^{-3}$  and  $B_0 = 8$  mT in hydrogen ( $m_{ion} \approx 2 \text{ u}$ ) at an excitation frequency of 4 MHz,

<sup>4</sup>A description of helicon sources operated in the high field/high power regime is discussed by various sources in the corresponding literature. A comprehensive review is for example provided by [BC97b, CB97]

<sup>5</sup>General information regarding waves in (magnetized) plasmas is provided e.g. by [Sti92].

those frequencies are

$$\omega_{ci} \approx 10^5 \text{ s}^{-1} \ll \omega = 2.5 \times 10^7 \text{ s}^{-1} \ll \omega_{ce} \approx 10^9 \text{ s}^{-1} \ll \omega_{pe} \approx 10^{10} \text{ s}^{-1}.$$

Solving the electromagnetic wave equation in this frequency range while applying the *cold plasma approximation*<sup>6</sup> and taking into account electron collisions yields the dispersion relation  $k(\omega)$  of *quasi-longitudinal R waves* [Sti92]:

$$k^2 = \frac{\omega \omega_{pe}^2}{c^2(\omega_{ce} \cos(\theta) - \omega \xi)}. \quad (4.15)$$

This relation describes waves of the form  $e^{i(m\theta + kz - \omega t)}$  with the squared total wave number  $k^2 = k_{\parallel}^2 + k_{\perp}^2$ , the angle  $\theta$  between  $\mathbf{B}_0 = B_0 \hat{z}$  and the wavenumber vector  $\mathbf{k}$ , i.e.  $\cos(\theta) = k_{\parallel}/k$  and the azimuthal mode number  $m$ . The term  $\xi = 1 + i(\nu_{\text{coll}}/\omega)$  accounts for wave damping due to electron collisions with neutrals and ions. In correspondence to the conventional notion, the wave numbers  $k_{\parallel}$  oriented parallel to the magnetic field are also referred to as *longitudinal*, while those in perpendicular direction ( $k_{\perp}$ ) are called *transversal*. The wave modes described by this dispersion relation are also known as *whistlers*, in reference of naturally occurring electromagnetic disturbances due to lightning flashes in the earth's ionosphere [Che15, CB11].

For the particular case of cylindrically bounded waves at low frequencies of  $\omega \ll \omega_{ce}$ , equation (4.15) now describes the dispersion of the desired helicon waves in its original form without any further limitations. General information about the properties of these waves can be found in a variety of publications, which are comprehensively reviewed by [BC97b, CB97, Che15] and subject to several textbooks treating RF plasma heating, i.e. [LL05, CB11]. In the following, only the particular case of waves excited in an axially limited device will be discussed further, as it is of relevance for the present work.

### Wave modes in axially bounded plasmas

If an axially bounded plasma is considered, e.g. in case of a cylindrical device of the length  $L_c$ , it acts as a (plasma filled) cavity and a longitudinal quantization condition for the waves is imposed. Following the descriptions of [ST96] for low aspect ratio sources where the antenna length is comparable to the device length,

<sup>6</sup>The cold plasma approximation implies that electrons and ions are motionless in the unperturbed state, i.e. they have zero temperature. A comprehensive description of this model is provided e.g. by [Sti92].

the longitudinal wavenumber is defined by

$$k_{\parallel} = l \frac{\pi}{L_c} \quad \text{with} \quad l \in \mathbb{N}. \quad (4.16)$$

Since  $k_{\parallel} = 2\pi/\lambda$  with the wavelength  $\lambda$ , the integer  $l$  denotes the number of longitudinal half wavelengths within the device. Accounting for this boundary condition, the dispersion relation in equation (4.15) can be solved with respect to the transversal wavenumber  $k_{\perp}$  [ST96]:

$$k_{\perp\pm}^2 = k_{\parallel}^2 \frac{1}{2\xi^2 \alpha^2 \beta^2} (1 - 2\xi\alpha - 2\xi^2 \alpha^2 \beta^2 \pm \sqrt{1 - 4\xi\alpha}), \quad (4.17)$$

with the parameters

$$\alpha = \left( \frac{\omega_{pe}\omega}{\omega_{ce}} \frac{L_c}{lc\pi} \right)^2 \quad \text{and} \quad \beta = \frac{\omega_{ce}}{\omega\omega_{pe}^2} \left( \frac{lc\pi}{L_c} \right)^2. \quad (4.18)$$

It can be seen that equation (4.17) describes two solutions, i.e. two different wave modes exist that fulfil the imposed boundary conditions in the discussed frequency range. The first one, designated by the minus sign, is again the helicon wave. The second one is corresponding to the plus sign and commonly referred to as the *Trivelpiece-Gould (TG) wave*. Typically, helicon waves are weakly damped, have a longer radial wavelength and are able to penetrate the plasma volume and propagate along the magnetic field lines. The TG waves on the other hand are highly damped, of a short radial wavelength and therefore localized at the plasma boundary [ST96, Che15].

### Conditions for helicon and TG wave propagation

In order to qualitatively assess the typical range of the parameters  $B_0$  and  $n_e$  that permit the propagation of helicon and TG waves, the collisionless case is considered in a first approximation, i.e.  $\nu_{\text{coll}} = 0 \Rightarrow \xi = 1$  [ST96]. In figure 4.3, the characteristic regions of wave propagation depending on the electron density and the magnetic field are illustrated for fixed values of  $\omega$  and  $k_{\parallel}$ . In order to allow for wave propagation,  $k_{\perp\pm}^2$  in equation (4.17) has to be real and positive. This requires the term under the square root to be positive, yielding the condition  $\alpha < 1/4$ . If  $\alpha$  exceeds  $1/4$ , the electron density is too high at a given magnetic field,  $k_{\perp\pm}^2$  is complex and the plasma is opaque for both modes. Resolving the expression for  $\alpha$  in equation (4.18) while setting  $\alpha = 1/4$  yields an upper limit  $n_{\text{max}}$  for the electron density:

$$n_{\max} = \frac{1}{4} \frac{\epsilon_0 B_0^2}{m_e} \left( \frac{lc\pi}{\omega L_c} \right)^2 \quad (4.19)$$

Above this density, neither helicon nor TG waves can propagate. This case corresponds to the area in top-left of figure 4.3. Since equation (4.19) yields  $n_{\max} \propto B_0^2$ , it is limited by the depicted parabola.

To allow for a propagation of helicon waves a second condition has to be met in order to fulfil  $k_{\perp-}^2 > 0$ : the expression in the brackets of equation (4.17) has to be positive. This leads to the requirement  $\beta < 1$ , if the frequency ranges introduced in equation (4.14) are accounted for. This second condition corresponds to a minimum density  $n_{\min}$  which is needed for the propagation of helicons, which is gained by rewriting the expression for  $\beta$  in equation (4.18) with respect to the density assuming the limit  $\beta = 1$ :

$$n_{\min} = \frac{B_0 \epsilon_0}{e m_e} \left( \frac{lc\pi}{L_c} \right)^2. \quad (4.20)$$

The minimum density increases linearly with  $B_0$ , as depicted in figure 4.3. If the plasma is not dense enough, it is opaque for helicons. In summary, helicon waves can only propagate for  $n_{\min} < n_e < n_{\max}$ . For TG waves on the other hand, no minimum density condition is present and propagation is possible for  $n_e < n_{\max}$ .

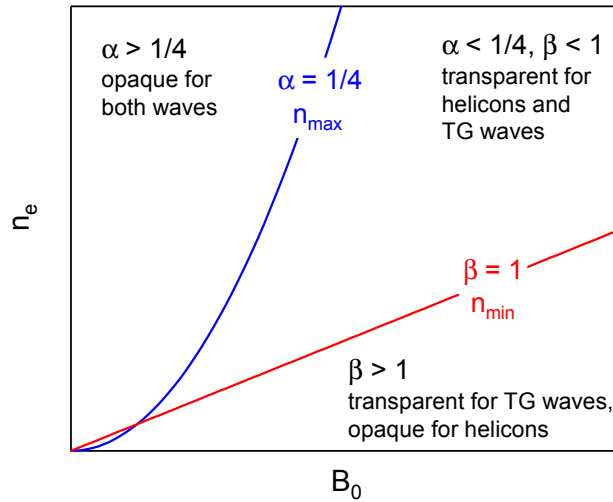


**Figure 4.3:** Conditions for the propagation of helicon and Trivelpiece-Gould waves in an axially confined plasma depending on the electron density and the applied magnetic field for fixed frequency and longitudinal wavenumber according to [ST96].

### 4.3.2 Antenna coupling and heating mechanism

As described in the previous chapter, the presence of a static magnetic field  $\mathbf{B}_0$  enables the propagation of helicon and Trievelpiece-Gould waves in the radio frequency range. In contrast to inductive heating, the exact mechanisms responsible for both the excitation of these waves as well as for the power transfer between the waves and the plasma particles are not entirely understood up to now and still the subject of active experimental and theoretical research [LL05, CB11, Che15].

#### Antenna coupling and wave excitation

In order to excite the described wave modes, particular antennas are utilized. A comparison of the properties and capabilities of different helicon antennas is for example provided by [KB96]. In the present work, only the so-called *Nagoya type III* antenna [WHK<sup>+</sup>78] is utilized, which is known to preferably excite wave modes characterized by the azimuthal wave numbers  $m = \pm 1$  [Che15, KB96].

Figure 4.4 shows the Nagoya type III antenna in a schematic illustration. It consists of two rings which are closed around a cylindrical dielectric discharge vessel. The rings are connected to each other by a long horizontal leg on top. Via two shorter legs at the bottom of the rings, the antenna is connected to the RF generator and the matching circuit. Considering a fixed point in time during operation, e.g. in the rising RF half-cycle, a current  $I_{\text{ant}}$  is flowing through the antenna following its geometry, which is illustrated by the black arrows. Assuming an ideal antenna, the RF current splits in half at the end rings. Effectively, the Nagoya antenna can be seen as a one turn coil. In consequence, the same description of the electromagnetic fields as in case of the helical ICP coil in section 4.2 is valid here, yet in a different orientation: the magnetic field occurring due to Ampère's law is oriented perpendicular to the cylinder axis along  $\hat{y}$ . The induced electric field  $\mathbf{E}_m$  is generated in opposition to the rising antenna current along the rings and legs of the antenna, as illustrated by the red arrows in figure 4.4. As a result, the Nagoya antenna can also be operated in the inductive mode, e.g. if the external magnetic field is switched off.

In order to illustrate how the Nagoya antenna is capable to couple to and excite the desired wave modes due to its geometry, the reaction of the plasma electrons on the generated fields has been specifically considered. For a qualitative discussion, the description provided by [Che15, LL05] is followed: the induced field  $\mathbf{E}_m$  along the top connection and the bottom legs moves electrons from one end ring of

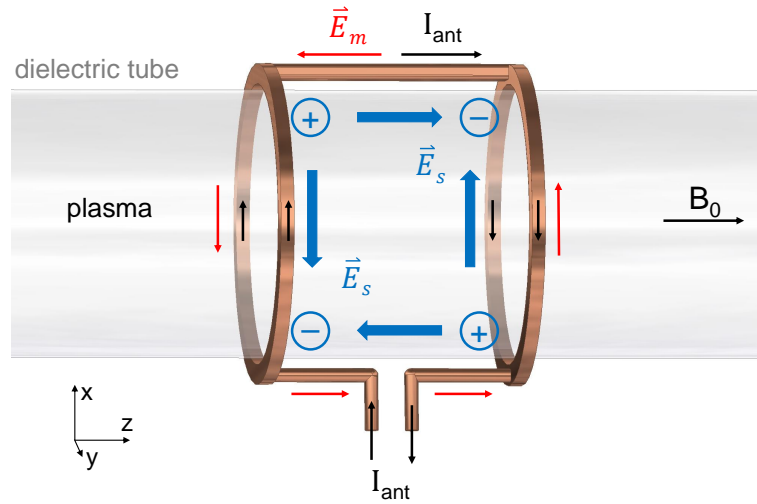


**Figure 4.4:** Scheme of the Nagoya type III antenna in operation at a fixed point in time. Indicated is the current flowing through the antenna (black), the induced electric field  $\mathbf{E}_m$  (red) and the space charges and electric fields generated due to the reaction of the plasma electrons (blue).

the antenna to the other, leading to positive and negative space charges near the antenna rings as indicated by  $\oplus$  and  $\ominus$ . Those charges give rise to an electric field  $\mathbf{E}_s$  indicated in blue, which eventually stops the electron flow along  $\mathbf{B}_0$ . Due to the alternating direction of the current through the top and bottom legs, inverse space charge patterns build up. In turn, these charges create a transverse, quasistatic  $\mathbf{E}$ -field oriented perpendicular to  $\mathbf{B}_0$ . This field points in the same direction as the field  $\mathbf{E}_m$  induced at the antenna rings and thus, effectively amplifies it. These amplified fields are considered responsible for the capability of the antenna to couple to the desired wave modes [Che15, LL05]. In particular the  $m = \pm 1$  helicon modes are excited, as their transverse mode patterns [Che91] resemble well the amplified transverse fields.

### Wave damping and power transfer mechanisms

In general, the energy transfer from excited waves to the plasma relies on the same basic mechanism that has already been described for the inductively heated plasmas in section 4.2: The charged plasma particles, dominantly the electrons, react to the excited electric fields (in this case those of the propagating waves) and are accelerated. Subsequently, collisional (or collisionless) processes lead to the randomization of momentum and thus, to power absorption by the plasma as the propagating waves are damped.

In contrast to the well understood ICPs, there is up to now no universally applicable description for the heating mechanism in the low field regime of RF helicon discharges if only helicon wave modes are considered. This is mainly due to the fact that helicon discharges are usually operated at relatively low pressures ( $p < 1$  Pa). In this region, the probability for electron-neutral collisions alone is too low for collisional damping of helicons and thus, for efficient ohmic heating [CB11, CB97, BC97b]. In the particular case of highly ionized helicon discharges ( $n_e \gg 10^{18} \text{ m}^{-3}$ ) operated in the high power/high field regime, this shortcoming can be compensated by the inclusion of electron-ion collisions [LL05, CB11]. However, this does not apply to the discharges of moderate density driven in the low field regime, which are of relevance for the present work: according to [CB11, Che91], the collision frequency  $\nu_{ei}$  of electrons with singly charged ions can be estimated by

$$\nu_{ei} \approx 2.9 \times 10^{-11} n_e \left( \frac{k_B T_e}{e} \right)^{-3/2}. \quad (4.21)$$

Typical parameters characterizing the discharges in the present work are  $T_e = 5 \text{ eV}$  and  $n_e = 5 \times 10^{17} \text{ m}^{-3}$ , which yields  $\nu_{ei} \approx 1 \times 10^6 \text{ s}^{-1}$ . This is about one order of magnitude lower than the typical frequency of electron-neutral collisions at low pressure and thus, much lower than required for efficient collisional wave damping [CB11].

Since collisional damping of helicons is insufficient to explain the high ionization capability in the low field regime, different collisionless mechanisms have been invoked [BC97b, CB97]. One of the most thoroughly investigated processes is *Landau damping*. Initially suggested by [Che91] as a possible heating mechanism for helicons, it was adopted by many authors [LBB<sup>+</sup>91, ZB91, CB97] and can also be found in textbook sources [LL05, CB11]. Its basic assumption is that fast electrons of a thermal velocity comparable to and in direction of the phase velocity of helicon waves are effectively accelerated by the propagating waves. However, investigations by [MER97, CB99] showed experimentally that the number of fast electrons is insufficient to explain the high power absorption in a helicon discharge, which eventually lead to the abandonment of this theory [Che15].

In consequence, the excitation of the Trivelpiece-Gould wave modes introduced in section 4.3.1 is frequently considered to be the dominant source of the observed plasma heating in the low field regime [Che15, LL05, ST96]. In order to assess the role of these modes, the damping of TG and helicon waves is discussed in the following based on the description provided by [ST96].

### Damping rates of helicon and TG waves

In case of collisional wave damping ( $\nu_{\text{coll}} > 0$ ), the transversal wavenumbers  $k_{\perp\pm}$  given by the dispersion relations of helicon and TG waves introduced in equation (4.17) become complex. The real transversal wavenumbers  $k_{\pm}$  are then given by  $k_{\pm} = \text{Re}(k_{\perp\pm})$ , whereas spatial damping rates  $\kappa_{\pm}$  are obtained from  $\kappa_{\pm} = \text{Im}(k_{\perp\pm})$ . If a parameter region of the plasma density and the magnetic field is assumed where both helicons and TG waves can propagate well (i.e.  $\alpha, \beta^2 \ll 1$ ) at a low collisionality ( $\nu_{\text{coll}} \ll \omega$ ), simplified expressions of these quantities can be obtained that allow for a qualitative discussion [ST96].

For the helicon waves (-), this yields

$$k_{-} = k_{\parallel} \frac{1}{\beta}, \quad (4.22)$$

$$\kappa_{-} = k_{\parallel} \frac{\nu_{\text{coll}}}{\omega} \frac{\alpha}{\beta}. \quad (4.23)$$

Considering typical experimental conditions [ST96] in a cylindrical plasma device with a radius  $\rho$  yields that the transversal wavelengths of helicons are in the order of the plasma radius, i.e.  $k_{-}\rho \geq 1$ . The damping lengths however may strongly exceed the vessel dimensions, as  $\kappa_{-}\rho \ll 1$ . This corresponds to the statement already provided above that helicons are only weakly damped.

Applying the analogous assumptions for the TG waves (+) provides the expressions

$$k_{+} = k_{\parallel} \frac{\omega_{\text{ce}}}{\omega}, \quad (4.24)$$

$$\kappa_{+} = -k_{+} \frac{\nu_{\text{coll}}}{\omega}. \quad (4.25)$$

At typical conditions, the transversal wavelengths and the damping length of TG waves are less than the plasma radius, as  $k_{+}\rho \gg |\kappa_{+}|\rho > 1$ . In contrast to helicon waves, TG waves strongly decay across the magnetic field and deposit their energy mainly at the plasma boundary and can therefore dominate the absorption of RF power in the low field regime [Che15]. Numerically obtained examples of the transversal wave profiles and damping lengths of both helicon and TG waves are provided by [Che15].

In practice, low field discharges that mainly rely on the power deposition via TG waves exhibit radial plasma distributions that are not unlike those observed in

cylindrical ICPs, where the power deposition also occurs at the plasma boundaries. In high field helicon discharges on the other hand, where the plasma heating is mainly dominated by helicon wave modes, the radial plasma distribution usually exhibits a significantly different behaviour. In such discharges, the plasma heating occurs not at the boundaries, but within the plasma volume due to the long damping lengths of helicons. Due to the strong magnetization of charged particles, the plasma is radially concentrated in a small area at the cylinder axis and broadly distributed parallel to the applied magnetic field. Examples for the spatial profiles in these discharges can be found e.g. in [BC97a].

### **The low field peak**

Helicon plasma sources operated at low magnetic fields are known to exhibit a local enhancement of the electron density or the RF power transfer efficiency at a certain  $B_0$  of a few mT. This phenomenon is commonly referred to as the *low field peak*. Since its first observation by [Che92], it has been reported and investigated frequently both in argon [DJB<sup>+</sup>96, Cho06] as well as in hydrogen discharges [SMO<sup>+</sup>15, BGR<sup>+</sup>16]. It is usually explained by the reflection of helicon waves from the axial endplates of a cylindrical vessel, leading to constructive interference and thus, to an increased power deposition and ionization [Che15].

## 5 Experimental setup and diagnostics

### 5.1 The CHARLIE experiment

The investigation of the RF driven hydrogen and deuterium plasmas is carried out at the laboratory experiment CHARLIE (C**oncept** studies for **Helicon Assisted RF Low pressure Ion sourceEs**). A schematic of the experimental setup is presented in figure 5.1. The plasma is generated within a cylindrical quartz vessel which has a length of 40 cm, an outer diameter of 10 cm and a wall thickness of 0.5 cm. At both ends the cylinder is attached to the vacuum system. As depicted on the left of figure 5.1, one end is connected to the gas feed line via a stainless steel transition piece. The latter effectively serves as an end plate for the discharges, since it also contains a vertical stainless steel grid in order to reduce the expanse of the discharge into the vacuum system. Additionally, an  $\text{Al}_2\text{O}_3$  ceramic ring is installed to shield a majority of the metal surfaces from the plasma. Both the grid and the ceramic ring serve as countermeasures to suppress the sputtering of metal particles by the plasma, which can occur especially if the discharge is operated in a regime where capacitive coupling is not negligible.

At the opposite end of the discharge tube, a cylindrical stainless steel vacuum chamber is mounted which serves as the expansion region for the generated plasma. It is 25 cm long and has a diameter of 31.8 cm. The dimensions of the expansion region are therefore well comparable to those of the IPP prototype source introduced in chapter 2. As indicated in figure 5.1, the two-stage pumping system, which consists of a rotary vane pump and a turbo molecular pump, is connected to the chamber. This allows to evacuate the whole system to a background pressure of some  $10^{-6}$  mbar, which is monitored by a compact pressure gauge consisting of a Pirani gauge and a cold cathode gauge connected to the expansion chamber.

During gas and plasma operation, the absolute working pressure is measured by a capacitive pressure gauge insensitive of the gas type which is also connected

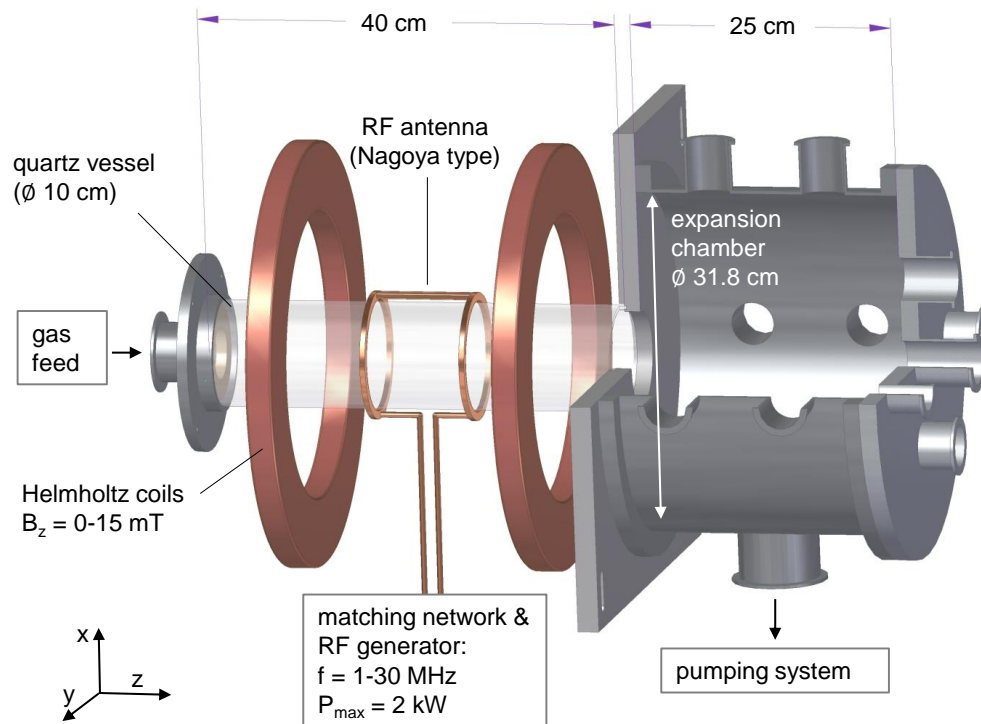


**Figure 5.1:** Schematic of the experimental setup of CHARLIE.

to the chamber. The working pressure is adjusted by reducing the pumping speed via an in-line valve installed between the chamber and the pumping system. At a fixed flow rate of 5 sccm in H<sub>2</sub> and D<sub>2</sub> operation adjusted by a mass flow controller, this allows in general for filling pressures within the range of 0.2 to 10 Pa, whereas the lower limit is determined by the pumping rate and the higher limit is set by the upper measurement limit of the capacitive pressure gauge. Some of the investigations presented within this work have been conducted in a prior configuration of the experiment, lacking the expansion chamber. In this case, at both ends of the discharge vessel identical transition pieces like the one depicted on the left end of the tube were installed.

The RF discharges investigated in this work are generated via one of two different antennas which is installed around the center of the discharge vessel. In figure 5.1, the Nagoya type antenna utilized for the operation of wave assisted discharges is shown exemplary. The helical five-turn coil which is used for the inductive discharges is installed at the identical position. Both antennas are also

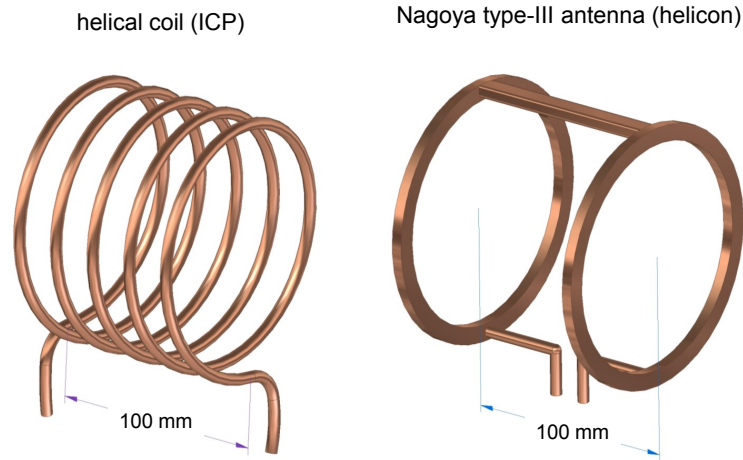


**Figure 5.2:** Schematic of the two RF antennas which are utilized at CHARLIE.

depicted in figure 5.2. Both are of an aspect ratio of one, with a diameter and length of each about 10 cm. The helical ICP coil is a bent copper tube with an outer diameter of 6 mm. The Nagoya antenna is manufactured from solid copper with a rectangular cross section of  $6 \times 9$  mm. The antennas are connected via an impedance matching network to the RF generator (RFG-1/30-2000, Barthel HF-Technik). This generator is capable of delivering RF powers up to 2 kW at a frequency ranging from 1 to 30 MHz, which can be adjusted in steps of 10 kHz. Details regarding the required impedance matching network and the discharge ignition procedure are provided in section 6.1.

The external magnetic field, which is directed parallel to the cylindrical axis of the discharge vessel ( $\hat{z}$ ), is generated by a pair of Helmholtz coils (380 windings and 18 cm inner radius each). The maximum field strength in continuous wave operation is about 15 mT, limited by ohmic heating of the coils which are not actively cooled.

### Diagnostic setup

The investigations presented in this work focus on the determination of the RF power and efficiency and on the plasma parameters within the discharge vessel itself, which is typically the defining region for the plasma heating mechanism. Plasma parameters in the expansion region are therefore not specifically investigated. In figure 5.3 the general setup of the applied diagnostic systems at CHARLIE is depicted. A specific description of the diagnostics and the subsequent evaluation of the plasma parameters is provided in the following section 5.2. The diagnostic

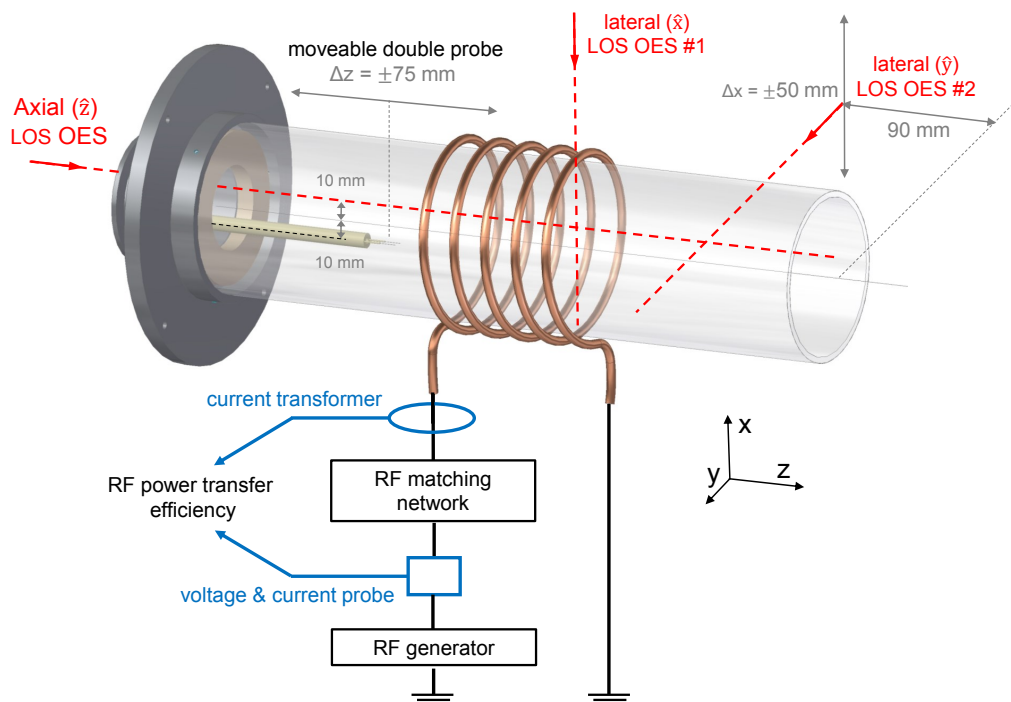


**Figure 5.3:** Arrangement of the diagnostic systems at CHARLIE. Exemplary, the ICP coil is depicted; the diagnostic setup with the Nagoya antenna is identical.

setup for both antennas (ICP and Nagoya type) is identical, in figure 5.3 the helical ICP coil is exemplarily shown.

In order to obtain the required parameters of the RF circuit, two measurement devices are utilized. First, a current transformer (CT-FO.1-BNC, Magnelab) is installed around the connection between the matching circuit and the RF antenna, which is connected to a digital oscilloscope (TDS-3004B, Tektronix) and measures the RF current  $I_{\text{ant}}$  flowing through the antenna. Second, an in-line voltage and current probe (V/I Probe 350, MKS ENI Products) is installed between the RF generator and the matching network and allows for the time resolved measurement of the voltage and current output of the generator and the phase angle between both. Consequently, the V/I Probe provides an in-situ monitoring of the impedance matching as well as a value for the delivered RF power. The combination of the antenna current and the RF power measurement allows for the quantification of the RF power transfer efficiency.

Line of sight averaged plasma parameters of the generated discharges are measured via optical emission spectroscopy (OES). At CHARLIE, three different lines of sight (LOS) are utilized.

The axial LOS is oriented parallel and in 1 cm distance to the cylinder axis. The emitted radiation of the discharge passes through a quartz window installed behind the transition piece and is collimated by a non-dispersive focusing mirror into a fiber optic. Additionally, an aperture stop of 10 mm is used to limit the collected solid angle. The optical fiber guides the light towards a high resolution spectrometer (Acton Series SP-2756i, grating with 1800 grooves/mm, Princeton Instruments PIXIS:2KB CCD camera). The spectrometer is wavelength and intensity calibrated within the wavelength region of 300 - 850 nm. The full width at half maximum  $\Delta\lambda_{\text{FWHM}}$  of the Gaussian apparatus profile is in the range from 18 to 20 pm in the wavelength region of interest between 400 and 650 nm. Wavelength calibration was done by recording emission lines of known wavelength using mercury and rare gas lamps. The intensity calibration of the system is performed via an Ulbricht sphere serving as a diffuse and homogeneously emitting secondary calibration standard. Since the absolute emission of the Ulbricht sphere is known, a calibration factor  $f(\lambda)$  for the spectroscopic system can be derived by dividing the known emission of the sphere by the emission measured with the present spectroscopic system. Further details of the applied calibration procedure are provided e.g. by [Bri11, Fri13]. Along the axial line of sight, the absolute intensities of the atomic Balmer lines and rotational lines of the molecular Fulcher band are detected. The length of the LOS is set to be 40 cm, assuming that the plasma emission originating from the expansion region is negligible. The measured intensities provide the input for the applied collisional radiative models, which allow for a determination of line of sight averaged values of the plasma parameters.

The first lateral line of sight (#1) is aligned in the central region of the discharge directly above the antenna. The light is collected and transferred via an optical fiber to a wavelength and intensity calibrated survey spectrometer (Plasus Emicon HR, 300-850 nm,  $\Delta\lambda_{\text{FWHM}} \approx 0.3$  nm). This LOS is solely utilized to measure the time resolved emission of the discharge, allowing to monitor the temporal stability of the discharge. Absolute intensities and plasma parameters are, in this case, not evaluated.

The second lateral LOS (#2) is positioned in a distance of 9 cm to the end of the discharge vessel. The light is collected and transferred to the high-resolution Acton spectrometer in the same way as in case of the axial LOS. However, its solid angle is reduced by an aperture stop to a diameter of 4 mm. Additionally, its vertical position can be varied within a distance of 10 cm by a stepper motor, allowing to scan the whole diameter of the discharge vessel. It is applied to measure lateral intensity profiles of the discharge.

The floating double probe consist of two identical tungsten wires ( $\varnothing 300 \mu\text{m}$ , length 10 mm), positioned parallel and in a distance of 5 mm to each other. The wires are connected to electrical vacuum feedthroughs via two stainless steel tubes embedded in an insulating  $\text{Al}_2\text{O}_3$  rod which also serves as probe mounting. The probe is inserted through the transition piece into the discharge chamber and can be moved parallel to the cylinder axis within a range of 15 cm. Analogously to the axial LOS of OES, it is positioned in 1 cm distance to the cylinder axis. The floating double probe provides plasma parameters at a specific position, and thus allows for space resolved measurements in axial ( $\hat{z}$ ) direction.

## 5.2 Applied diagnostics

### 5.2.1 Measurement of the RF power transfer efficiency

The applied method to evaluate the RF power transfer efficiency or analogously, the plasma equivalent resistance, relies on the measurement of the power losses  $P_{\text{loss}}$  during plasma operation due to ohmic heating. These occur both within the RF coil and the matching network as well as via induced eddy currents in the vicinity of the RF system. Due to its approach, the technique is frequently referred to as *the subtractive method* [Hop94, Hor83, GP90]. According to equation (4.2), the RF power transfer efficiency is given by

$$\eta = \frac{P_{\text{plasma}}}{P_{\text{RF}}} = \frac{P_{\text{RF}} - P_{\text{loss}}}{P_{\text{RF}}} = \frac{P_{\text{RF}} - I_{\text{ant,plasma}}^2 R_{\text{loss}}}{P_{\text{RF}}}, \quad (5.1)$$

where  $I_{\text{ant,plasma}}$  is the root mean square of the AC current running through the antenna during plasma operation. In analogy, the plasma equivalent resistance  $R_{\text{plasma}}$  can be determined via

$$R_{\text{plasma}} = \frac{P_{\text{RF}}}{I_{\text{ant,plasma}}^2} - R_{\text{loss}}. \quad (5.2)$$

The delivered RF power  $P_{\text{RF}}$  is measured by the in-line voltage and current probe. In order to quantify the power losses  $P_{\text{loss}}$ , two steps are required [Hop94]. First, the current  $I_{\text{ant,plasma}}$  during plasma operation is measured via the installed current transformer. Second, the real part of the complex resistance of the RF coil and the matching network  $R_{\text{loss}}$  has to be determined at the same conditions as during plasma operation. This is achieved by applying power to the RF system while the ignition of a discharge is suppressed, typically by reducing the working

pressure significantly below the Pa regime, while maintaining the settings of the matching network. This implies on the one hand, that the impedance matching to the output resistance of the generator is typically no longer achieved, and a considerable amount of reactive power occurs. On the other hand, all of the active RF power is now solely consumed due to ohmic losses within the coil, the matching network and due to eddy currents. If the antenna current  $I_{\text{ant,vac}}^2$  is measured simultaneously during this vacuum operation, the loss resistance can be calculated according to

$$R_{\text{loss}} = P_{\text{RF}}/I_{\text{ant,vac}}^2. \quad (5.3)$$

In practice, the RF power is varied in several steps, each time measuring the respective antenna current. By plotting  $P_{\text{RF}}$  against  $I_{\text{ant,vac}}^2$ , the antenna resistance is provided by the slope of a linear increase. Exemplarily, this is shown in figure 5.4 for an excitation frequency of 1 MHz and the application of the helical five-turn ICP coil. The observed dependence of  $P_{\text{RF}}$  on the square of the current is almost ideally linear, yielding a loss resistance of  $0.117 \Omega$ .

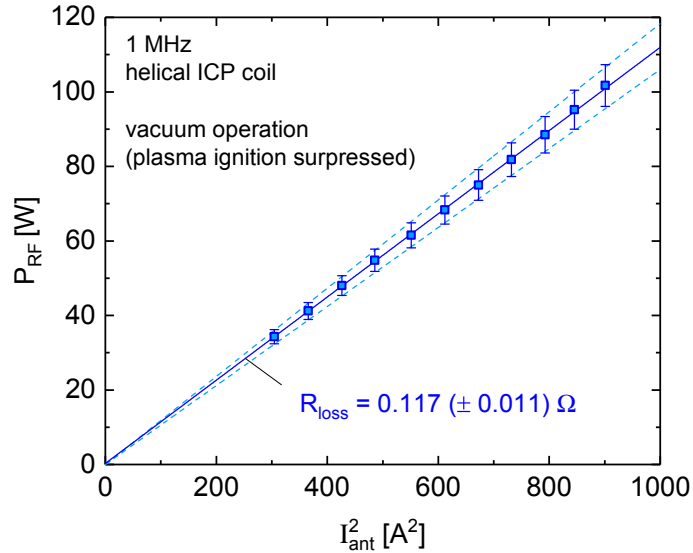


**Figure 5.4:** Example of the measurement of the resistance  $R_{\text{loss}}$  required for the evaluation of the power transfer efficiency. Indicated as dashed lines are the enveloping linear regressions accounting for the measurement uncertainty of the RF power.

### Limitations and measurement errors

In principle, the applied subtractive method tends to slightly overestimate the losses, since the plasma itself can effectively shield some of the induced eddy currents in its vicinity, which contributed to the measured value of  $R_{\text{loss}}$  without plasma ignition. Therefore, the method provides a lower estimate of the RF power transfer efficiency [Hop94]. However, in the present work this overestimation is assumed to be small. Due to the dielectric plasma vessel and a relatively large distance of about 15 cm from the antenna to the nearest conducting walls (transition plate and expansion chamber), losses due to eddy currents in the vicinity of the plasma are considered to be small in comparison to the ohmic losses within the antenna and the matching network.

In practice, also the effect of the temperature on the network resistance has to be considered. During plasma operation, the RF system is heated due to both ohmic heating as well as its proximity to the plasma and the discharge vessel. Ideally, the determination of the network resistance has to be conducted at the same temperature as during plasma operation. Therefore,  $R_{\text{loss}}$  is measured directly after the plasma operation to avoid a significant cooling of the system. In order to assure this, the measurement procedure has been fully automatized and can hence be conducted within a few seconds [Sei17]. Additionally, the order of the current running through the antenna during the measurement of  $R_{\text{loss}}$  is kept in the same region as during plasma operation to provide a comparable amount of ohmic heating. Therefore, the range within the RF power is varied is chosen appropriately.

The resulting error of the power transfer efficiency and the plasma equivalent resistance are estimated based on the typical measurement errors of the utilized devices. The relative measurement error of the antenna current is smaller than 2.5%. The relative uncertainty of the delivered power  $P_{\text{RF}}$  depends on the phase angle  $\varphi$  between the voltage and current measured by the V/I probe. During plasma operation,  $\varphi$  is close to 0 since impedance matching is typically achieved. In this case, the resulting error of  $P_{\text{RF}}$  is smaller than 5.5%. Since the phase difference during the determination of the network resistance is typically larger than zero, the uncertainty of the power measurement increases. This is shown by the error bars in figure 5.4. Consequently, the error range of the determined resistance is provided by the enveloping linear regressions indicated by the dashed lines. This error range of  $R_{\text{loss}}$  is much higher than the fit error of the linear regression, and typically dominates also the resulting errors of the RF power

transfer efficiency and the plasma equivalent resistance. Those can be estimated as follows:

$$\Delta\eta = (1 - \eta) \sqrt{(5.5\%)^2 + (2.5\%)^2 + \left(\frac{\Delta R_{\text{loss}}}{R_{\text{loss}}}\right)^2} \quad (5.4)$$

$$\Delta R_{\text{plasma}} = (R_{\text{plasma}} + R_{\text{network}}) \cdot 10.5\% + \Delta R_{\text{loss}}. \quad (5.5)$$

The resulting errors are evaluated for each measurement individually, as they depend on the value of  $\eta$  and  $R_{\text{plasma}}$ , respectively. In general, the error  $\Delta\eta$  is low at a high efficiency, and significantly increases at low efficiency. The relative error of  $R_{\text{plasma}}$  is at least 10.5% and increases depending on the values of  $R_{\text{loss}}$  and  $\Delta R_{\text{loss}}$ .

### 5.2.2 Optical emission spectroscopy (OES)

Optical emission spectroscopy provides non-invasive access to line of sight averaged plasma parameters. It relies on the measurement of the spectral intensity distribution  $I(\lambda)$  of optical transitions, consecutively allowing to determine the densities of the involved initial atomic or molecular states. The emissivity  $\epsilon_{ik}$  introduced in equation (3.23) is connected to  $I(\lambda)$  as follows:

$$\epsilon_{ik} = \frac{1}{l_{\text{plasma}}} \int_{\Delta\lambda_{ik}} I(\lambda) f(\lambda) d\lambda. \quad (5.6)$$

In equation (5.6),  $l_{\text{plasma}}$  denotes the length of the line of sight within the plasma and  $f(\lambda)$  is the calibration factor of the spectroscopic system, which takes into account its wavelength dependent sensitivity.

#### OES at atomic hydrogen

In the present work, the line emission  $\epsilon_{\text{H}}(n_i \rightarrow n_k = 2)$  of the first four transition lines of the atomic Balmer series of hydrogen and deuterium is measured and the corresponding emissivities are evaluated according to equation (5.6). Those serve as input for the collisional radiative models applied to evaluate the plasma parameters. The designation, principal quantum number of the upper and lower states and the corresponding central wavelengths of the first four Balmer lines of hydrogen and deuterium are summarized in table 5.1.

## OES at molecular hydrogen

Due to the multitude of different electronic, vibrational and rotational states of the hydrogen molecule, a variety of optical transitions occurs. The spectroscopically well accessible Fulcher- $\alpha$  system ( $d^3\Pi_u, \nu', J' \rightarrow a^3\Sigma_g^+, \nu'', J''$ ), located in the wavelength region between 590 nm and 650 nm is diagnostically treated after [FH98, BRF17] for both hydrogen and deuterium. This evaluation allows to determine rotational and vibrational temperatures of the electronic ground state  $X^1\Sigma_g^+$ , as its ro-vibrational population is linked to the upper triplet state of the Fulcher system via electron impact excitation, assuming the validity of the Franck-Condon principle [Her50]. Subsequently, the total emission of the Fulcher- $\alpha$  transition is determined, which is required as input for the collisional radiative modelling. In the present work, the first twelve emission lines of the rotational Q-branch ( $J' = J''$ ) of the first four diagonal vibrational bands ( $\nu' = 0, \dots, 3 \rightarrow \nu'' = \nu'$ ) from its spectrum are evaluated.

In the present work, the **gas temperature**  $T_{\text{gas}}$  is specifically required to determine the neutral particle density  $n_0 = n_{\text{H}} + n_{\text{H}_2}$  during plasma operation via the ideal gas law. For the latter, also the absolute pressure is required, which is measured by the capacitive pressure gauge. During plasma operation at lower pressure, thermal transpiration effects occurring between the discharge tube and the pressure gauge are considered according to an empirical approach by [TS63]. Diagnostic access to the gas temperature is provided by the evaluation of the rotational population of the upper Fulcher state. In hydrogen and deuterium, the energy difference between the rotational levels of a vibrational level in the electronic ground state X is small (of the order of 0.01 eV), which allows for a population by heavy particle collisions and a subsequent thermalization. Consequently, the population distribution of the rotational states can be described by the energy

**Table 5.1:** *Transition lines of the Balmer series of atomic hydrogen and deuterium with the principal quantum numbers  $n$  for the upper and the lower state and the corresponding wavelengths  $\lambda$  [GMS95].*

$n_i$	$n_k$	Hydrogen		Deuterium	
		designation	$\lambda$ [nm]	designation	$\lambda$ [nm]
3	2	H $_{\alpha}$	656.3	D $_{\alpha}$	656.1
4	2	H $_{\beta}$	486.1	D $_{\beta}$	486.0
5	2	H $_{\gamma}$	434.0	D $_{\gamma}$	433.9
6	2	H $_{\delta}$	410.2	D $_{\delta}$	410.1

distribution of the heavy particles ( $\rightarrow T_{\text{gas}}$ )[OOR<sup>+</sup>89]. Assuming that for electron impact excitation the rotational quantum number is not changed, the rotational distribution in the ground state is projected into the excited upper Fulcher state. In order to evaluate the rotational distribution in the upper Fulcher state, the corresponding emissivities of the ro-vibronic transitions are determined according to equation (5.6). Those are characterized furthermore by the proportionality [Her50]

$$\epsilon_{\text{d,a}}^{\nu',\nu'',J',J''} \propto gS_{J',J''} \exp\left(-\frac{\Delta E_{\text{rot}}(J')}{k_{\text{B}}T_{\text{rot}}^{\text{d}\nu'}}\right), \quad (5.7)$$

where  $g$  denotes the degeneracy due to the nuclear spin and  $S_{J',J''}$  the *Hönl-London factor* [Her50, Kov69].  $\Delta E_{\text{rot}}(J')$  is the energy difference between the rotational levels and the lowest level  $J' = 1$ .  $T_{\text{rot}}^{\text{d}\nu'}$  is the rotational temperature of a thermal distribution in the vibrational state  $\nu'$  and is determined by the slope of  $\ln(\epsilon_{\text{d,a}}^{\nu',\nu'',J',J''}/gS_{J',J''})$  plotted against  $\Delta E_{\text{rot}}(J')$ . Considering the corresponding rotational constants  $B_{\nu'=0}^{\text{X}}$  and  $B_{\nu'}^{\text{d}}$ , the rotational temperature in the ground state X is obtained via [OOR<sup>+</sup>89]

$$T_{\text{rot}}^{\text{X}\nu=0} = \frac{B_{\nu=0}^{\text{X}}}{B_{\nu'}^{\text{d}}} T_{\text{rot}}^{\text{d}\nu'}. \quad (5.8)$$

If the rotational states in the electronic ground state thermalize with the heavy particles, the value of  $T_{\text{rot}}^{\text{X}\nu=0}$  is assumed to be equal to the gas temperature. In the present case, this is valid only for the lowest five rotational levels up to  $J' = 5$ , as the rotational population in the investigated discharges typically exhibits a strong two-temperature Boltzmann distribution where the population of the higher rotational states is characterized by a much higher temperature than the gas temperature. Further details regarding this phenomenon and remarks regarding its origin can be found within [BRF17]. Accordingly, the gas temperature in this work is evaluated from the rotational temperature of the lower states, and taken from the mean value of the first three evaluated vibrational transitions  $\nu' = 0, 1, 2$  which are typically in good agreement among themselves [BRF17].

In order to determine the **entire emission of the Fulcher transition**, an approach described in detail by [FH98] is followed. In addition to the evaluation of the rotational population discussed above, it requires the determination of the vibrational population in the electronic ground state. In order to deduce the latter, at first the vibrational population of the upper Fulcher state is evaluated via the

first four diagonal vibrational transitions using equation (5.7), while taking into account the deduced rotational populations. The measured population is then compared to calculated populations, determined by assuming different vibrational (Boltzmann) distributions in the ground state, characterized by vibrational temperatures  $T_{\text{vib}}$ . These distributions are projected into the upper Fulcher state, accounting for the corresponding Franck-Condon factors and vibrationally resolved rate coefficients [FW06]. The vibrational population in the ground state and thus, the vibrational temperature, is then provided by the best match between the measured and the calculated distributions.

Subsequently, the measured emission of the first four diagonal transitions is extrapolated to deduce the total Fulcher emission  $\epsilon_{\text{Ful}}$ . The scaling required for this extrapolation depends on  $T_{\text{vib}}$  and is derived from the ratio of a calculated emissivity of the first four vibrational bands to the calculated emissivity of the entire Fulcher transition. Such a calculation is performed via a corona model, which balances the population via electron impact excitation from the electronic ground state against the depopulation via spontaneous emission. The corona model applied for the calculation is described in detail in [WF16] and relies on cross section data provided by [MTG72].

### Determination of plasma parameters via collisional radiative modelling

The measured emissivities of the atomic Balmer lines and the molecular Fulcher transition are used to determine line of sight averaged values of the electron temperature, the electron density and the density ratio of atomic to molecular hydrogen via collisional radiative models (CR models). In the present work, the evaluations were performed by the simultaneous application of the CR models *Yacora H* for the hydrogen atom and *Yacora H<sub>2</sub>* for the hydrogen molecule. A detailed description of the models is provided by [WF16]. These models are only available for hydrogen, and not for deuterium. The applicability to deuterium is separately discussed in a paragraph following below.

In general, the applied CR models balance all relevant population and depopulation processes for the particular states of interest of H and H<sub>2</sub> by calculating so-called population coefficients  $R_{si}$ . Via these coefficients, the density  $n_i$  of an excited state  $i$  is linked to the electron density and the density  $n_s$  of a particular species  $s$ . A 0-dimensional approximation of the population density  $n_i$  in equilibrium is thus determined by [WF16]

$$n_i = n_e \sum_s n_s R_{si}(T_e, n_e, \dots). \quad (5.9)$$

In case of the hydrogen atom, the applied model comprises the population densities of the principal electronic states with  $n = 1, \dots, 40$ . For the hydrogen molecule, a CR model including all states of the singlet and triplet systems up to the principal quantum number  $p = 10$  is used, which considers the splitting due to angular momentum of the electrons for the electronically excited states with  $p \leq 3$  [WF16]. Via non-vibrationally resolved cross sections for electron collision excitation from the ground state to the excited states taken from [MTG72], this model is in the present case utilized to provide the population density of the upper Fulcher state  $d^3\Pi_u$ . For the electron excitation process, the CR models assume a Maxwellian EEDF. In order to facilitate the evaluation, the plasma is treated as optically thin by these models, which means that processes including the reabsorption of photons are not considered. This is a valid assumption for the molecules, but has to be considered as an approximation for the atoms, since the reabsorption of photons corresponding to the Lyman series can be of relevance.

In order to derive a specific set of population densities, the applied models require a set of input parameters, namely the densities and temperatures of the neutrals H and H<sub>2</sub> and those of the electrons and the charged particles H<sup>+</sup>, H<sub>2</sub><sup>+</sup>, H<sub>3</sub><sup>+</sup> and H<sup>-</sup>. Based on the population densities provided by the models and emission rate coefficients of the considered transitions, corresponding emissivities are calculated according to equation (3.23). The required transition probabilities are provided by [FW06] for the Fulcher- $\alpha$  transition and by [KRR18] for the atomic Balmer lines. In practice, the models are used to determine the plasma parameters via a backward calculation: their input parameters are varied until both the absolute emissivities and the relative line ratios are matched to the values obtained from the OES measurements.

In the present case, specific assumptions can be made which simplify this procedure. The OES measurements along the axial LOS (see figure 5.3) of the experiment are performed in order to cover the central, plasma generating regime of the discharges previously introduced as an *ionizing* plasma. In fully ionizing hydrogen plasmas, the amount of relevant reaction channels is strongly reduced: only direct excitation from the electronic ground states of H and H<sub>2</sub> and dissociative excitation of H<sub>2</sub> have to be taken into account [WF16]. Processes involving the hydrogen ions do not play a significant role. On the one hand, this implies that the models are not sensitive to the densities of H<sup>+</sup>, H<sub>2</sub><sup>+</sup>, H<sub>3</sub><sup>+</sup> and H<sup>-</sup>. In consequence,

these parameters cannot be determined based on the OES measurements in this case. On the other hand, the possibility to neglect these species strongly reduces the amount of free input parameters of the models, namely to the densities of H and H<sub>2</sub> and the electron density and temperature. Additionally, the total neutral density  $n_0 = n_{\text{H}} + n_{\text{H}_2}$  is given by the ideal gas law, assuming  $T_{\text{H}} = T_{\text{H}_2} = T_{\text{gas}}$  and taking into account the measured absolute pressure. The remaining free parameters  $n_{\text{e}}$ ,  $T_{\text{e}}$  and  $n_{\text{H}}/n_{\text{H}_2}$  are now determined by an iterative variation, until the calculated emissivities of the Balmer lines  $\epsilon_{\text{H}_{\alpha-\delta}}$  and the Fulcher emission  $\epsilon_{\text{Ful}}$  as well as the line ratios  $\epsilon_{\text{H}_{\alpha}}/\epsilon_{\text{H}_{\beta}}$ ,  $\epsilon_{\text{H}_{\beta}}/\epsilon_{\text{H}_{\gamma}}$ ,  $\epsilon_{\text{H}_{\gamma}}/\epsilon_{\text{H}_{\delta}}$  and  $\epsilon_{\text{H}_{\gamma}}/\epsilon_{\text{Ful}}$  are matched with the corresponding measured values within a typical error of the emissivity measured via OES of  $\pm 10\%$ .

### Application of CR models to D<sub>2</sub> plasmas

The applied CR models *Yacora H* and *Yacora H<sub>2</sub>* are in general designed for the hydrogen atom and molecule, whereas no specific models for deuterium are available. However, the application of the CR models for H and H<sub>2</sub> to deuterium discharges is well possible, if the influence of significant isotopic effects is thoroughly considered.

First, the small variations of the atomic energy levels, which lead to the slight wavelength shifts of the Balmer emission lines (see table 5.1), are expected to have no significant influence on the electron excitation process of the atoms. Additionally, the corresponding emission rate coefficients are virtually equal as well [KRR18]. Consequently, all processes coupled to the atomic states are assumed to be directly transferable to deuterium.

In contrast, isotopic effects are expected for processes depending strongly on the vibrational and rotational states of the molecules and molecular ions, as they are influenced by the nuclear mass. This applies foremost to processes leading to the dissociation of molecules, as discussed in chapter 3.3. Regarding the atomic CR model, this implies in the present case that only the dissociative excitation of molecules has to be considered, since all processes coupled to the ions are neglected due to the ionizing nature of the discharge. Cross sections for the excitation of the Balmer series via dissociative excitation for hydrogen and deuterium molecules are given by [MHL77]. They show systematically lower cross sections for deuterium over the entire electron energy range, typically between 20 and 50%. Consequently, the rate of dissociative excitation is generally overestimated if *Yacora H* is applied to deuterium.

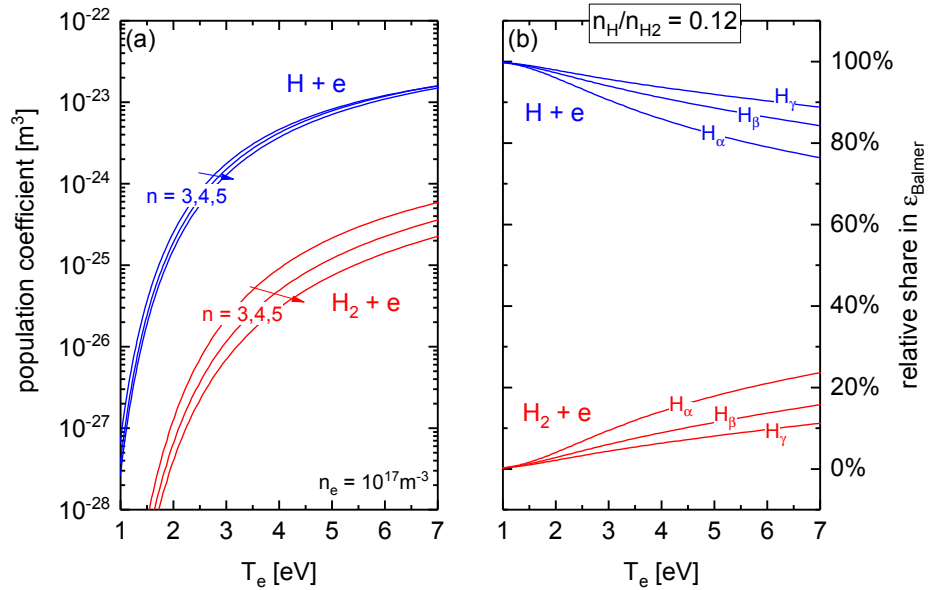


**Figure 5.5:** (a) Population coefficients for the states  $n = 3, 4, 5$  of atomic hydrogen calculated with the CR model Yacora H[WF16] for  $n_e = 1 \times 10^{17} \text{m}^{-3}$ . (b) Corresponding relative contribution of the excitation channels coupled to the atomic and the molecular ground state to the emissivities of the atomic Balmer series.

In the present case however, this overestimation is small: Due to the relatively high atomic densities of the investigated discharges, the globally dominant population channel of the upper states of the Balmer transitions is the electron impact excitation of atoms. This circumstance is demonstrated via figure 5.5. In part (a), the population coefficients calculated via the CR model of the upper Balmer states  $n = 3, 4, 5$  due to electron impact excitation of atoms and due to the dissociative excitation of molecules are compared at varying electron temperature and an exemplary electron density of  $10^{17} \text{m}^{-3}$ . The population coefficients coupled to the atomic ground state are systematically about two orders of magnitude higher. In order to quantitatively assess the influence of this difference at the present discharge parameters, the resulting share of both excitation channels in the corresponding emissivities of the Balmer lines is shown in part (b) for an atomic to molecular density ratio of 0.12. In this specific case, the contribution coupled to the molecules is found to be within the range of a few percent up to 20%, increasing for higher  $T_e$  and lower principle quantum number of the excited state. However, this case represents the upper limit of the influence of the dissociative excitation channel within the present work, since  $n_{\text{H}}/n_{\text{H}_2} = 0.12$  is the globally

lowest measured value of the density ratio. Typically,  $n_{\text{H}}/n_{\text{H}_2}$  reaches values much higher than assumed here, and particularly at higher electron temperature and in deuterium (due to its higher dissociation cross section). This reduces the contribution of the excitation channels coupled to the molecular ground state even further, typically to a relative share of 10% or less in the total emission. Consequently, the expected isotopic differences of the dissociative electron impact excitation of  $\text{H}_2$  and  $\text{D}_2$  in the range of a few ten percent are influencing a process which contributes only by a few percent to the total emission. Therefore it can be concluded that these isotopic differences only have a minor influence at the present parameters, and the applicability of the atomic CR model for deuterium discharges is considered to be well provided.

For assessing the application of *Yacora H<sub>2</sub>* to deuterium, similar arguments as for the atomic model can be stated: the CR model applied to determine the population density of the upper Fulcher state does only resolve the electronic, but not the vibrational and rotational states of the molecules. On the one hand, this simplification imposes the general restriction that influences of the vibrational distributions within participating molecular states on excitation processes cannot be displayed by the model. On the other hand, this limitation entails that also the molecular CR model can be applied to deuterium due to the same electronic states of  $\text{H}_2$  and  $\text{D}_2$  in a first approximation. This correspondence is also illustrated by [FW06] based on the specific example of the Fulcher- $\alpha$  transition. As shown therein, the effective radiative lifetimes and transition probabilities of electronic molecular states are independent on the mass of the isotope. However, the effective excitation cross sections required by the CR model may still exhibit isotopic differences between deuterium and hydrogen due to an implicit ro-vibrational influence in principle. These effects could only be truly resolved by a ro-vibrationally resolved CR model for both isotopes, which is not available yet due to the lack of resilient data regarding the excitation cross sections of the deuterium molecule. Therefore, the non-vibrationally resolved model for hydrogen is applied as a first approximation also for deuterium.

### Limitations and measurement errors

The main limitation of optical emission spectroscopy is that only line of sight averaged plasma parameters are accessible. It is therefore impossible to resolve spatial variations of the plasma's distribution along one considered LOS. If it is required to distinguish between changes of the global values of the plasma

parameters and their spatial profiles, additional measures capable of measuring locally and thus, spatially resolved are required - such as the floating double probe discussed in the following section.

The characteristic error of the emissivity measured via OES of the order of 10% accounts for both the uncertainty of the measurement itself and the intensity calibration. Since the plasma parameters evaluated via the CR models are varied to match the measured values of OES, this error also defines a region of uncertainty for  $n_e$ ,  $T_e$  and  $n_H/n_{H_2}$  within those can be changed and still allow for a good agreement between model and measurement. In the present case, the typical values of the relative errors are 25% for  $n_e$  and 15% for  $T_e$  and  $n_H/n_{H_2}$  each.

### 5.2.3 Floating double probe

The application of traditional Langmuir probes [MSL26] for the determination of local plasma parameters requires an electrode well connected to the plasma, which can serve as the reference point for the potential when a DC bias voltage is applied to the probe. In RF discharges, this role can be fulfilled by partially metallic vessel walls or other metallic components in the direct vicinity of the discharge. In the present case however, discharges are created and investigated in a dielectric tube where no reference electrode in sufficiently good contact to the plasma is available. Therefore, the double-probe method, originally proposed by [JM50], is applied. It provides the possibility to conduct probe measurements without the requirement of a potential reference. By means of this technique, the local electron temperature and density of the discharge can be obtained. The following descriptions are based on a detailed characterization provided by [CEZ65].

The principle scheme of a double probe is illustrated in figure 5.6. The system consists of two probes which are insulated from ground and biased with respect to each other by a voltage  $U$ . Consequently, the entire system "floats" with the plasma, hence being called a *floating double probe*. In general, the system is always on a negative potential with respect to the plasma in order to prevent the inflow of a net current. In the present case, the probes are cylindrical and consist of tungsten wires, as presented in section 5.2. The probes 1 and 2 are manufactured to be identical and have a surface area of  $A = A_1 = A_2$ . Both probes are located in the plasma, which is assumed to have constant properties within the spacing of the probes.

By a variation of the bias voltage and the simultaneous measurement of the

current  $I$  between the probes, the current-voltage characteristic of the floating double probe is obtained. Exemplary, a probe characteristic obtained with the system applied in this work is shown in figure 5.7. If no voltage is applied, the entire system is on floating potential. Consequently, an equal flow of electrons and ions from the plasma onto both probes is established and the resulting current  $I$  is zero due to the identical probe surfaces. If  $U$  is made slightly positive, the potential at probe 1 will increase and analogously the potential at probe 2 will decrease. Consequently the flow of electrons on probe 1 is increased while it is decreased at probe 2, resulting in a positive current  $I$  from 2 to 1. If the bias voltage is increased further, the potential at probe 2 is reduced accordingly until eventually, all electrons are repelled. In this case, the *ion saturation regime* is reached with probe 2 solely drawing the *ion saturation current* carried by the plasma ions, which is compensated by an increasing electron current on probe 1. Regarding the  $I$ - $U$  characteristic, reaching the ion saturation regime is accompanied by a significant reduction of the slope of the measured current  $I(U)$ . Changing the sign of the applied voltage leads to same general behaviour with a reversed measured current and consequently to the symmetry of the probe characteristic illustrated in figure 5.7.

In order to deduce the plasma parameters of interest from the double probe characteristics, a quantitative description of  $I(U)$  considering the individual ion and electron currents onto both probes at varying bias voltage is required. Such an analysis is provided in detail by [CEZ65]. Assuming a Maxwellian electron energy distribution, it yields a proportionality for the slope of  $I(U)$  at  $U = 0$ :

$$\frac{dI}{dU} \Big|_{U=0} = \frac{e}{k_B T_e} \frac{|I_{\text{sat},1} I_{\text{sat},2}|}{|I_{\text{sat},1}| + |I_{\text{sat},2}|}. \quad (5.10)$$

By measuring the slope of the characteristic at the origin as indicated in figure

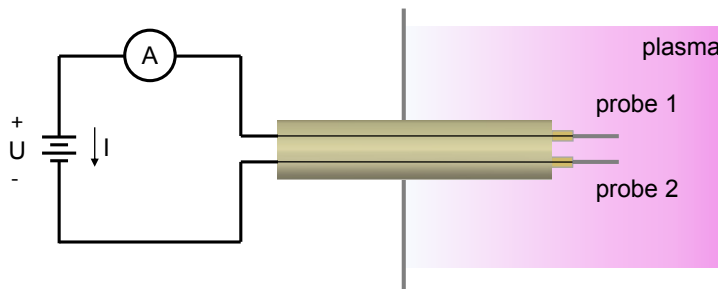


**Figure 5.6:** Schematic of the floating double probe system.

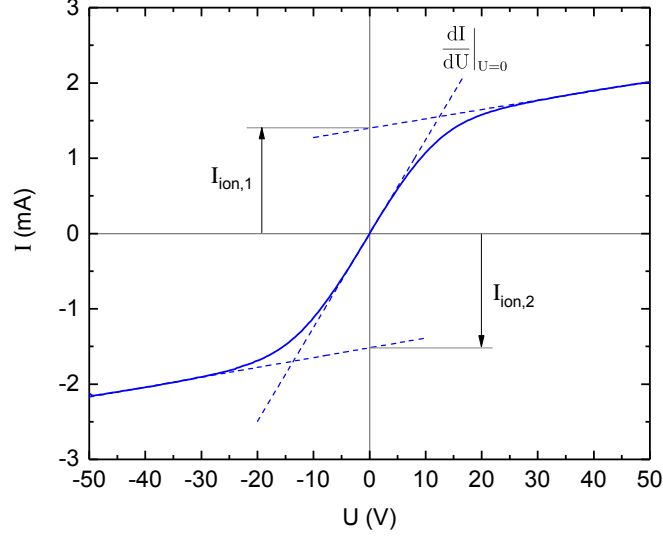


**Figure 5.7:** Exemplary  $I/U$  characteristic of the floating double probe obtained with the applied diagnostic setup.

5.7, the electron temperature can be deduced depending on the values of the ion saturation currents  $I_{\text{sat},1}$  and  $I_{\text{sat},2}$ . Under the basic assumption that the potential of the probes is always negative enough to essentially draw the ion saturation current,  $I_{\text{sat},1}$  and  $I_{\text{sat},2}$  can be determined at  $U = 0$  (and generally at any other voltage) by a smooth extrapolation, as illustrated in figure 5.7.

Based on the measured ion saturation currents and equation (5.10), the plasma density can be determined subsequently. Assuming a radial, collision free ion flux on the probe area  $A$  independent of the probe voltage  $U$ , the saturation ion current is approximated by [CEZ65]

$$I_{\text{sat}} = \frac{1}{2} n_e A \left( \frac{k_B T_e}{m_{\text{ion}}} \right)^{1/2}. \quad (5.11)$$

The value of  $I_{\text{sat}}$  is given by the average of the currents  $|I_{\text{sat},1}|$  and  $|I_{\text{sat},2}|$ . In the specific case of hydrogen and deuterium plasmas, the ion mass  $m_{\text{ion}}$  denotes an effective ion mass due to the presence of different ion species, namely  $\text{H}^+$ ,  $\text{H}_2^+$  and  $\text{H}_3^+$ . In the present case, the actual ion contribution in the plasma is not directly measurable. However, investigations via energy resolved mass spectrometry at a different low pressure RF discharge operating at well comparable parameters showed, that the effective mass in the pressure and power range of interest is typically in the region between 2 u and 3 u [Bri17]. For the present case, a value of

$m_{\text{ion}} = 2.5 \text{ u}$  for hydrogen and  $m_{\text{ion}} = 5 \text{ u}$  for deuterium was chosen, accordingly. The uncertainty of this assumption is considered within the typical error range of the density described in the following section.

### Limitations and measurement error

The ability to obtain spatially resolved plasma parameters is accompanied by the drawback that the floating double probe is, analogously to every other probe system, an invasive diagnostic. It can disturb the plasma, on the one hand due to its physical presence and on the other hand due to its potential difference with respect to the plasma. A priori, the extend of its influence on the plasma parameters is difficult to assess. Therefore it is favourable to compare the parameters obtained via probe measurements with non-invasive diagnostics, in this case OES.

Regarding the determination of the electron temperature, some considerations have to be made. As already described, the potential of the floating probe system is generally negative in comparison to the plasma, i.e. repelling for the plasma electrons, and any electron current drawn on one probe must always be balanced by an equal ion current on the other. As the total current to the system is furthermore always limited by the ion saturation current, only fast electrons in the high energy tail of the EEDF can ever be collected. Consequently, only those electrons contribute to the measured value of  $T_e$  while the bulk of the EEDF is not sampled [CEZ65]. Additionally, in RF discharges the probe characteristics can be distorted by RF fields and occurring oscillations of the plasma potential, which specifically influence the plasma electrons due to their higher mobility compared to the plasma ions. Consequently, the evaluation of the electron temperature by the slope of the double probe can be affected. In order to counteract such distortions, compensation techniques for the measured probe currents, e.g. via band pass filters, are required. However, such countermeasures are always designed to be applied at a specific frequency. Since in the present work different excitation frequencies are used and no frequency dependent compensation is applied to facilitate the measurement, RF distortions influencing the determination of  $T_e$  cannot be ruled out. Consequently, the electron temperature obtained by the floating double probe method is not quantitatively used to characterize the discharges investigated in this work.

The ion currents on the other hand are considered to be undisturbed by RF distortions and allow for the evaluation of the plasma density according to equation

(5.11). The resulting error of the local  $n_e$  obtained is given by the uncertainties of each considered parameter, typically leading to a relative error of 25%. The floating double probe is used to obtain spatial profiles of the plasma density parallel to the discharge cylinder axis, as it was shown in figure 5.3. The spatial accuracy  $\Delta z$  of this measurement is provided by the finite probe length, as the plasma is sampled in its whole reach. Accordingly, the position  $z$  of the measurement is assumed to be at the center of the probe wires of 10 mm length each, with an uncertainty of  $\Delta z = \pm 5$  mm.

### Effects of a low external magnetic field

In the presence of a magnetic field, the probe characteristics can be generally altered since the diffusion of charged particles is hindered, as discussed in section 3.5. However, the effects of the magnetic field can be neglected if the ratio  $r_p/r_c$  between the probe radius  $r_p$  and the gyration radius  $r_c$  is small [PT01]. In the present case, the ion saturation current carried by the positive hydrogen ions has to be considered. As specifically shown in chapter 3.5, the gyration radii of the different hydrogen and deuterium ions range from several mm up to a few cm at the present magnetic fields. Since this is significantly larger than the probe radius of 150  $\mu\text{m}$ , the influence of the magnetic field on the measured ion saturation current is negligible in the whole  $B$ -field range of interest.



## 6 Experimental approach and boundary conditions

In the present work, basically four different setups are investigated: inductive discharges generated via the helical coil at excitation frequencies of 1, 2 and 4 MHz and discharges applying the Nagoya-type antenna at 4 MHz. The general procedure of igniting and operating the discharges in order to obtain reliable and reproducible results is presented in the following, including some remarks regarding the experimental restrictions and boundary conditions to be considered. Apart from the excitation frequency, also the gas pressure, the delivered RF power and the static magnetic field can be varied externally during operation. Together, those are referred to as the *operational parameters* of the discharges within this work.

### 6.1 Impedance matching and discharge ignition

Depending on the applied antenna and the specific excitation frequency, different matching circuits have been set up to meet the requirement introduced in equation (4.1) that the load impedance has to equal a value of  $Z_0 = 50 \Omega$ . For all setups considered in this work, impedance matching can be achieved by applying a circuit of the same basic topology (frequently referred to as a  $\gamma$ -type matching network). In order to quantify its specifically required components, a simplified network analysis has been conducted. Therefore, the equivalent circuit of the applied network is depicted in figure 6.1.

The antenna of the inductivity  $L_{\text{ant}}$  and resistance  $R_{\text{ant}}$  and the plasma with its equivalent plasma resistance  $R_{\text{plasma}}$  are regarded as a series circuit with respect to each other and are connected to the in- and output of the generator. The actual matching network consist of two capacitors  $C_1$  and  $C_2$  (assumed to be ideal in this case, i.e.  $R = 0$ ), connected in series and parallel to the plasma and the antenna, respectively. In this simplified picture, resistive contributions of the

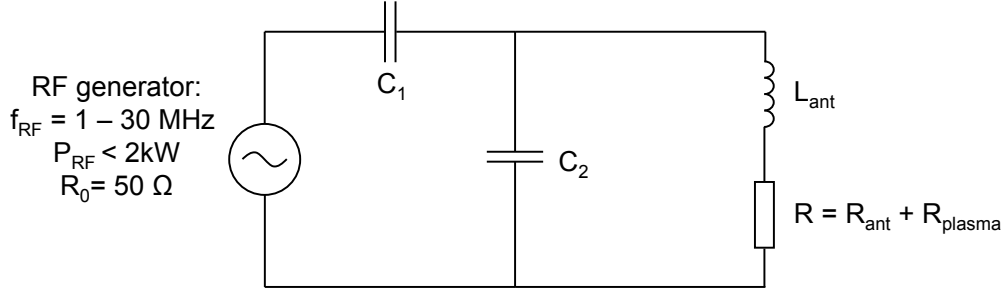


**Figure 6.1:** Simplified equivalent circuit of the matching network utilized at CHARLIE.

transmission lines and connections as well as reactive contributions of the plasma are not considered. Therefore, also the antenna resistance  $R_{\text{ant}}$  is not equal to the integral loss resistance  $R_{\text{loss}}$  introduced in chapter 4.1, as the measurement of the latter specifically includes also those resistive contributions which are neglected in the scheme of figure 6.1. In order to fulfill the matching equality of equation (4.1), the capacitances  $C_1$  and  $C_2$  are adjusted. In practice, a combination of fixed and variable vacuum capacitors (Comet CVBA-1400AC/4-BEA-L, adjustable in the range of 0.008 – 1.4 nF) is utilized: the fixed capacitors are used to achieve the required capacitance roughly in a first step. The variable capacitors are utilized as  $C_1$  and  $C_2$  have to be adjustable in real time: on the one hand, they have to cover the range imposed by the generally variable contribution  $R_{\text{plasma}}$  of the plasma depending on the operational parameters of the discharge. On the other hand, a certain power output even in gas or vacuum operation and without the contribution of  $R_{\text{plasma}}$  is mandatory, in order to achieve a power output sufficient for a discharge ignition in the first place.

The required values for the capacitors can be calculated considering the principles of conservation of electric charge and of conservation of energy via an application of *Kirchhoff's circuit laws*. Applying the matching conditions  $\text{Re}(Z_{\text{load}}) = 50 \ \Omega$  and  $\text{Im}(Z_{\text{load}}) = 0$  as boundary conditions, this yields

$$C_1 = \frac{1}{\omega_{\text{RF}}} \sqrt{\frac{R}{R_0}} \left( \omega_{\text{RF}}^2 L_{\text{ant}}^2 + R^2 - RR_0 \right)^{-1/2} \quad (6.1)$$

and

$$C_2 = \frac{L - C_1(\omega_{\text{RF}}^2 L^2 + R^2 - RR_0)}{\omega_{\text{RF}}^2 L^2 + R^2}. \quad (6.2)$$

The subsequent estimation of the capacitances requires several input parameters, which are provided in table 6.1 for the four different RF setups investigated in the present work. The inductances of the different antennas are measured via an RLC-multimeter while being disassembled from the circuit, whereas the provided uncertainties account for the unknown contributions of the RF connections and the transmission lines when the RF circuit is fully assembled at the experiment. The estimation of the resistances can be roughly done by a direct measurement regarding  $R_{\text{ant}}$ , but especially for  $R_{\text{plasma}}$  it largely relies on previous experimental observations and experience. The provided values in table 6.1 are the typical values found for the discharges investigated in the present work. The resulting capacitances show that only in case of the inductive coil and 4 MHz the adjustable capacitors achieve the matching requirement on their own. For lower frequencies and the Nagoya antenna, additional fixed capacitors have to be connected in parallel to shift the ranges of  $C_1$  and  $C_2$  to higher values. Applying these matching circuits, impedance matching is achieved for all four setups within the required range of pressure, RF power and external magnetic field for an operation of discharges in deuterium and hydrogen.

### Plasma ignition

In general, the practical procedure to ignite discharges is similar for all applied RF setups. Typically, the gas pressure in hydrogen or deuterium is set to the range between 3 and 5 Pa and the network is adjusted to deliver the RF powers necessary to reach a capacitive, and subsequently an inductive discharge. For an operation with the helical ICP coil, the typically required power for an inductive ignition is in the range between 250 and 500 W, increasing with decreasing excitation frequency. This frequency dependence is due to the voltage drop across the antenna, which is approximately proportional to  $\omega_{\text{RF}}L_{\text{ant}}$ . If the voltage drop is higher, a capacitive discharge providing sufficient ionization to reach the H-mode is ignited easier. Applying the Nagoya antenna, analogously a higher RF power of the order of

**Table 6.1:** *Parameters of the matching network for different applied antennas and excitation frequencies.*

Antenna	$f_{\text{RF}}$ [MHz]	$L_{\text{ant}}$ [ $\mu\text{H}$ ]	$R_{\text{ant}}$ [ $\Omega$ ]	$R_{\text{plasma}}$ [ $\Omega$ ]	$C_1$ [nF]	$C_2$ [nF]
ICP	1	$2.4 \pm 0.2$	$\approx 0.1$	0.1 - 0.9	0.4 - 1.8	8.0 - 9.4
ICP	2	$2.4 \pm 0.2$	$\approx 0.15$	0.5 - 2.0	0 - 1.4	1.6 - 3.0
ICP	4	$2.4 \pm 0.2$	$\approx 0.2$	1.0 - 6.0	0 - 1.4	0 - 1.4
Nagoya	4	$0.7 \pm 0.2$	$\approx 0.12$	0.02 - 0.5	0 - 1.4	1.0 - 2.4

1 kW is required for the ignition, due to the significantly lower inductance of the antenna compared to the helical coil. Its low inductance is also the reason why in this case no discharges at frequencies below 4 MHz are possible, as the RF power required at lower frequency exceeds the maximum of 2 kW provided by the generator. Even though it is not within the scope of this work, in principle the applied RF setup allows also for the generation of discharges at higher frequency than 4 MHz with both antennas. Once a stable inductive discharge is ignited, the pressure and the delivered RF power are adjusted (via both the matching network and the generator) to match the individually desired values. In case of discharges applying the Nagoya antenna, this also implies the adjustment of the external magnetic field, and the subsequent transition of the discharge to a wave-assisted heating mode.

## 6.2 Discharge operation, temporal stability and reproducibility

The discharges generated in the present work are run in continuous wave operation, i.e. the plasma reaches steady state, ideally regarding all processes defining and influencing its parameters. If the steady state at specific operational parameters like pressure and power is reached, measurements are conducted which provide results that are reproducible within the typical errors of the applied diagnostics. In practice, the time to reach steady state is typically of the order of several minutes up to an hour. Within this time scale, mainly two contributions can be distinguished - even though being partly coupled - which define the temporal behaviour of the discharge:

The first determining factor is thermal, i.e. the heating of the experiment vessel, the RF system and all components of the setup during operation. As already discussed, on the one hand the temperature influences the ohmic resistance of the RF components and thus influences the plasma parameters by changing the RF power transfer efficiency. On the other hand, the temperature of the discharge vessel can change the dynamics of plasma-surface interactions, e.g. by changing the wall recombination coefficient  $\gamma$  discussed in section 3.3.

This correlation directly leads to the second mechanism which empirically dominates the long term stability of the discharges: the recombination processes of atomic hydrogen to molecules at the walls. However, this occurs not only due to the temperature dependence of the recombination coefficient. As already

discussed in section 3.3, the recombination processes are strongly dependent on the coverage of the surfaces with atomic hydrogen, which in turn exhibits a variety of dependences on the plasma and surface parameters as well. The build up of a stable coverage requires the balance of all these processes. Particularly for discharge vessels dominantly consisting of dielectric material like quartz, this leads to the typical observation that also the atomic density in low pressure low temperature hydrogen plasmas can vary within the order of several minutes or more until a stable equilibrium is reached, which is not necessarily coupled to the thermal dynamics of the experiment.

Consequently, the temporal stability of the presented discharges is monitored by the continuous measurement of two parameters: the antenna current as a measure for the thermal stability of the RF system and the emissivity of the atomic Balmer lines (LOS #1, see figure 5.3), as it is proportional to the atomic density within the discharge. If both parameters reach a stable value within the typical errors of the diagnostic systems simultaneously, the discharge is considered to have reached steady state which allows to perform systematic measurements.

### **Operational limits**

Basically, the same factors which determine the temporal stability of the discharges are also responsible for the main practical limitations of experimental operation. First, the ohmic heating of the RF system has to be sufficiently low to be compensated by the applied cooling via fans and ambient air in order to protect the components of the RF system from permanent damage. To assure that the temperature increase via joule heating is within a tolerable regime, the level of RF power, i.e. the current running through the antenna, has to be limited. Empirically, the region where the power losses  $P_{\text{loss}}$  reach values of about 300 - 400 W has been identified as a critical threshold to avoid excessive heating and damage to critical parts, e.g. connections and plugs. Below this region, the cooling capabilities of the RF system are sufficient to allow for continuous discharge operation, which typically applies for all discharges utilizing the helical coil for inductive plasma generation in the present work. For an application of the Nagoya antenna however, generally higher absolute RF powers are required during operation and the power losses due to ohmic heating can indeed exceed this threshold. The second limiting factor is the requirement to prevent a permanent modification or damaging of the discharge vessel caused by a high plasma admission. Inevitably, the plasma always interacts with the vessel, which generally leads to a temperature increase of its

walls, but can eventually also result in a the modification of the surface properties and the emission of substantial amounts of particles from the surface, e.g. due to physical sputtering and/or chemical erosion. In the present case of a quartz vessel, the latter are mainly silicon and oxygen which can be identified via their characteristic emission. On the one hand, the presence of considerable amounts of these impurities in the bulk plasma can significantly affect its properties. On the other hand, the correlated modification of the surfaces may strongly influence the surface catalytic recombination processes of atoms, and thus the atomic density within the bulk plasma. Both effects render meaningful and reproducible investigations impossible and have to be avoided, practically by limiting the provided RF power.

In summary, the described limitations set the boundary conditions for the discharges operated and investigated in the present work. Generally, two different approaches are followed, depending in the applied antenna:

- In case of **inductive discharges** generated via the **helical coil**, the discharges are generally operated continuously, but the provided RF power is restricted to a maximum of 1 kW. This assures that neither excessive ohmic heating of the RF system nor deteriorating effects of the vessel walls caused by the interaction with the plasma occur. Once the discharges reach equilibrium, the measurement of the plasma parameters is performed.
- With an application of the **Nagoya antenna**, an RF power of the order of 1 kW or higher is required to generate a discharge. In order to prevent the occurrence of excessively high and possibly damaging temperatures within the RF system, the discharge operation time has to be effectively reduced in this case. Therefore, the discharges are operated in a quasi-pulsed mode, applying plasma-on and -off phases between two and five minutes in continuous succession. This approach allows to reach stable and reproducible plasma parameters typically after a few pulses (monitored via OES) while the heating of the RF system is kept at a tolerable level. Once the monitored emission of the discharges reaches a stable level from pulse to pulse, the required measurements are conducted in course of several successive pulses. In order to ensure the comparability between the discharges utilizing different antennas, all measurements applying the helical ICP coil which are directly compared to discharges generated via the Nagoya antenna have also been performed by applying the described pulsed operational mode.

In general, the described limitations can be avoided by dedicated experimental measures: in order to counteract the ohmic heating of the RF system, actively water cooled antennas and transmission lines can be applied. To counteract the deteriorating effects of the plasma on the dielectric vessel walls close to the coil/antenna, a Faraday screen can be applied. Both measures are a prerequisite at higher RF powers and thus commonly applied, e.g. at larger ion source test beds.



## 7 Inductive discharges at 1 MHz

As presented in chapter 2, inductively coupled hydrogen and deuterium plasmas generated at 1 MHz are the discharges currently applied in the RF driven ion sources for NNBI. In the present chapter, this scenario is discussed in detail as it serves as the baseline case for the comparison with ICPs at higher frequency and the application of wave heated discharges in the subsequent chapters 8 and 9. While hydrogen discharges are investigated as the typical reference case at first, isotopic differences relevant for the plasma heating mechanism are assessed specifically afterwards. The investigations within this specific chapter have been performed at a previous setup of CHARLIE lacking the expansion chamber, as briefly mentioned in chapter 5.1. This does not pose any limitations to the comparability with the results presented in the following chapters 8 and 9, which were obtained with an installed expansion chamber: the presence of the expansion chamber does not influence the inductive plasma generation regime, which has been checked experimentally. The results presented in this chapter are to a large extent the contents of a paper already published by the author [RBF17].

### 7.1 RF power transfer efficiency

The RF power transfer efficiency obtained in inductive hydrogen discharges driven at 1 MHz for varying the gas pressure between 0.3 Pa and 10 Pa is shown in figure 7.1 (a). The presented measurements are obtained at three different delivered RF powers of 250 W, 520 W and 800 W, respectively. With increasing RF power, the efficiency increases globally, and a broad maximum of  $\eta$  over pressure is observed between 1 and 3 Pa. With increasing power, the position of this peak slightly shifts from 1 Pa at 250 W to 3 Pa at 800 W, where the RF power transfer efficiency exceeds values of 90% for RF powers of 800 W. The efficiency is significantly lower at the low and high pressure limits where it drops to values below 50%, particularly for low RF power. At 250 W, sustaining an inductive discharge at the low and high pressure limits of 0.3 Pa and 10 Pa is no longer possible due to the decreased power absorption by the plasma.

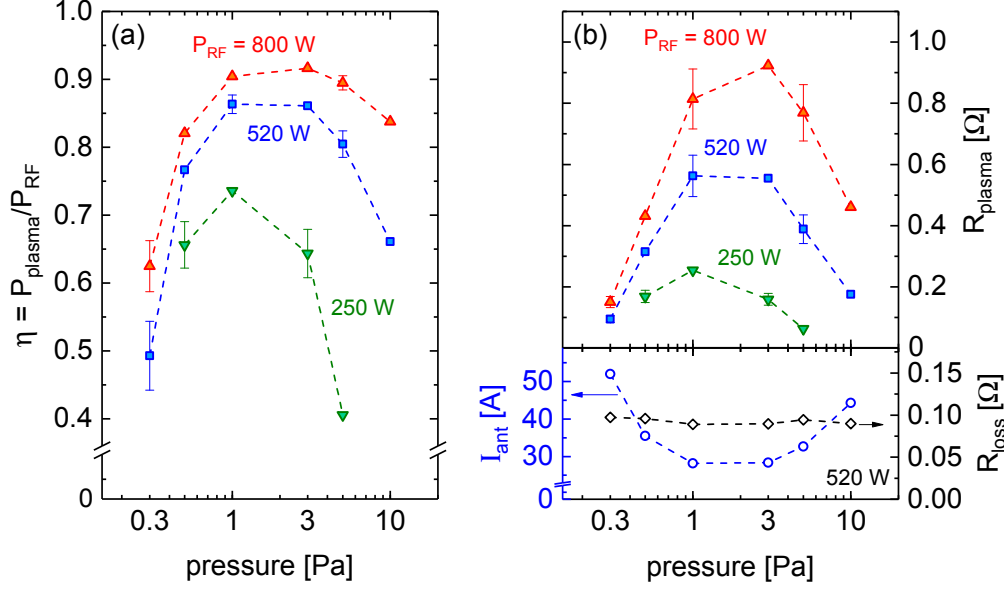


**Figure 7.1:** (a) RF power transfer efficiency  $\eta$  in hydrogen discharges at varying pressure and different values of the delivered RF power  $P_{\text{RF}}$ . In (b), the corresponding values of the plasma equivalent resistance at varying pressure and RF power are depicted (top), in addition to the antenna current during plasma operation and the loss resistance at 520 W (bottom).

Generally, the observed dependence of  $\eta$  on  $p$  and  $P_{\text{RF}}$  is connected with the behaviour of the plasma equivalent resistance  $R_{\text{plasma}}$  presented in 7.1 (b).  $R_{\text{plasma}}$  is in the range between 0.1  $\Omega$  and 1  $\Omega$  and displays analogous relative trends as  $\eta$  with respect to the varied parameters. The characteristic variation of  $R_{\text{plasma}}$  leads to a corresponding change of the antenna current  $I_{\text{ant}}$ , which is illustrated on the bottom of figure 7.1 (b) exemplarily for an RF power of 520 W. In the pressure region between 1 and 3 Pa,  $I_{\text{ant}}$  is around 28 A while it significantly rises towards higher and lower pressure, reaching values of 50 A. As the loss resistance is of roughly 0.1  $\Omega$  virtually independent of the operational parameters, the relative behaviour of the power loss term  $I_{\text{ant}}^2 R_{\text{loss}}$  is determined by the changing antenna current, which leads to the observed behaviour of  $\eta$ . The pressure dependent change of the current is therefore mainly a result of the varying power absorption by the plasma, which is proportional to the plasma equivalent resistance. In general, this behaviour is well comparable to the results of the power transfer efficiency of noble gas discharges that have been reported several times, e.g. by [Hop94, Kra08, KRP<sup>+</sup>16].

## 7.2 Plasma characterization and heating mechanism

In order to analyse the observed characteristic behaviour of RF power absorption, the analytical descriptions of the inductive heating provided in section 4.2 can be applied. This requires the experimental determination of several plasma parameters, foremost the electron density and temperature and the characteristic collision frequencies of electrons.

### 7.2.1 Relative spatial plasma profiles

In the present work, mainly axially averaged plasma parameters are discussed, which are considered to be representative for the global description of the discharge behaviour and the heating mechanism. In order to ensure that such an approximation is valid, the typical spatial profiles of the discharge and their respective dependence on the varied operational parameters have to be checked. Serving as the representative quantity for the spatial distributions within the discharge, mainly the electron density is treated in the following.

The distribution of the electron density in axial direction is measured by the moveable floating double probe. In figure 7.2 (a), an exemplary profile obtained at a pressure of 1 Pa and an RF power of 520 W between the end plate and the center of the discharge vessel is presented. The density is peaked in the heating region under the coil at a maximum value of  $4 \times 10^{17} \text{ m}^{-3}$  and gradually decreases towards the cylinder ends. Due to the symmetry of the coil and the discharge vessel, the spatial profiles are axially symmetric with respect to the discharge center, which has been checked by inserting the probe from the other side. Empirically, the measured profiles are found to be very well described by Lorentzian peak functions, as indicated for this example as well. In order to compare the probe measurements with the LOS-averaged plasma parameters obtained via OES and CR modelling, the mean value of the Lorentzian fit along the whole length of the cylinder is calculated, yielding in this case  $\langle n_e \rangle = 1.7 \times 10^{17} \text{ m}^{-3}$ .

In general, the relative shape of the axial density profile does not show a strong variation with the operational parameters of the discharge, in contrast to the absolute values which are discussed in the next chapter. At fixed pressure, virtually identical profiles are obtained at different RF power. If the pressure is varied, a weak yet systematic behaviour is observed as presented in figure 7.2 (b): if the

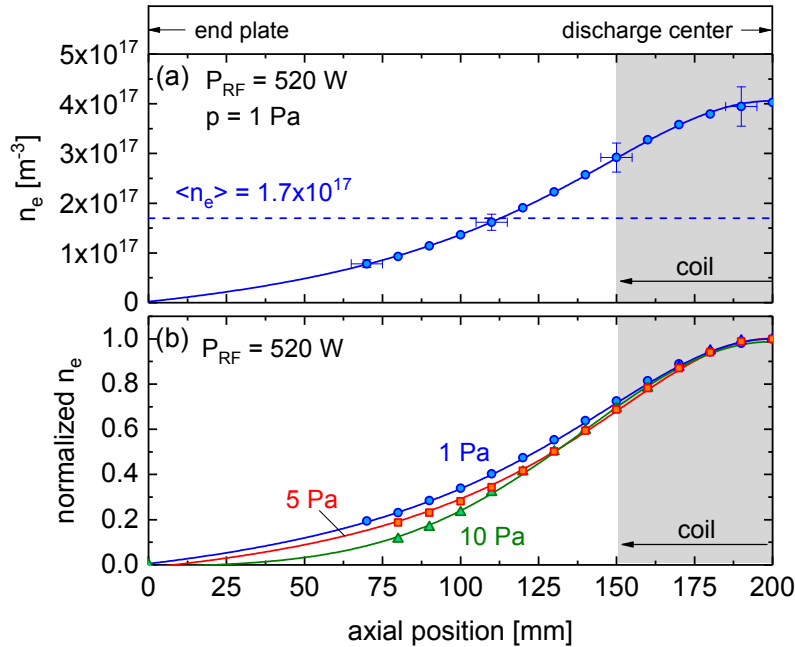


**Figure 7.2:** (a) Example of an axial profile of the electron density measured by the floating double probe. The data is fitted by the displayed Lorentzian peak function in order to evaluate the axially averaged density  $\langle n_e \rangle$ . (b) Axial density profiles at varying pressure. For both graphs, the extent of the coil as well as the end and the center of the discharge tube are indicated.

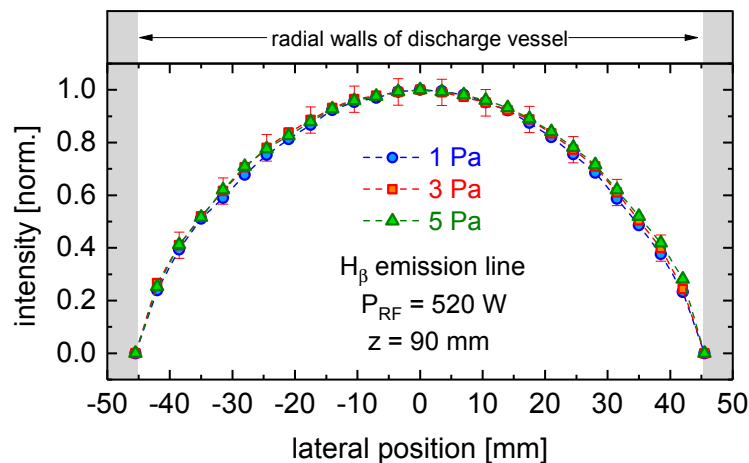


**Figure 7.3:** Normalized lateral intensity profiles of the atomic  $H_\beta$  emission line at an axial position  $z = 100$  mm between the coil and the end plate. Presented are profiles obtained at different pressure and a fixed RF power.

pressure is increased, the normalized profiles become slightly narrower. This is the typical observation in low pressure low temperature plasmas, caused by a shorter mean free path of the charged particles, leading to a slower diffusion and more pronounced density gradients [CB11].

The corresponding investigation of the radial discharge profiles is performed indirectly via spectroscopic measurements, since a radial variation the probe position is not possible for the present setup. By means of the moveable lateral LOS of OES (denoted #2 in section 5.1), intensity profiles of the atomic Balmer and the molecular Fulcher radiation are obtained. Apart from an absolute variation of the measured intensity with changing operational parameters, the resulting profiles do not show a significant radial dependence, neither on the RF power nor on the pressure. Exemplary, the normalized lateral intensity profiles of the  $H_\beta$  emission line at different pressures for a fixed RF power of 520 W are presented in figure 7.3. The profiles are obtained at the axial position  $z = 90$  mm (see figure 7.2) between the coil and the end plate. They are peaked on the cylinder axis and decrease towards the radial wall virtually identical for all pressures. The observed insensitivity of the intensity profiles with respect to  $p$  and  $P_{\text{RF}}$  indicates that the relative radial distribution of the plasma parameters is not strongly influenced by the operational parameters either.

Even though it is not discussed specifically in this work, the measured lateral emission profiles can be used to obtain radial emission profiles via *Abel inversion*. Subsequently these profiles can be compared to numerical simulations which are capable of calculating spatially resolved plasma parameters. For the present parameters, this has already been performed and is published within [BMR<sup>+</sup>17], where the measurements discussed within this chapter are compared with results of the numerical PIC-MCC<sup>1</sup> code *NINJA* [Mat17, MNO<sup>+</sup>17]. As reported therein, the radial electron density profiles are well described by a zero-order Bessel function, which corresponds to the typical expectation in cylindrically symmetric low pressure low temperature plasmas [LL05, CB11, Beh91].

In summary, both the relative axial and radial distributions of the plasma parameters show the typical characteristics expected in the discharge regime at hand and are mostly insensitive to the operational parameters  $p$  and  $P_{\text{RF}}$ . Conclusively, changes of the line of sight averaged parameters evaluated via OES can be solely contributed to a change of the global plasma parameters, and are not due to significant changes of the plasma's spatial distribution.

---

<sup>1</sup>Particle-in-cell Monte Carlo collision

## 7.2.2 Plasma parameters at varying pressure and RF power

The electron density  $n_e$ , the electron temperature  $T_e$  and the gas temperature  $T_{\text{gas}}$  at varying pressure and delivered RF power are presented in figure 7.4. In (a), the axial average of the electron density for different RF powers is displayed, which is determined by evaluating the profiles obtained by the floating double probe according to the approach presented in the previous chapter. The density is of the order of  $10^{17} \text{ m}^{-3}$  and increases with increasing RF power. Up to 3 Pa, it also increases with increasing pressure. In the region above 3 Pa, a deviant behaviour depending on the RF power is observed: for 800 W,  $n_e$  continues to grow, while for intermediate and lower power it saturates or even decreases in the high pressure region, which is directly connected to the analogous decrease of the RF power transfer efficiency at lower powers shown in figure 7.1. The electron density obtained via OES and CR modelling is exemplarily shown for  $P_{\text{RF}} = 520 \text{ W}$  in addition to the probe data. The correspondence to the axial average of the electron density obtained by the floating double probe is excellent, regarding both the absolute value and the relative trend.

In figure 7.4 (b), the electron temperature determined via OES and CR modelling at varying pressure is shown. For all powers applied, a monotonous decrease from about 5 eV at 0.3 Pa down to values slightly below 2 eV at 10 Pa is observed, which corresponds to the expected behaviour in low pressure discharges described by the ionization balance in chapter 3.4. The influence of the applied power is not pronounced: all values of  $T_e$  are within the error margins for a fixed pressure. Generally, a small increase of  $T_e$  with increasing power is present within the error bars due to a moderate increase of the gas temperature with increasing power, effectively reducing the neutral particle density.

The gas temperature is explicitly shown in figure 7.4 (c):  $T_{\text{gas}}$  increases steadily with the pressure in a range between 450 K at 0.3 Pa and 800 K at 10 Pa due to the increased collision rate and energy transfer between electrons and neutrals. With increasing power,  $T_{\text{gas}}$  rises by about 200 K between 250 W and 800 W. Consequently, the typical inequality  $T_e \gg T_{\text{gas}}$  is observed, which is characteristic for non-equilibrium low pressure low temperature plasmas.

The density ratio  $n_{\text{H}}/n_{\text{H}_2}$  evaluated via OES and collisional radiative modelling is found to be within a range of 0.1 and 0.6 for all operational parameters. Typically, it increases for higher  $T_e$  (i.e. at low pressure) and higher  $n_e$  (i.e. at high power) due to the dissociation of  $\text{H}_2$  via electron impact described in chapter 3.3. Selected

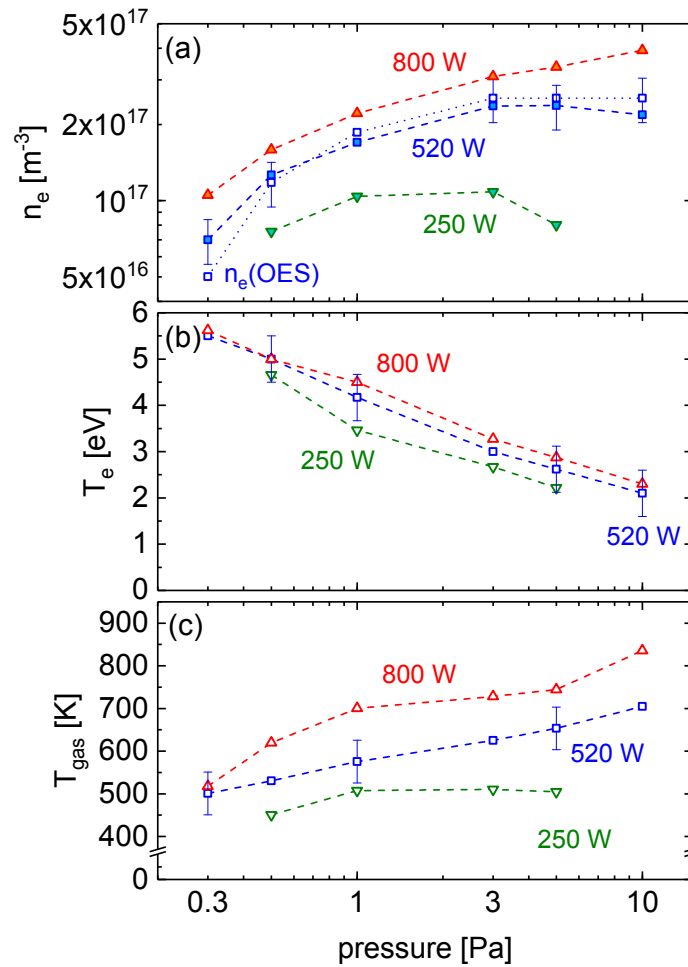


**Figure 7.4:** Plasma parameters of inductive hydrogen discharges driven at 1 MHz at varying pressure and RF power. Depicted in (a) is the electron density obtained by probe measurements (full symbols) and via optical emission spectroscopy and collisional radiative modelling (open symbols). In (b) the electron temperature is shown, evaluated by OES and CR modelling. (c) shows the gas temperature obtained via OES.

values of  $n_{\text{H}}/n_{\text{H}_2}$  are specifically shown in section 7.3 as part of the discussions concerning the isotopic differences between hydrogen and deuterium.

### 7.2.3 Inductive heating mechanism

In order to discuss the behaviour of the RF power transfer efficiency  $\eta$  presented in section 7.1 in further detail, the effective plasma conductivity  $\sigma_{\text{eff}}$  is calculated according to equation (4.13), as it is proportional to the power absorption of an inductively heated plasma defined in equation (4.6). This approach provides a 0-dimensional approximation of the characteristic dependencies of the power transfer and heating mechanism.

In order to evaluate the plasma conductivity  $\sigma_{\text{eff}}$ , measured electron density values and the effective collision frequency  $\nu_{\text{eff}}$  are taken into account. Regarding the latter, both the electron-neutral collision frequency  $\nu_{\text{en}}$  and the stochastic collision frequency  $\nu_{\text{stoc}}$  are calculated. The electron-neutral collision frequency is given by the sum of the collision frequencies of electrons with hydrogen atoms  $\nu_{\text{eH}}$  and molecules  $\nu_{\text{eH}_2}$ , respectively. Collisions with ions can be neglected due to their lower density. At the present conditions, the stochastic collision frequency is given by equation (4.11), since the electron transit frequency through the RF skin depth layer is much larger than the angular excitation frequency of  $2\pi \times 1$  MHz, yielding  $\alpha \ll 1$ .

In figure 7.5 (a), the calculated frequencies are presented at varying pressure at the RF power of 520 W. The collision frequency  $\nu_{\text{en}}$  is characterized by an almost linear increase with rising pressure due to its proportionality to the neutral particle density. Slight deviations from a linear dependence are due to a change of the neutral density caused by the observed steady increase of the gas temperature. Furthermore, there is an implicit influence of the electron temperature on  $\nu_{\text{en}}$  via the rate coefficients  $X_{\text{eH}}(T_e)$  and  $X_{\text{eH}_2}(T_e)$ . However, as there is only a weak variation of the electron momentum transfer cross sections of hydrogen atoms and molecules with  $T_e$  in the relevant energy region between 2 eV and 5 eV ([SEG87, YSH<sup>+</sup>08], see chapter 3.3), the impact of  $T_e$  on the electron collision frequency is almost negligible. In addition, the difference between the cross sections of atoms and molecules is fairly small in this energy range, which leads to the observation that the density ratio of atoms and molecules has no significant impact on the electron-neutral collision frequency either.

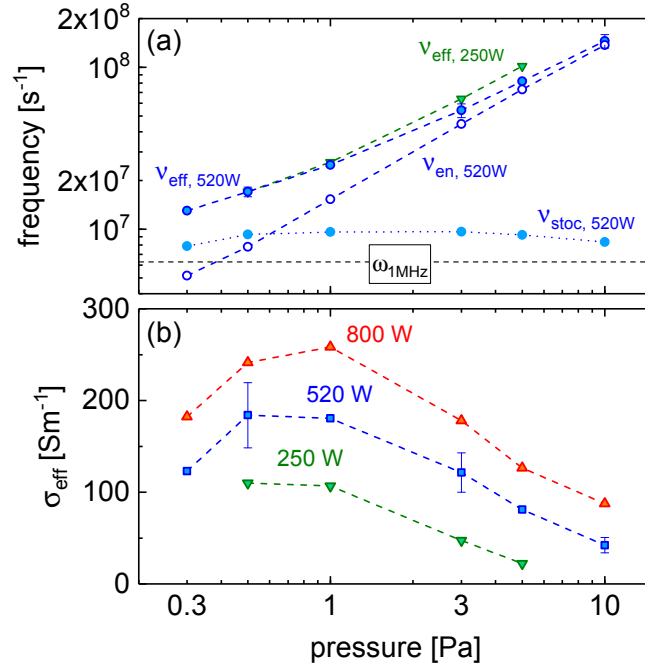


**Figure 7.5:** (a) Electron collision frequencies in hydrogen at varying pressure. For 520 W, the collision frequency of electrons with neutrals ( $\nu_{\text{en}}$ ), the frequency of the electron momentum change due to stochastic non-collisional heating ( $\nu_{\text{stoc}}$ ) and the effective sum of both components ( $\nu_{\text{eff}}$ ) is depicted. For a comparison,  $\nu_{\text{eff}}$  at 250 W is also included. (b) Real part of the complex (effective) plasma conductivity at varying pressure and delivered RF power in hydrogen.

The stochastic collision frequency displays only small variations, due to its dependence on both  $T_e$  and  $n_e$ , which depict a contradictory relative dependence on the pressure. Comparing both  $\nu_{\text{stoc}}$  and  $\nu_{\text{en}}$ , the expected dominance of ohmic heating at higher pressure is well reflected:  $\nu_{\text{en}}$  exceeds  $\nu_{\text{stoc}}$  by more than one order of magnitude at 10 Pa. Due to the negligible influence of stochastic heating in this region, the effective collision frequency is virtually equivalent to  $\nu_{\text{en}}$ . At low pressures of  $p \leq 1$  Pa though, the influence of stochastic heating becomes significant. At the low pressure limit of 0.3 Pa, the stochastic collision frequency even exceeds  $\nu_{\text{en}}$ . In consequence, the effective collision frequency deviates strongly from  $\nu_{\text{en}}$ , confirming that stochastic heating has to be considered in hydrogen discharges at low pressure. In contrast to the pressure, the RF power has only a minor influence on the evaluated collision frequencies. As an example, the effective collision frequency at a delivered RF power of 250 W is also included in figure 7.5 (a). The relative behaviour of  $\nu_{\text{eff}}$  at lower power is virtually the same as for 520 W, while the absolute frequency is slightly but globally higher.

This is mainly due to a slightly higher neutral density caused by the lower gas temperature. At higher RF power a slight reduction of  $\nu_{\text{eff}}$  is analogously observed due to a higher gas temperature. In addition, the constant value of the angular excitation frequency  $\omega_{\text{RF}}$  is indicated in 7.5 (a), which is globally lower than all of the individually evaluated effective collision frequencies. As discussed in section 4.2, this implies that in the present regime a lower collision frequency results in an increase of the plasma conductivity.

The real part of the complex plasma conductivity  $\sigma_{\text{eff}}$  is determined subsequently based on the plasma parameters discussed above and presented in figure 7.5 (b). With an increase of the RF power, the conductivity increases globally. For all three RF powers applied, an analogous behaviour with respect to the pressure is obtained:  $\sigma_{\text{eff}}$  describes a maximum between 0.5 and 1 Pa and decreases for both higher and lower pressures. In case of 250 W, no stable plasma operation is possible below 0.5 Pa. The position of the maximum appears to be slightly shifted to higher pressures with increasing RF power. In summary, the obtained picture resembles well the relative behaviour of the RF power transfer efficiency presented in figure 7.1, which allows for a detailed comparison between  $\eta$  (or analogously  $R_{\text{plasma}}$ ) and  $\sigma_{\text{eff}}$  in order to evaluate the individual contributions of the considered plasma parameters to the RF power absorption.

The increase of  $\eta$  as well as  $\sigma_{\text{eff}}$  for higher RF power is mostly caused by the increasing electron density. In addition, the observed slight decrease of the effective collision frequency with increasing  $P_{\text{RF}}$  leads to a further enhancement of the plasma conductivity: in the present case,  $\omega_{\text{RF}} < \nu_{\text{eff}}$  is globally valid. Consequently, a lower effective collision frequency increases the fraction  $\nu_{\text{eff}}/(\omega_{\text{RF}}^2 + \nu_{\text{eff}}^2)$ . In general, the characteristically peaked pressure dependence of the plasma conductivity is also well comparable to the RF power transfer efficiency. It is caused by an interplay of the electron density and the effective collision frequency. At low pressure,  $\nu_{\text{eff}}$  is minimal and thus close to the applied frequency  $\omega_{\text{RF}}$ , which increases the plasma conductivity. At the same time, the relatively low value of  $n_e$  at low pressure significantly limits the conductivity and therefore also the ability of the plasma to absorb power. With rising pressure the situation inverts: while the electron density is increased and proportionally enhances the plasma conductivity, the steady increase of  $\nu_{\text{eff}}$  simultaneously reduces  $\sigma_{\text{eff}}$ . Consequently, both  $\sigma_{\text{eff}}$  as well as  $\eta$  describe a peak at intermediate pressure and decrease at higher pressure, where the rising electron-neutral collision frequency reduces the plasma's capability to absorb the provided RF power.

However, a direct comparison of the figures 7.1 and 7.5 also reveals that the position of the pressure dependent peak of  $\sigma_{\text{eff}}$  is systemically shifted to slightly lower pressure, compared to the maximum of the RF power transfer efficiency. The cause of this local deviation cannot be positively identified, but several possibilities can be considered.

First, it is known that the EEDF in inductive discharges may deviate from a Maxwellian distribution, particularly at low pressures [GPA92, MDCK<sup>+</sup>09]. Since a Maxwellian EEDF has been globally considered for the evaluation of the electron-neutral collision frequency, this could also affect the evaluated plasma conductivity, particularly in the low pressure region. However, the dependence of  $\nu_{\text{en}}$  on the electron temperature, and thus on the mean electron energy is weak at the present conditions, as already discussed above. This indicates that the effect of a non-Maxwellian EEDF on the plasma conductivity is also moderate, and probably not prominent enough to serve as a possible explanation for the observed deviation.

Second, the observed behaviour may be caused by relative spatial variations which cannot be conveyed by the conducted 0-dimensional approximation of the power absorption: the followed approach does not account for the small changes of the spatial profiles of the involved plasma parameters with pressure and power and the associated influence of the induced electric field  $\tilde{\mathbf{E}}$  in the RF sheath. For a further detailed and spatially resolved treatment of the heating process, numerical modelling approaches are required. First steps towards such a numerical simulation of the heating process of low pressure hydrogen discharges are already carried out [Zie17]. In addition, the contradictions of  $\sigma_{\text{eff}}$  and  $\eta$  at low pressure may also be a result of a limited validity of the considered description of stochastic heating. As mentioned already in section 4.2, the ion plasma frequency of the investigated discharges is higher than the excitation frequency, in contrast to the assumptions made in [VLD<sup>+</sup>95].

Nevertheless, it is concluded that the qualitative dependencies of  $\eta$  on gas pressure and RF power are generally well resembled by the presented analytical considerations accounting for both collisional and collisionless heating mechanisms. The deduction of this correlation is considered to be a novelty with respect to  $\text{H}_2/\text{D}_2$  low pressure discharges. The performed analysis provides also a specific motivation for the investigation of higher excitation frequencies than 1 MHz which is presented in chapter 8: since the effective electron collision frequencies are globally higher than  $\omega_{\text{RF}}$ , the efficiency of the inductive power absorption could

be enhanced by increasing the excitation frequency in order get closer to the maximum at  $\omega_{\text{RF}} = \nu_{\text{eff}}$ .

In general, the investigations conducted within this work (including the results to be presented in the subsequent chapters 8 and 9) provide a diverse set of experimental data, characteristic for RF heated low pressure hydrogen discharges. Therefore, they have proven to be ideally suited to serve as valuable input for the benchmark of numerical codes dedicated to the simulation of such discharges [Mat17, Zie17].

### 7.3 Isotopic effects: comparison of hydrogen and deuterium

As introduced in chapter 3.2, the nuclear mass has only a negligible impact on the electronic states of hydrogen and deuterium and thus, many of the governing processes within low temperature low pressure discharges do not display any relevant isotopic differences. This leads to partially comparable plasma parameters in  $\text{H}_2$  and  $\text{D}_2$  at the same operational parameters. However, significant isotopic differences between hydrogen and deuterium are expected regarding the process of molecular dissociation.

The behaviour of the molecular dissociation can be experimentally investigated by evaluating the ratio  $n_{\text{H}}/n_{\text{H}_2}$  of the atomic to the molecular density in hydrogen - and analogously  $n_{\text{D}}/n_{\text{D}_2}$  in deuterium - via optical emission spectroscopy. Measured values of this ratio at varying pressure are shown in figure 7.6 (a) for both isotopes, exemplary at a delivered RF power of 250 W. A comparable relative dependence on the pressure is observed for both isotopes: both density ratios describe a maximum at 1 Pa and a decrease towards lower and higher pressure.  $n_{\text{D}}/n_{\text{D}_2}$ , which reaches values between 0.25 and 0.45, globally exceeds  $n_{\text{H}}/n_{\text{H}_2}$  roughly by a factor of two. An analogous isotopic difference of the same order of magnitude is globally observed, e.g. also at higher RF power. As expected from the electron impact dissociation cross sections provided in section 3.3, the atomic density in  $\text{D}_2$  plasmas is higher than in  $\text{H}_2$  at the same operational parameters. Furthermore, the absolute densities of atoms are in the same order as the density of the molecules. This implies that atoms may have a non-negligible influence on the RF power absorption process which is further assessed in the following.

As discussed in the previous chapter 7.2.3, the difference between atoms and molecules with respect to the total electron-neutral collision frequency is negligible

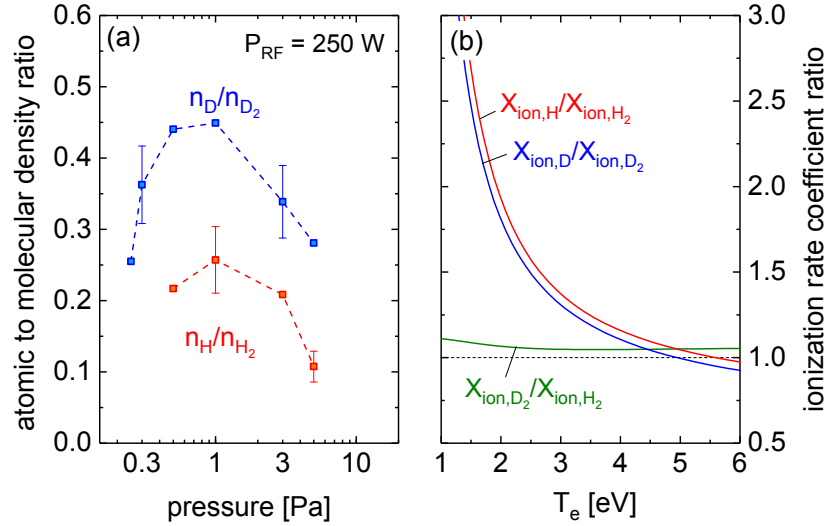


**Figure 7.6:** (a) Ratio of the atomic to the molecular density at varying pressure at  $P_{RF} = 250$  W in hydrogen and deuterium. (b) Ratio of the electron impact ionization rate coefficients of hydrogen and deuterium atoms and molecules in the electron temperature region of interest between 1 and 6 eV, calculated based on cross section data by [YSH<sup>+</sup>08, YKK<sup>+</sup>10, SEG87] and by assuming a Maxwellian EEDF. The horizontal dotted line indicates unity.

at the present conditions. In contrast, a significant deviation between atoms and molecules can be found for the electron-impact ionization, which is mainly caused by the lower ionization energy of hydrogen atoms (13.60 eV) compared to molecules (15.60 eV) - as introduced in chapter 3.3. In order to quantify this difference in view of the ionization rate, the rate coefficients  $X_{ion}(T_e)$  of electron-impact ionization are evaluated based on the electron-impact ionization cross sections provided in chapter 3.3. This is conducted for both the molecules  $H_2$  and  $D_2$  and the atoms H and D assuming a Maxwellian EEDF. Due to the different threshold energies, also the rate coefficients for atoms and molecules significantly deviate at low electron temperatures. This is illustrated in figure 7.6 (b). The rate coefficient ratios of  $X_{ion,H}/X_{ion,H_2}$ ,  $X_{ion,D}/X_{ion,D_2}$  and  $X_{ion,D_2}/X_{ion,H_2}$  are presented in the electron temperature range between 1 and 6 eV. The rate coefficients of electron-impact ionization of the atoms are generally higher than those of the molecules at electron temperatures below 5 eV, analogously for both  $H_2$  and  $D_2$ . This difference is particularly prominent at lower  $T_e$ . For electron temperatures above 6 eV the difference is small, as the influence of the lower ionization threshold of atoms decreases. In addition, the depicted ratio  $X_{ion,D_2}/X_{ion,H_2}$  shows that the ionization

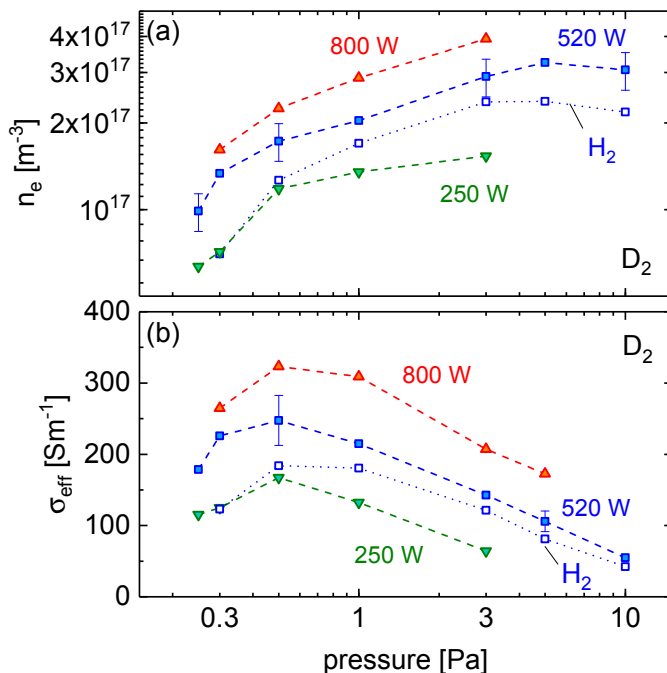


**Figure 7.7:** (a) Electron density in deuterium at varying pressure and delivered RF power. (b) Real part of the complex plasma conductivity  $\sigma_{\text{eff}}$  in deuterium. The results obtained in hydrogen at 520 W are included for a comparison, respectively.

rate coefficient of the D<sub>2</sub> molecule exceeds the one of the H<sub>2</sub> molecule globally by about 5%. This can be attributed to the involvement of ro-vibrational states in the dissociation processes of molecules, hence being influenced by analogous isotopic effects as the dissociation process [YKK<sup>+</sup>10].

In summary, a higher ionization rate is therefore expected in D<sub>2</sub> in comparison to hydrogen, mostly due to the increased atomic fraction (and to a minor extent because D<sub>2</sub> molecules are slightly easier ionized than H<sub>2</sub> molecules). This is in good agreement with the experimental results: the electron density measured by the floating double probe in deuterium discharges is depicted in figure 7.7 (a). In D<sub>2</sub>,  $n_e$  is generally characterized by the same relative dependences on the operational parameters that are observed in hydrogen. As illustrated by the direct comparison with the exemplary included density in H<sub>2</sub> at 520 W though, the absolute electron densities in deuterium are globally higher. The values obtained in deuterium generally exceed the ones in hydrogen by roughly 50%, and even more so at low pressure.

The power absorption mechanism in deuterium can be analysed analogous to hydrogen in section 7.2.3 by evaluating the plasma conductivity  $\sigma_{\text{eff}}$  according to

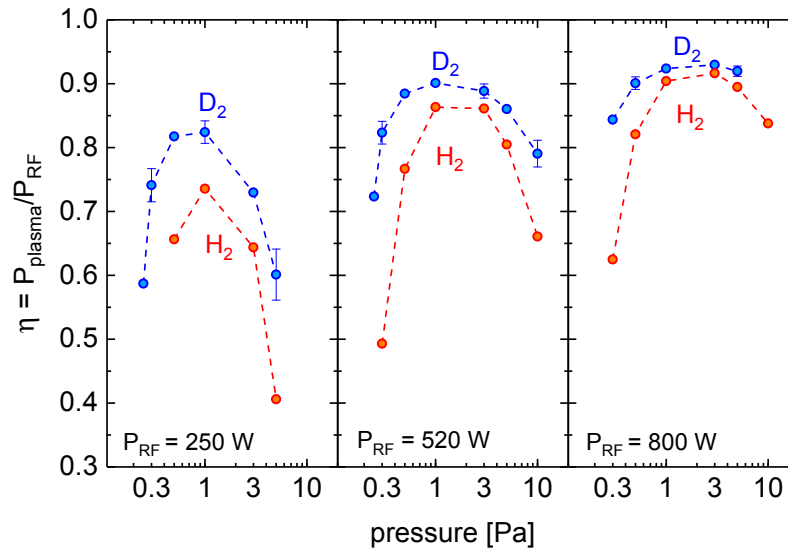


**Figure 7.8:** RF power transfer efficiency  $\eta$  in deuterium discharges at varying pressure and at three different values of totally delivered RF power; included for a comparison are the corresponding results obtained in hydrogen.

equation (4.13). This assessment again requires the consideration of the parameters  $T_e$  and  $\nu_{\text{eff}}$ . In general, their behaviour is well comparable to the one observed in  $\text{H}_2$ . Within the measurement uncertainty, the electron temperature in deuterium is similar to the values of  $T_e$  measured in hydrogen (and shown in figure 7.4) and is therefore equally dominated by the expected decrease with increasing pressure. The effective electron collision frequency is also virtually the same as in hydrogen. The calculated effective plasma conductivity in deuterium is shown in figure 7.7 (b), in comparison to the values obtained in  $\text{H}_2$  at 520 W. As expected, a virtually equal relative dependence of  $\sigma_{\text{eff}}$  on the operational parameters is observed for deuterium and hydrogen, since all input parameters depict comparable trends as well. However, the absolute conductivity is globally enhanced in  $\text{D}_2$ , which is a direct result of its proportionality to  $n_e$ .

In conclusion, the isotopic difference of  $\sigma_{\text{eff}}$  results in a globally increased power absorption capability of the deuterium discharges, which is in excellent agreement with the measurement of the RF power transfer efficiency shown in figure 7.8. A globally higher power absorption is measured in deuterium, while the relative dependencies of  $\eta$  on the operational parameters  $p$  and  $P_{\text{RF}}$  are well comparable for both isotopes. At higher powers and in the region of the pressure peak, the isotopic difference is only of a few percent. At higher and particularly at lower pressures though, it is significantly evident. For the example of an intermediate

power of 520 W at 0.3 Pa, an RF power transfer efficiency in D<sub>2</sub> of more than 80 % is obtained, while it drops below 50 % for H<sub>2</sub> at the same conditions. Due to this increased efficiency in deuterium, stable inductive plasma operation down to 0.25 Pa becomes possible even at such intermediate powers. The particularly increased efficiency in D<sub>2</sub> at lower pressures also correlates well with the behaviour of  $\sigma_{\text{eff}}$  shown in figure 7.7, as the difference between the conductivities of hydrogen and deuterium is also more prominent at low pressures of  $p < 1$  Pa.

In summary, the presented results illustrate that the atomic fraction in H<sub>2</sub>/D<sub>2</sub> low pressure discharges is a determining factor when the RF heating and power transfer mechanism is investigated: a higher atomic fraction leads to a significant increase of the ionization rate in the present electron temperature range, effectively increasing the electron density and thereby the capability of the plasma to absorb the provided RF power. This correlation, for the first time deduced in the course of this work, substantially contributes to the general understanding of the heating process of low pressure low temperature H<sub>2</sub>/D<sub>2</sub> plasmas. It explains many isotopic differences empirically observed before, e.g. that deuterium discharges typically require less RF power to be ignited in the first place and often achieve higher electron densities at the same operational parameters compared to hydrogen.

## 8 Inductive discharges at varying excitation frequency

The influence of the excitation frequency on inductively driven hydrogen and deuterium plasmas is investigated by comparing discharges generated at 2 MHz and 4 MHz with the reference case at 1 MHz. In analogy to the analysis in the previous chapter, the RF power transfer efficiency and the governing parameters of the inductive heating mechanism are discussed in a first step.

### 8.1 RF power transfer efficiency

The most prominent effects of a changed excitation frequency on the RF power absorption mechanism are present regarding its dependence on the pressure, due to the changed collisionality. Therefore, the RF power absorption - and in correspondence the inductive heating mechanisms in the next chapter - are mainly investigated at varying pressure, while the RF power is fixed at the intermediate value of 520 W. These examinations are exemplarily conducted for hydrogen discharges, as the behaviour in deuterium is mostly analogous and the same isotopic differences as discussed in section 7.3 are valid at higher frequency as well. Deuterium discharges and the influence of the provided RF power are specifically treated later as part of section 8.3, where the applicability and promises of a higher excitation frequency in view of larger ion sources is assessed in detail.

At first, the measured values of the loss resistance at the three applied frequencies are presented in figure 8.1 (a).  $R_{\text{loss}}$  increases systematically with frequency, from  $0.1 \Omega$  at 1 MHz,  $0.15 \Omega$  at 2 MHz up to approximately  $0.2 \Omega$  at 4 MHz. At 1 MHz and 2 MHz, no variation of the loss resistance with pressure apart from fluctuations within the characteristic measurement errors is observed. At 4 MHz, the loss resistance weakly decreases between 1 and 3 Pa compared to the mean value. In general, the increase of  $R_{\text{loss}}$  is found to be proportional to  $\sqrt{\omega_{\text{RF}}}$ , which corresponds to the expected behaviour due to the skin effect within an ohmic

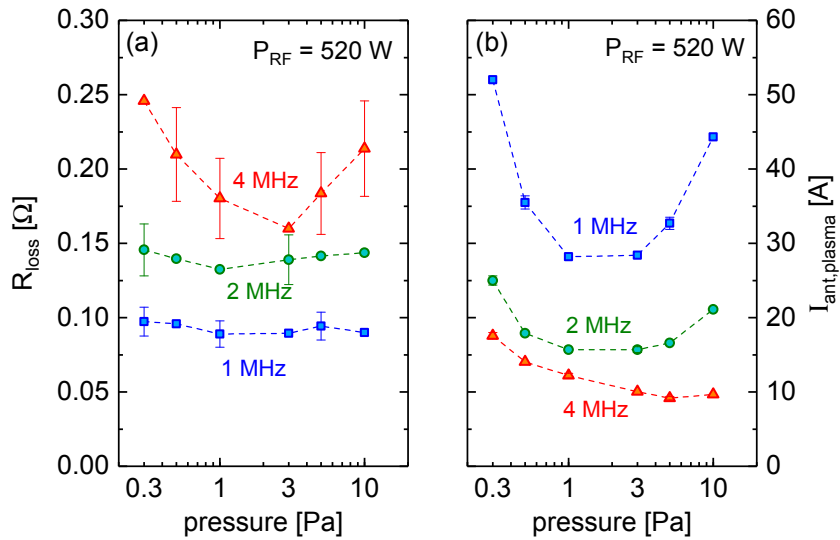


**Figure 8.1:** (a) Integral loss resistance and (b) antenna current during inductive plasma operation at varying pressure and excitation frequency in hydrogen.

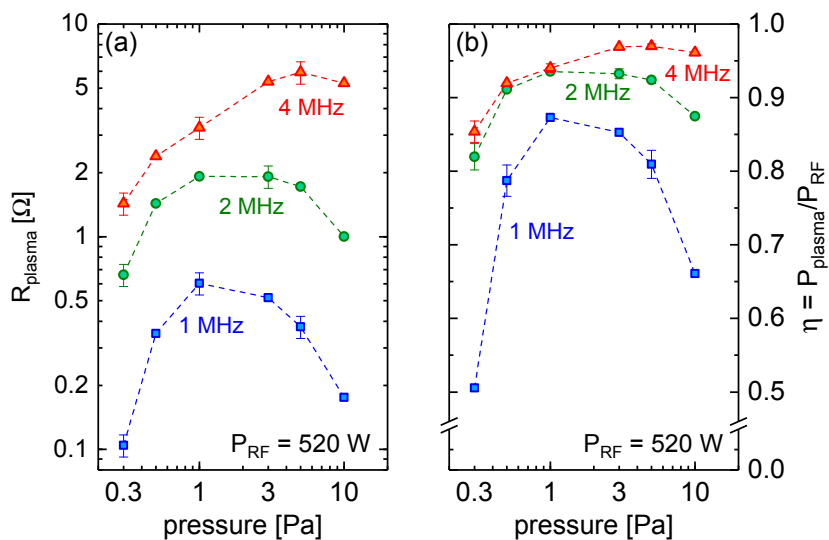


**Figure 8.2:** (a) Plasma equivalent resistance and (b) RF power transfer efficiency of inductively coupled discharges at varying pressure and different excitation frequencies in hydrogen.

resistor with a circular cross section, as introduced in chapter 4.1.

The antenna current measured during plasma operation is presented in figure 8.1 (b) and is characterized by an inverse dependence on  $\omega_{\text{RF}}$ : it decreases systematically at higher frequency, reaching values down to 10 A at 4 MHz. In analogy to the pressure dependence of  $I_{\text{ant,plasma}}$  observed at 1 MHz and presented in the previous chapter, also at higher frequencies a minimum of the current at varying pressure is evident. However, its position appears to be shifted to higher pressures for higher frequencies, precisely from 1 Pa at 1 MHz to 5 Pa at 4 MHz.

The observed trends of the antenna current can be well described if the correspondingly evaluated plasma equivalent resistance presented in figure 8.2 (a) is taken into account. In general, for all frequencies a comparable dependence of  $R_{\text{plasma}}$  on the pressure is observed, leading to the characteristic maximum at a specific pressure. The absolute resistance is increasing with a higher excitation frequency in the whole pressure range from 0.3 to 10 Pa. Corresponding to the behaviour of the antenna current, the position of the pressure dependent maximum is shifted monotonically to higher pressure by increasing the excitation frequency. Quantitatively,  $R_{\text{plasma}}$  is found to increase by almost one order of magnitude from 1 MHz to 4 MHz. At the high frequency maximum at 5 Pa, a plasma equivalent resistance of almost  $6 \Omega$  is measured.

Consequently, the reduction of the antenna current with rising frequency is mostly caused by the increase of the plasma equivalent resistance, even though the loss resistance is also increasing, yet at a much lower rate. This implies that also the fraction of the provided power that is actually absorbed by the plasma itself increases at a higher frequency relatively to the ohmic power losses. This is accordingly resembled within the observed behaviour of the RF power transfer efficiency illustrated in figure 8.2 (b). The relative dependencies of  $\eta$  are completely analogous to the ones found for  $R_{\text{plasma}}$ : the efficiency rises with frequency and displays the described maximum over pressure. At 5 Pa and 4 MHz, more than 95% of the provided power is absorbed by the plasma. At the low pressure limit of 0.3 Pa, the measured increase of the efficiency is quite significant, as it reaches values above  $\eta = 0.85$  for 4 MHz - compared to the case of 1 MHz, where half of the provided RF power is actually lost.

## 8.2 Plasma parameters and heating mechanism

The following evaluations are conducted by comparing the results obtained at 4 MHz directly with those provided by the reference case at 1 MHz. Since this is sufficient to highlight the influence of the excitation frequency, the discharges generated at 2 MHz are not specifically treated further on.

### 8.2.1 Relative spatial plasma profiles

In general, an influence of the excitation frequency on the spatial distributions of the plasma parameters cannot be excluded a priori, since the RF skin depth depends on  $\omega_{\text{RF}}$ . Assuming a collisional RF skin depth according to equation (4.8), its thickness  $\delta_{\text{coll}}$  is inversely proportional to  $\omega_{\text{RF}}$  yielding  $\delta_{\text{coll},4\text{MHz}} \approx 1/2 \delta_{\text{coll},1\text{MHz}}$  at otherwise equal parameters. In the present case, the RF skin depth at 1 MHz is typically of the order of 2 cm (and accordingly at 4 MHz about 1 cm). In principle, this leads to a shift of the plasma ionization and heating regime towards the wall at higher frequency, and may thus result in a change of the spatial profiles of the discharge.

First, the axial plasma profiles obtained by the floating double probe are considered. As an example, the normalized axial profiles of the electron density measured at the applied frequencies of 1 MHz and 4 MHz at a pressure of 1 Pa and an RF power of 520 W are depicted in figure 8.3. The profiles are virtually identical within their respective measurement errors. A comparable agreement between the profiles is found within the whole pressure and power range, which leads to the conclusion that the axial density profiles are not displaying any significant influences of the excitation frequency in the considered range. This corresponds to the expected behaviour that the determining factor of density gradients within a low pressure low temperature discharge is the (ambipolar) diffusion of charged particles to the wall [LL05, CB11]. This implies that the plasma profiles are determined by the experiment geometry (vessel and coil) and the parameters determining the mean free path of charged particles, such as the neutral particle density.

After all, the similarities between the axial profiles are not surprising, since the main effects due to the frequency dependent attenuation of the RF fields are expected in radial direction anyway. In order to gain information about possible relative changes of the radial distribution of the plasma parameters, again the lateral intensity profiles measured via OES are compared. Provided as an example

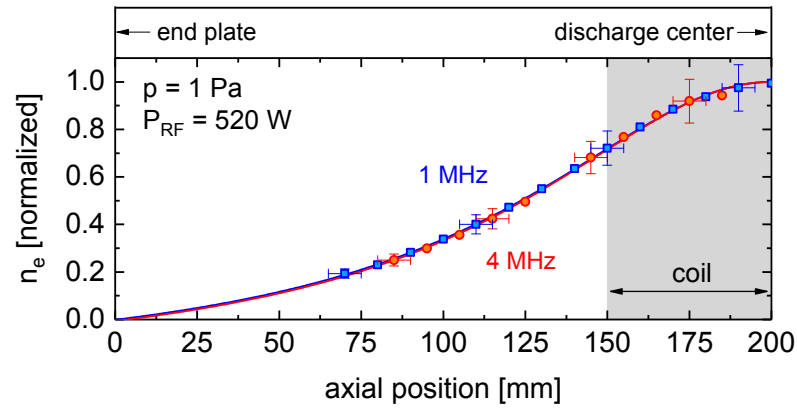


**Figure 8.3:** Exemplary axial profiles of the electron density measured by the floating double probe at the excitation frequencies 1 MHz and 4 MHz. The data is fitted by the displayed Lorentzian peak functions.

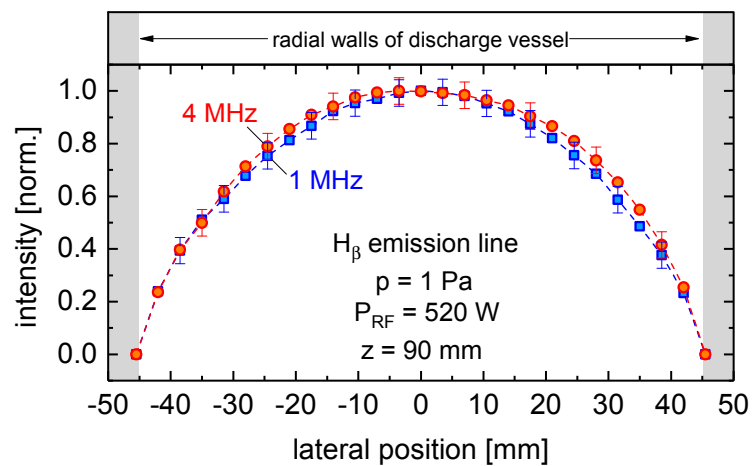


**Figure 8.4:** Normalized lateral intensity profiles of the atomic  $H_\beta$  emission line at the axial position  $z = 90 \text{ mm}$  between the coil and the end plate. Presented are profiles obtained at the excitation frequencies of 1 MHz and 4 MHz at the same pressure and RF power.

are the normalized intensity profiles of the  $H_\beta$  emission line measured at a pressure of 1 Pa, RF power of 520 W and varying excitation frequency in figure 8.4. The profiles appear to be very well comparable within their respective measurements errors. Nevertheless, a slightly but systematically broader profile is found at higher frequency, indicating that a smaller RF skin depth might lead to a small, yet measurable broadening of the radial profiles, since the RF heating regime is moving closer to the cylinder vessel walls. Deviations of comparable extent are also observed at different pressure and RF power, although not presented in detail here. However, the observed small variations are not considered to have a major influence on the discussion of axially averaged plasma parameters in the following section.

### 8.2.2 Plasma parameters at varying pressure

The axially averaged electron density obtained in hydrogen discharges via the floating double probe is presented in figure 8.5 (a) for applied frequencies of 1 MHz and 4 MHz. In both cases the density exhibits an increase with increasing pressure (except for 1 MHz at 10 Pa) roughly between  $1 \times 10^{17} \text{ m}^{-3}$  and  $4 \times 10^{17} \text{ m}^{-3}$ , whereas the values obtained at 4 MHz globally exceed those at lower frequency. The observed difference corresponds well to the behaviour of the RF power transfer efficiency: the deviation of  $\eta$  between 1 MHz and 4 MHz is the smallest in the intermediate pressure range where a comparable power is absorbed by the discharges, leading to electron densities that deviate only within the measurement error of the double probe of 25 %. At low and high pressures however, both the RF power transfer efficiencies and the electron densities deviate, mostly because the efficiency at 1 MHz drops significantly. In those limits, the density at 4 MHz is almost a factor of two higher.

In figure 8.5 (b), the related electron temperatures evaluated via OES are depicted. As already discussed in chapter 7.2.2,  $T_e$  generally decreases with increasing pressure in the range from 5 to 2 eV. The electron temperatures obtained at the two different frequencies show a very good agreement as the corresponding values are systematically within the respective error ranges of the measurement. Since also the gas temperature is virtually equal, it can be concluded that  $T_e$  is independent of the excitation frequency and appears to be mainly determined by the neutral particle density, in accordance to the behaviour expected due to the ionization balance in low pressure low temperature plasmas (see chapter 3.4).

Also the atomic to molecular density ratio does not exhibit a specific dependence

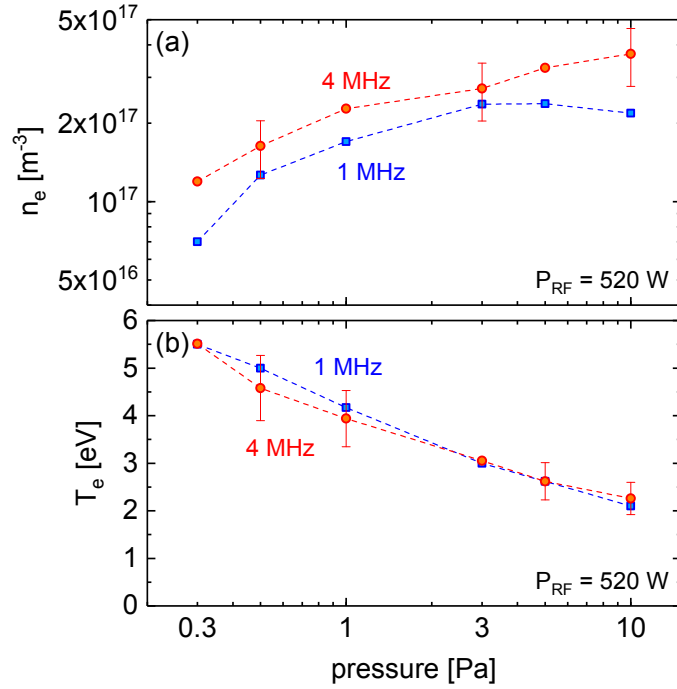


**Figure 8.5:** Plasma parameters of inductive hydrogen discharges driven at 1 MHz and 4 MHz at varying pressure at an RF power of 520 W. Depicted in (a) is the electron density obtained by double probe measurements. In (b), the electron temperature is shown, evaluated via OES and collisional radiative modelling.

on the applied frequency. It is measured to be in the range between 0.15 and 0.6, with an analogous dependency on the pressure and power for both frequencies. As the behaviour of  $n_{\text{H}}/n_{\text{H}_2}$  is dominated by the production process of atoms via electron impact dissociation of  $\text{H}_2$ , it is mostly determined by the plasma parameters  $n_e$  and  $T_e$ . In consequence, the atomic fraction is slightly enhanced at higher frequency due to the globally higher electron density. This correlation is further assessed in section 8.3, where measured values of  $n_{\text{H}}/n_{\text{H}_2}$  are provided.

### 8.2.3 Inductive heating mechanism

In order to describe the influence of the excitation frequency  $\omega_{\text{RF}}$  on the inductive heating mechanism, the effective plasma conductivity of the discharges driven at 4 MHz is evaluated according to equation (4.13), in analogy to the case of 1 MHz presented in chapter 7.2.3.

Required for this analysis are again the characteristic collision frequencies of electrons. While for the collision frequency of electrons with neutrals the identical

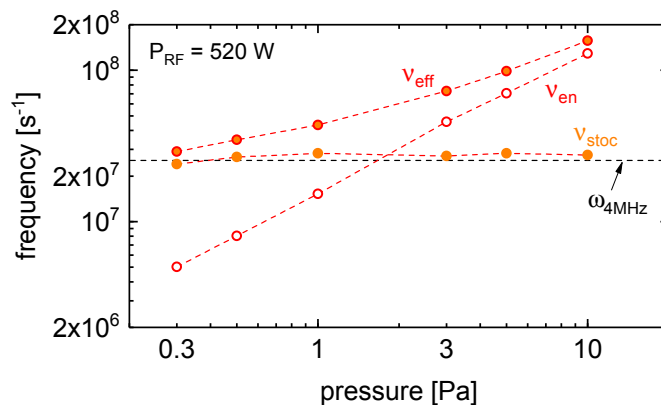


**Figure 8.6:** Pressure dependence of the electron collision frequencies at 4 MHz. Depicted is the collision frequency of electrons with neutrals  $\nu_{\text{en}}$ , the stochastic collision frequency  $\nu_{\text{stoch}}$  and the sum of both, the effective collision frequency  $\nu_{\text{eff}}$ . In addition, the value of the angular excitation frequency is indicated by the dashed horizontal line.

approach as in case of 1 MHz is followed, some considerations have to be made for the determination of the stochastic collision frequency. At the present discharge conditions and a driving frequency of 4 MHz, the transit frequency of electrons through the RF skin depth layer approaches the order of the angular excitation frequency. This yields values of the characteristic parameter  $\alpha$  of about 0.06. Consequently, the stochastic frequency and the RF skin depth are in this case described by the expressions introduced in equation (4.12).

In figure 8.6, the resulting collision frequencies are presented at varying pressure. Completely analogous to the case of 1 MHz, the electron-neutral collision frequency  $\nu_{\text{en}}$  is increasing approximately linear with the pressure due to its proportionality to the neutral particle density. Again, small perturbations of this linearity are caused by a change of the gas and electron temperatures. The stochastic collision frequency  $\nu_{\text{stoc}}$  is virtually constant over pressure and well comparable to the value of the angular excitation frequency of  $2\pi \times 4$  MHz. The two collision frequencies cross between 1 Pa and 3 Pa. Consequently, the effective collision frequency  $\nu_{\text{eff}}$  is dominated by  $\nu_{\text{en}}$  at high pressure and inversely determined mainly by  $\nu_{\text{stoc}}$  at low pressure. In the latter case, the effective collision frequency is close to the value of the angular excitation frequency. In general, the difference between  $\omega_{\text{RF}}$  and the effective collision frequency is significantly smaller than for 1 MHz, which is considered to be the main reason for the globally higher RF power absorption of the inductive discharges at higher frequency.

In the last step, the effective plasma conductivity is calculated. However, a

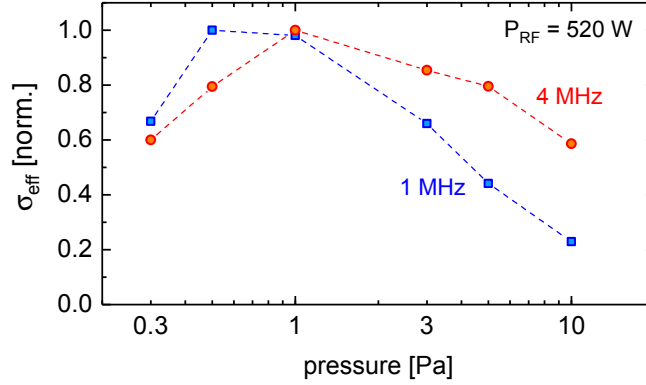


**Figure 8.7:** Normalized real part of the complex (effective) plasma conductivity at varying pressure in inductively heated hydrogen discharges at the excitation frequencies of 1 MHz and 4 MHz.

direct and global comparison of the absolute conductivities at 1 MHz and 4 MHz cannot be conducted in this case. As already discussed in section 8.2.1, the amplitude and the spatial attenuation of the induced electric field driving the RF currents in the plasma is strongly depending on the frequency. A variation of the frequency therefore leads to different spatial profiles of the field amplitude  $\tilde{\mathbf{E}}_{\text{RF}}$  within the discharge, which is correlated with the shift of the RF skin depth towards the radial walls at higher frequency. However, the plasma parameters are measured at the same radial position in a distance of 1 cm to the cylinder axis independent of the applied frequency. Consequently, the approximation made in chapter 4.2 - namely that the power absorption by the plasma is only proportional to  $\sigma_{\text{eff}}$  and variations of  $\tilde{\mathbf{E}}_{\text{RF}}$  can be neglected - is no longer valid. Nevertheless, a comparison of the relative pressure dependence of the conductivity can be still performed, since the variation of the RF skin depth with pressure is not as pronounced as with frequency and the assumption stated above is met.

In figure 8.7, the effective conductivities obtained at 1 MHz and at 4 MHz are shown in the considered pressure range, respectively normalized to their maximum value. The conductivity at 1 MHz is the same as already presented in chapter 7.2.3, characterized by a maximum located roughly at 0.5 Pa. While the conductivity obtained at 4 MHz exhibits a comparable general trend, the position of its maximum is found at 1 Pa. As also discussed in detail within chapter 7.2.3, the observed characteristically peaked behaviour of  $\sigma_{\text{eff}}$  is caused by an interplay of the pressure dependent electron density and the influence of the changing effective collision frequency. The provided description is analogously valid in the present case of 4 MHz, since both  $n_e$  and  $\nu_{\text{eff}}$  exhibit the same relative trends as for 1 MHz.

In conclusion, the observed shift of the maximum of the effective conductivity to higher pressures with a higher excitation frequency is in good agreement with the RF power transfer efficiency, which displays the same relative trend. However, analogously similar to the case of 1 MHz is the observation that the position of the pressure dependent peak appears to deviate between  $\sigma_{\text{eff}}$  and  $\eta$ . Possible reasons for this lacking correspondence have already been provided in section 7.2.3 and are equally relevant at higher driving frequency.

Nonetheless, the applied 0-dimensional description provides a conclusive characterization of the qualitative dependencies of the RF power absorption. According to this assessment, the increasing RF power transfer efficiency from 1 MHz to 4 MHz is considered to be caused by the globally decreased difference between the excitation frequency and the effective collision frequencies: at 4 MHz, the plasma conductivity is closer to its maximum at  $\omega_{\text{RF}} = \nu_{\text{eff}}$  than at lower frequency. This result allows for an outlook regarding an application of driving frequencies that exceed 4 MHz for a generation of inductively heated hydrogen plasmas. Firstly, since the RF power transfer efficiency is already considerably high in the whole pressure region of interest, no significant further improvement can be expected anymore, at least not within the pressure range of interest. In a pressure region exceeding 10 Pa, higher frequencies might still be beneficial even though this is not of particular relevance for the present case. In the low pressure limit, where the plasma heating mechanism is mainly collisionless, a significantly higher excitation frequency even leads to the violation of the boundary conditions of the described mechanism: the excitation frequency will eventually exceed both the electron collision frequency and the transit frequency of electrons through the RF sheath, which effectively renders this non-local heating scheme impossible. In conclusion, no further improvement of the RF efficiency of relevant extent is expected in the considered pressure range by a higher driving frequency. In other words, the applied frequency of 4 MHz is considered to be at, or at least sufficiently close to the global efficiency optimum for the inductive generation of low pressure low temperature discharges in hydrogen and deuterium.

In summary, the presented results clearly illustrate that the RF power transfer efficiency at an intermediate RF power of 520 W appears to be significantly improved at the low pressure limit of 0.3 Pa if the excitation frequency is increased with respect to the baseline case at 1 MHz. Since this pressure region is relevant for the production of negative ions for NNBI, a dedicated assessment of the applicability and the promises of a higher excitation frequency at RF driven ion sources is conducted.

## 8.3 Assessment of an application to RF driven ion sources

In order to evaluate the promises of applying a higher excitation frequency at large ion sources, the main differences between the discharges investigated in this work and the inductively heated plasmas of RF driven ion sources for NNBI have to be considered: the magnitude of RF power, the diameter of the discharge chamber and the application of a metallic Faraday screen between the plasma and the dielectric discharge vessel (see section 2).

In the present laboratory experiment, up to 1 kW can be applied to generate plasmas within the vessel of a diameter of 9 cm, whereas in larger ion sources the typically provided RF power is in the region up to 100 kW and the driver diameter is around 25 cm. Due to this difference, the RF power density  $P_{\text{RF}}/V$  in large ion sources such as the IPP prototype source is about one order of magnitude higher than at the present laboratory setup. On the one hand, the application of a Faraday shield can lead to additional RF losses and or a lower RF power transfer efficiency, as a fraction of the provided RF power is deposited within the metallic shield due to eddy currents and the capacitive discharge mode is suppressed [Hop94]. On the other hand, the metallic Faraday screen significantly changes the surface recombination probability of atoms compared to an entirely dielectric vessel, as described in section 3.3.

As a result, the typical electron density in ion source drivers is about five times higher than at the present experiment. In contrast, well comparable atomic fractions can be achieved, since the surface recombination rate at CHARLIE without a Faraday screen is much lower. In order to gain relevant information with the present setup regarding the high power regime, the power dependence of the RF power transfer efficiency and the plasma parameters being crucial for the production of negative ions are specifically considered. Accordingly, the parameters  $\eta$ ,  $n_e (= n_{\text{ion}})$  and  $n_{\text{H}}/n_{\text{H}_2}$  are evaluated in the following in the range up to 1 kW, comparing discharges driven at 1 MHz and 4 MHz. The pressure is kept constant at the typical operation point of large ion sources of 0.3 Pa, while hydrogen and deuterium are considered both. Even though a NNBI system for DEMO will have to be specifically optimized for D<sub>2</sub> operation, hydrogen plasmas are of importance regarding diagnostic applications and for ion source development.

The RF power transfer efficiency is shown in figure 8.8 at varying RF power. In general,  $\eta$  is systematically increasing with the provided  $P_{\text{RF}}$  in each case. As

described in section 7.2.3, this can be attributed to the equally increasing electron density, which will be confirmed in the following. In part (a), the values obtained in hydrogen discharges are depicted. In correspondence to the results presented in the previous chapter, the efficiency at 4 MHz globally exceeds  $\eta$  at 1 MHz. However, the relative difference between both is reduced at higher power. The RF power transfer efficiency at 1 MHz increases significantly from 0.45 at 300 W to 0.7 at 1000 W. At 4 MHz on the other hand, the increase of  $\eta$  is rather moderate between 0.79 and 0.92 due to the already higher total efficiency. For deuterium, a comparable relative trend is observed in figure 8.8 (b). The absolute efficiency is globally higher than in hydrogen due to the isotopic effects discussed in chapter 7.3. The RF power transfer efficiency in  $D_2$  at 1 MHz increases up to 0.9 at 1 kW, which is sufficient to achieve the level of  $\eta$  that is reached by applying 4 MHz, yet at lower RF powers. To summarize, for both  $H_2$  and  $D_2$  the relative differences of  $\eta$  due to the varying excitation frequency tend to get less pronounced at higher RF power, even though a higher frequency still leads to a systematically higher power absorption by the plasma.

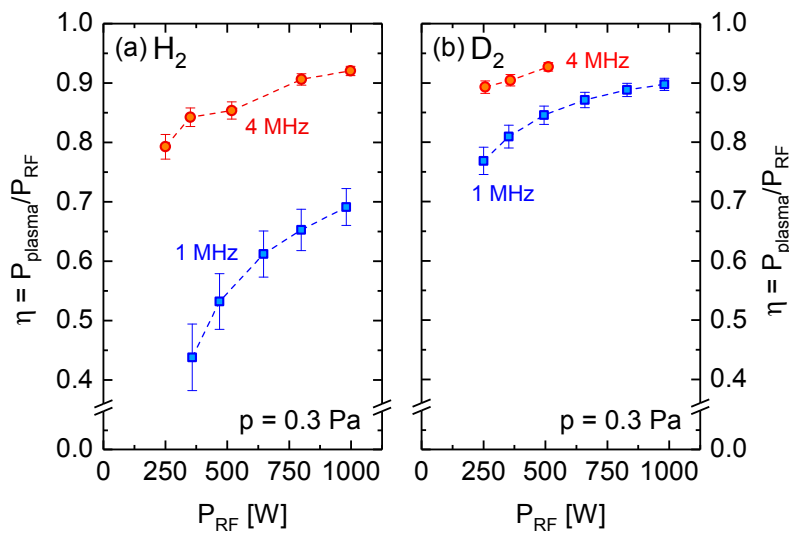


**Figure 8.8:** RF power transfer efficiency of inductive discharges generated at varying RF power and different excitation frequencies at a pressure of 0.3 Pa. In (a), results obtained in hydrogen are depicted, while in (b) the corresponding ones in deuterium are shown.

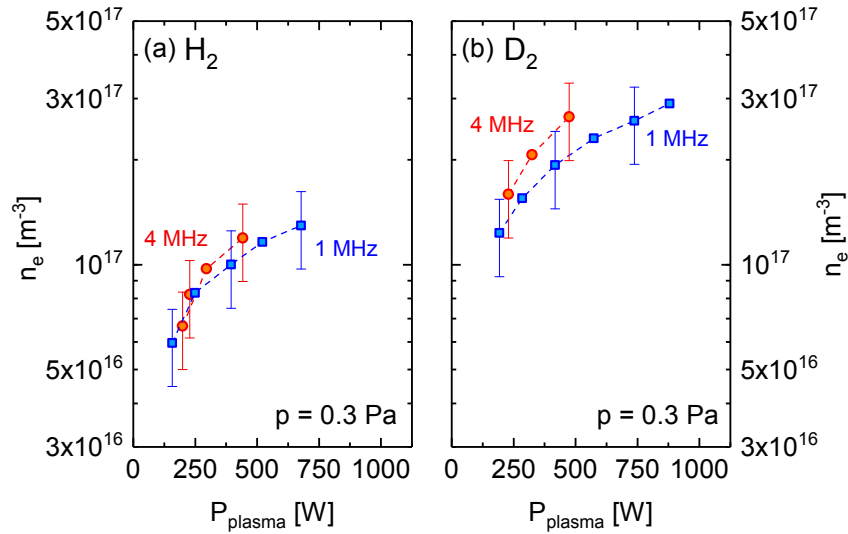


**Figure 8.9:** Electron density depending on the power  $P_{\text{plasma}}$  that is absorbed by the plasma for different excitation frequencies. In part (a), results obtained in hydrogen are depicted, while in part (b) the corresponding ones in deuterium are shown.

The corresponding power dependence of the electron density is regarded in figure 8.9. In this case, the density is plotted directly against the power  $P_{\text{plasma}}$  which is absorbed by the plasma and not against  $P_{\text{RF}}$ , in order to account for the changing RF power transfer efficiency. In general, for each excitation frequency and both hydrogen in part (a) and deuterium in part (b), a linear proportionality of  $n_e$  to the absorbed power is observed (appearing as a logarithmic increase in the graphs due to the logarithmic density scale, though). This corresponds to the typical behaviour of ICPs in the low pressure low temperature range and is equally predicted by the power balance introduced in chapter 3.4. The density in deuterium is globally about 2 times higher than in hydrogen, where it varies in the range between  $6 \times 10^{16} \text{ m}^{-3}$  and  $1.5 \times 10^{17} \text{ m}^{-3}$ . However, for both  $\text{H}_2$  and  $\text{D}_2$ , no significant difference between the two excitation frequencies is evident, since only variations within the corresponding error bars of the measurement occur. Consequently, the same density can be achieved independent of the driving frequency if the same power is absorbed by the discharge.

Serving as a measure for the atomic fraction within the discharges, the density ratio of atoms and molecules is analysed. It is shown in figure 8.10 depending on the power that is absorbed by the plasma. In general, again a global increase of  $n_{\text{H}}/n_{\text{H}_2}$  with rising  $P_{\text{plasma}}$  for all considered cases is given. In deuterium (b), the

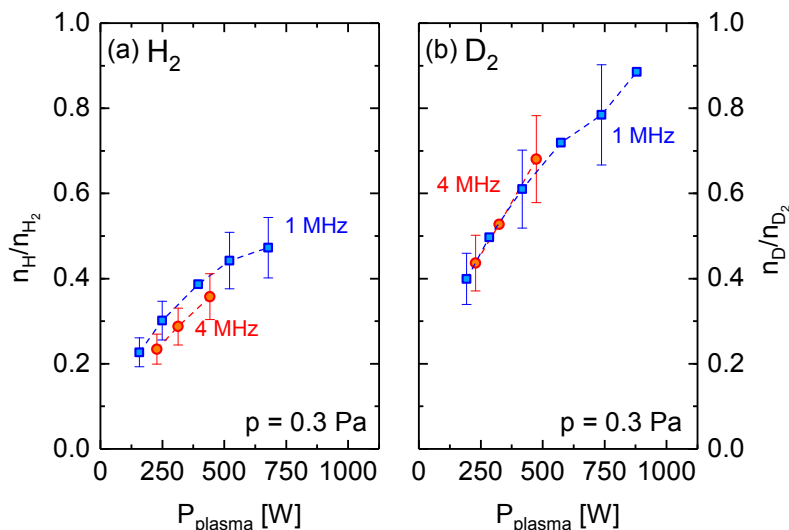


**Figure 8.10:** Density ratio of atoms to molecules depending on the power  $P_{\text{plasma}}$  that is absorbed by the plasma for different excitation frequencies. In part (a), results obtained in hydrogen are depicted, while in part (b) the corresponding ones in deuterium are shown.

density ratio is about two times higher than in hydrogen (a) at corresponding powers, in agreement with the isotopic differences described in chapter 7.3 and the behaviour of  $\eta$  and  $n_e$  observed above. Neither for hydrogen nor for deuterium any influence of the excitation frequency is evident that exceeds the uncertainties of the measurement. This is in good agreement with the expected behaviour, if the electron impact dissociation of H<sub>2</sub> is considered to be the dominant production channel of H. Since neither  $n_e$  nor  $T_e$  exhibit an influence on the excitation frequency at the same  $P_{\text{plasma}}$  and increase with power, the dissociation rate  $r_{\text{diss}} \propto n_e X_{\text{diss}}(T_e)$  is also independent of  $\omega_{\text{RF}}$  and hence, increases with power. However, the atomic fractions achieved at the present setup are remarkably high: at a power of 1 kW, the density ratio in deuterium reaches values of 0.9, which is even higher than typically achieved at large ion sources operated at much higher RF powers. This is a direct consequence of the dielectric (quartz) vessel walls. Applying the simple dissociation balance introduced in equation (3.29), an effective recombination coefficient  $\gamma$  of atomic hydrogen at the wall of the order of 0.03 is estimated, which is at the upper limit of the parameter range of  $\gamma$  typically reported for quartz surfaces. In contrast, an analogous estimation for typical ion source driver parameters ( $T_e \approx 10 \text{ eV}$ ,  $n_e \approx 10^{18} \text{ m}^{-3}$ ,  $T_{\text{gas}} \approx 1200 \text{ K}$ ,  $n_H/n_{H_2} \approx 0.4$  [MW<sup>+</sup>11, FSW<sup>+</sup>13]) yields a value of  $\gamma$  around 0.5. In accordance

with the literature values presented in section 3.3, this is typical for metallic surfaces and a result of the applied Faraday screen.

### Discussion and assessment in view of ion sources for NNBI

Considering the presented parameters simultaneously in the final step, several conclusions can be drawn. Virtually identical electron densities and atomic fractions can be achieved with both applied frequencies given that the absorbed power  $P_{\text{plasma}}$  is equal (at the same operational parameters and discharge geometry). Vice versa, neither  $n_e$  nor  $n_{\text{H}}/n_{\text{H}_2}$  ( $n_{\text{D}}/n_{\text{D}_2}$ ) exhibit an explicit dependence on the applied frequency apart from the implicit frequency effects due to  $P_{\text{plasma}}$  and the entire discussion regarding the frequency dependence can hence be reduced to the observed behaviour of  $\eta$ .

The RF power transfer efficiency increases with RF power, which is due to the increasing electron density. At high RF power, this eventually leads to a globally high  $\eta$  which exhibits only a negligible dependence on the collisionality term  $\nu_{\text{eff}}/(\nu_{\text{eff}}^2 + \omega_{\text{RF}}^2)$  of  $\sigma_{\text{eff}}$ . If the effective collision frequency  $\nu_{\text{eff}}$  and the excitation frequency  $\omega_{\text{RF}}$  are roughly of the same order of magnitude, a difference within the excitation frequency of a few MHz will eventually become irrelevant as the behaviour is dominated by the high electron density. This explains the observations made in figure 8.8: with increasing power, the frequency induced differences of the RF power transfer efficiencies are more and more reduced. Based on this behaviour, it is anticipated that the frequency dependence of the RF power absorption is small and almost negligible at higher powers exceeding the presently available range.

If this result is transferred to the scenario of large ion sources driven at high RF power, the same conclusions can be drawn: at typical driver plasma parameters at 0.3 Pa, an effective electron collision frequency of  $\nu_{\text{eff}} \approx 2.5 \times 10^7 \text{ s}^{-1}$  can be estimated. This value is about two times higher than the effective collision frequencies observed within this work at the same pressure. Since the collision frequencies are in the same order of magnitude, the presently deduced evaluation can be qualitatively transferred: at the typical (and required) parameters of an ion source driver plasma, changing the excitation frequency within a few MHz has only a negligible impact on the RF power transfer efficiency, and hence on the power absorption by the plasma. In other words, the currently applied frequency of 1 MHz is assumed to be already sufficiently close to the optimum value ( $\nu_{\text{eff}} \approx \omega_{\text{RF}}$ ). Applying frequencies much higher (or even lower) than 1 MHz is expected to eventually result in a reduction of  $\eta$ .

In addition, these conclusions remain basically unchanged even if the specific conditions at large and powerful ion sources are considered. At the vessel diameter of about 25 cm presently used at ion sources, no frequency differences are expected: a possible limitation due to an RF skin depth exceeding the vessel dimensions is well out of reach, since the estimated skin depth at 1 MHz and typical parameters is of the order of 2 cm, and further decreasing at higher frequency. The anticipated reduction of the RF power transfer efficiency due to the applied Faraday screen is expected to be more pronounced at higher frequency, since the voltage drop across the coil increases with the applied frequency and capacitive coupling is thus more prominent. In view of the high RF powers required at ion sources, the increased voltage drop across the antenna at higher frequency furthermore increases the risk for electrical breakdowns and arcing between the coil windings, which is critical in view of the required high reliability of an ion source for DEMO. In other words, these aspects even favour the application of a low excitation frequency.

In summary, the obtained results lead to the final conclusion that applying a higher excitation frequency at ICP drivers of ion sources for NNBI does not entail the potential to decisively reduce the RF power consumption and may even entail critical disadvantages with respect to the required high reliability. Based on the results obtained within this work, it is suggested that this approach is ruled out as a potential alternative in view of DEMO.

## 8.4 Effects of an external magnetic field

In preparation of the next chapter discussing wave heated discharges, a short assessment of the influence of a static axial magnetic field on the discharge properties of ICPs driven by the helical coil is conducted. Within the main parameter ranges of interest ( $0.3 \text{ Pa} \leq p \leq 1 \text{ Pa}$ ,  $P_{\text{RF}} \leq 1 \text{ kW}$ ,  $f = 4 \text{ MHz}$ ), a characteristic behaviour is observed if a magnetic field  $B_0$  is applied: for very low fields up to roughly 1 mT, no prominent influence on the discharge properties is observed within the measurement uncertainties. If the magnetic field is increased further however, the plasma generation is hindered (well observable e.g. via a reduced RF power transfer efficiency) until eventually, the plasma cannot be sustained and is shut down. This occurs typically in the range between 2 mT and 3 mT, depending on the current operational parameters.

This behaviour is caused by the magnetization of charged particles. On the one hand, the axial magnetic field results in a changed radial diffusion as described in chapter 3.5. On the other hand, it effectively hinders the inductive plasma heating mechanism itself: as it is presented in chapter 3.5, the regime of a few mT corresponds to the region where electrons are fully and ions are partly magnetized. In this case, the mobility of electrons and ions perpendicular to the magnetic field is generally reduced [LL05]. As a result, also the perpendicular plasma conductivity decreases in comparison to the field free case [Bit04]. Since at the present geometry the applied helical coil mainly induces an azimuthal plasma current (which is also oriented perpendicular to  $\mathbf{B}_0$ ), the inductive power absorption is strongly reduced by an increasing magnetic field, resulting in the observed behaviour. Specific investigations regarding the performance of a helical ICP in the presence of a magnetic field have already been conducted prior to this work [BGR<sup>+</sup>16, Gut14]. Even though these were performed at a higher excitation frequency of 13.56 MHz, the qualitative results are well comparable.



## 9 Discharges generated by a Nagoya-type helicon antenna

Discharges generated by the Nagoya type-III helicon antenna in hydrogen and deuterium are investigated at the excitation frequency of 4 MHz. At lower frequency, no plasma generation is possible in the present case due to the limited RF power, as described in chapter 6. At first, the operation of the Nagoya antenna without the application of an external magnetic field is discussed. This allows to deduce analogies to the inductive discharges generated by helical coil in order to highlight specific changes of the discharge properties once a static magnetic field is applied.

### 9.1 Inductive operation without external magnetic field

As described in chapter 4.3, the Nagoya antenna can be regarded as a one-turn coil. If no magnetic field is applied, it can therefore be utilized to generate a plasma via inductive heating - analogously to the five-turn helical coil discussed in the previous chapters. The main difference between the two antennas apart from the twisted geometry is their inductance: since the Nagoya antenna only consists of one loop, its measured inductance is only about  $0.7 \mu\text{H}$ , which is significantly smaller than the inductance of the helical coil of  $2.4 \mu\text{H}$  (see also chapter 6.1). In consequence, a higher RF current is generally required to ignite and sustain inductive discharges with the Nagoya antenna, which usually implies that also a higher RF power has to be provided.

To illustrate the differences and similarities between both antennas, discharges generated at varying pressure at a fixed RF power of 1 kW are discussed. At these parameters, the current through the Nagoya antenna is in the range between 50 A and 60 A during plasma operation. This is considerably higher than the typical currents measured for the helical coil between 15 A and 20 A at the same

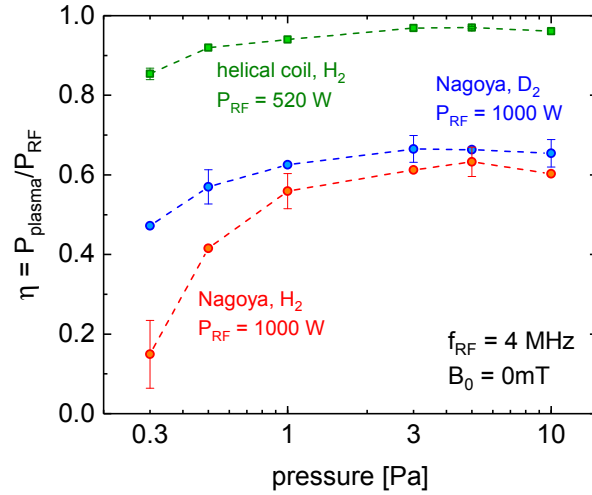


**Figure 9.1:** RF power transfer efficiency of inductive discharges generated by the Nagoya antenna in  $H_2$  and  $D_2$  at varying pressure and  $P_{RF} = 1 \text{ kW}$ , without the application of an external magnetic field. Included for a comparison are the results obtained in hydrogen with the helical coil at  $P_{RF} = 520 \text{ W}$ .

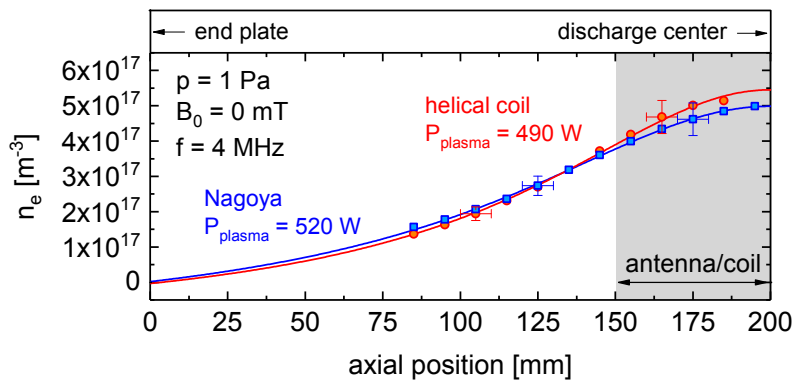


**Figure 9.2:** Axial profiles of the electron density measured by the floating double probe at the excitation frequency of 4 MHz comparing the helical coil and the Nagoya antenna. The data was obtained in hydrogen at a pressure of 1 Pa at  $B_0 = 0$ . With both antennas, a comparable power of  $P_{\text{plasma}} \approx 500 \text{ W}$  is deposited in the plasma. The data is fitted by the displayed Lorentzian peak functions.

conditions (see chapter 8.1). As a result, the RF power transfer efficiency of discharges generated via the Nagoya antenna is significantly reduced compared to the helical coil, which is illustrated in figure 9.1. With the Nagoya antenna,  $\eta$  only reaches values of slightly more than 60% at its maximum around 5 Pa. At lower pressures, the efficiency drops significantly. However, the observed relative pressure dependence is consistent with the results obtained for the helical coil that are described in the previous chapter. For a comparison, the ICP results at 4 MHz and an RF power of 520 W are exemplarily included in figure 9.1. Also for the Nagoya antenna,  $\eta$  in deuterium is again globally higher than in hydrogen.

The lower efficiency in case of the Nagoya antenna consequently requires higher RF powers to couple the same power  $P_{\text{plasma}}$  to the plasma compared to the helical coil. If the power absorbed by the plasma is approximately the same however, virtually equal plasma parameters can be obtained with both antennas. At the chosen example of  $P_{\text{RF}} = 900$  W for the Nagoya antenna and  $P_{\text{RF}} = 520$  W for the helical coil this situation is observed for  $p = 1$  Pa. At these parameters, about 500 W are absorbed by the plasma in each case. Serving as a representative example, the axial profiles of the electron density obtained by the floating double probe with both antennas are depicted in figure 9.2. As illustrated, both the profiles and the absolute values of the densities show an excellent agreement within the measurement error. Such a correspondence is systematically observed for all other measured parameters as well. This leads to the conclusion that the evaluated characteristics of ICPs in the previous chapters 7 and 8 are equally valid for the inductive discharges generated by the Nagoya antenna. In other words, the discharges driven by the Nagoya antenna at 0 mT can be considered as a reference for ICPs, e.g. if an external magnetic field is applied and the discharge changes from the inductive to a wave-assisted heating mode, which is conducted in the following sections.

## 9.2 Discharge operation with external magnetic field

Discharges in hydrogen and deuterium generated via the Nagoya helicon antenna in the presence of an external magnetic field  $B_0$  in axial direction between 0 and 12 mT are investigated. The presented measurements are obtained at a fixed RF power of 1 kW and at different pressures of 0.3, 0.5 and 1 Pa. This allows for a general characterization of the typical discharge properties and a comparison to the case of purely inductive heating at  $B_0 = 0$ .

### 9.2.1 RF power transfer efficiency

Figure 9.3 shows the RF power transfer efficiency of hydrogen and deuterium discharges at varying magnetic field  $B_0$ . In correspondence to the results found for ICPs, the efficiency in deuterium is globally higher than in hydrogen due to isotopic differences discussed in chapter 7.3. For all three pressures investigated, the same relative behaviour depending on  $B_0$  is observed: starting from the value of  $\eta$  obtained at  $B_0 = 0$  (which increases with pressure, see again figure 9.1), the power transfer efficiency steeply decreases to a minimum between 2.5 mT and 3 mT. At this minimum, the efficiency is globally below 50 % for both  $D_2$  and  $H_2$ , which further decreases especially at low pressure: at 0.3 Pa in hydrogen, no stable discharge operation is possible in the B-field region of the minimum at an RF power of 1 kW.

Applying magnetic fields higher than 3 mT is accompanied by a gradual increase of  $\eta$  until a maximum between 8 mT and 10 mT is reached. This increase is particularly strong at low pressures. Whereas at 1 Pa the efficiency reaches up to values comparable to the initial values at  $B_0 = 0$ , the maxima of  $\eta$  at 0.5 Pa and especially at 0.3 Pa well exceed the power transfer efficiency of the field-free case. For deuterium, this leads to RF power transfer efficiencies in the range between 60 % and 65 %, displaying only a weak increase with increasing pressure.

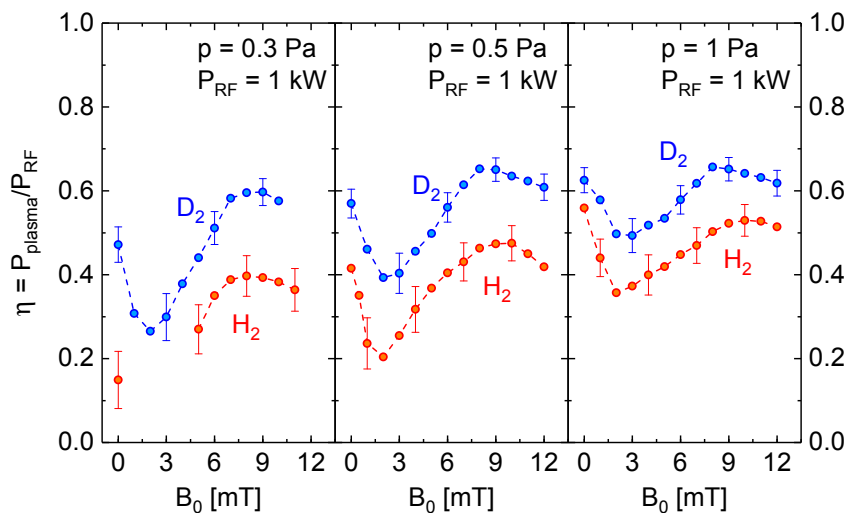


**Figure 9.3:** RF power transfer efficiency of discharges in  $H_2$  and  $D_2$  generated by the Nagoya antenna at varying magnetic fields. Presented are measurements obtained at an RF power of 1 kW and pressures of 0.3, 0.5 and 1 Pa, respectively.

In analogy to the measurements applying the helical coil, the observed variation of the RF power transfer efficiency is almost exclusively caused by a changing plasma resistance, as the loss resistance remains virtually constant at a value of  $0.12\ \Omega$  for all pressures and magnetic fields applied. Accordingly, the plasma resistance  $R_{\text{plasma}}$  displays an identical relative behaviour as the RF power transfer efficiency presented in figure 9.3, while its absolute value varies between  $0.05\ \Omega$  and  $0.23\ \Omega$ .

At low magnetic fields of  $B_0 < 3\ \text{mT}$ , the behaviour of  $\eta$  resembles the observations made with the helical coil in chapter 8.4: Starting from a purely inductive mode at  $0\ \text{mT}$ , the application of a magnetic field leads to the magnetization of charged particles, which reduces their perpendicular mobility and hinders inductive heating. Consequently, the RF power transfer efficiency decreases.

However, the subsequent increase of the power absorption at higher magnetic fields and the occurrence of the local maximum around  $8\ \text{mT}$  do not correspond to the characteristics of ICPs. This indicates that the discharge performs a mode transition to a wave-heated regime. In order to assess this observation in further detail, both the plasma parameters of the generated discharges and the particular influence of the magnetic field on the plasma transport have to be discussed first.

### 9.2.2 Relative spatial plasma profiles

The relatively low RF power transfer efficiency in hydrogen - particularly at low pressure and low magnetic fields - leads to some practical limitations due to the higher ohmic losses and the correspondingly higher heat loads (generally discussed in chapter 6.2). To overcome these limitations, most of the investigations presented in the following have been conducted in deuterium, where the situation is less critical. Selected results obtained in hydrogen are exemplarily included for a comparison, when required.

#### Axial profiles of the electron density

An example for the typical influence of the magnetic field on the axial electron distribution is provided in figure 9.4. It shows the axial profiles of the electron density in  $\text{D}_2$  at magnetic fields of  $0\ \text{mT}$ ,  $3\ \text{mT}$  and  $8\ \text{mT}$  and at a fixed pressure of  $1\ \text{Pa}$ . The profiles are normalized with respect to their maximum value, which is located at the vessel center. The profiles remain axially symmetric also in the presence of a magnetic field, which has been checked by inserting the probe from

the opposite direction. If  $B_0$  is increased, a monotonic broadening of the profiles is observed, significantly exceeding the measurement uncertainty. At 8 mT and a position of  $z = 100$  mm for example,  $n_e$  only weakly decreases to about 80 % of its peak value, while it drops down to 40 % at the same position if no field is applied. In general, an analogous behaviour is observed also in hydrogen and for lower pressures.

One reason for the observed broadening of the profiles is the reduced radial diffusion of charged particles with increasing magnetic field. Since the plasma transport parallel to the magnetic field lines remains unchanged, an increasing fraction of charged particles diffuse towards the axial ends of the vessel, effectively broadening the axial plasma distribution. This behaviour is accompanied by a significant increase of the absolute densities, which is further assessed in the following section 9.2.3.

### Lateral intensity profiles

Exemplarily, the lateral intensity profiles of the atomic  $D_\beta$  emission line of deuterium with and without the application of an external magnetic field of 8 mT are presented in figure 9.5. Depicted are measurements obtained at a pressure of 0.5 Pa. The profiles in the upper graph are measured at the discharge (and antenna) center ( $z = 200$  mm), while the ones in the lower graph are taken at an axial position of  $z = 90$  mm. At the central position, the intensity profile is observed to be slightly broader at 0 mT than at 8 mT. At  $z = 90$  mm, this difference is strongly reduced and the obtained profiles are almost identical. The small local deviation of the profiles at the center is caused by the geometry of the Nagoya antenna. At 0 mT, the purely inductive heating of the plasma occurs localized close to the upper horizontal leg and the lower end legs of the antenna (see illustration at the top of figure 9.5). Consequently, the spatial heating regime is not ideally cylindrically symmetric and a higher intensity is emitted close to the antenna legs during inductive operation.

In summary, the influence of the magnetic field on the relative lateral intensity profiles appears to be generally weak in the considered range of the magnetic field. An analogously weak effect of  $B_0$  is observed at 0.3 and 1 Pa as well as for hydrogen discharges. In fact, the intensity profiles obtained at  $z = 90$  mm with the Nagoya antenna are virtually identical to those obtained with the helical coil at the same  $z$ -position, which were presented in the sections 7.2.1 and 8.2.1. This indicates that the relative radial distribution of the plasma parameters  $n_e$  and  $T_e$

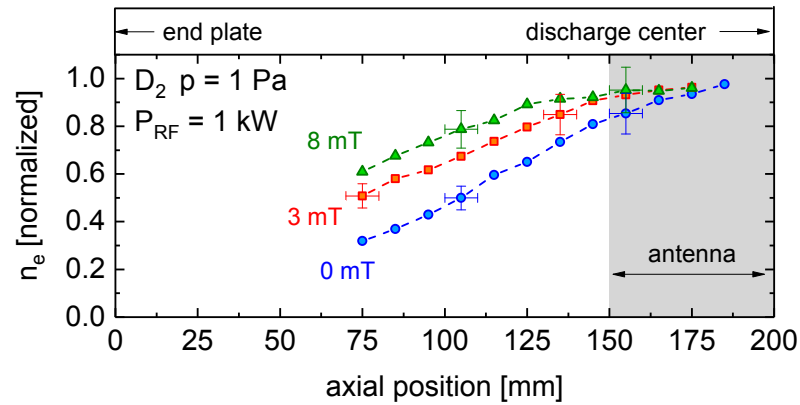


**Figure 9.4:** Normalized axial profiles of the electron density in deuterium at a fixed pressure of 1 Pa for different magnetic fields.

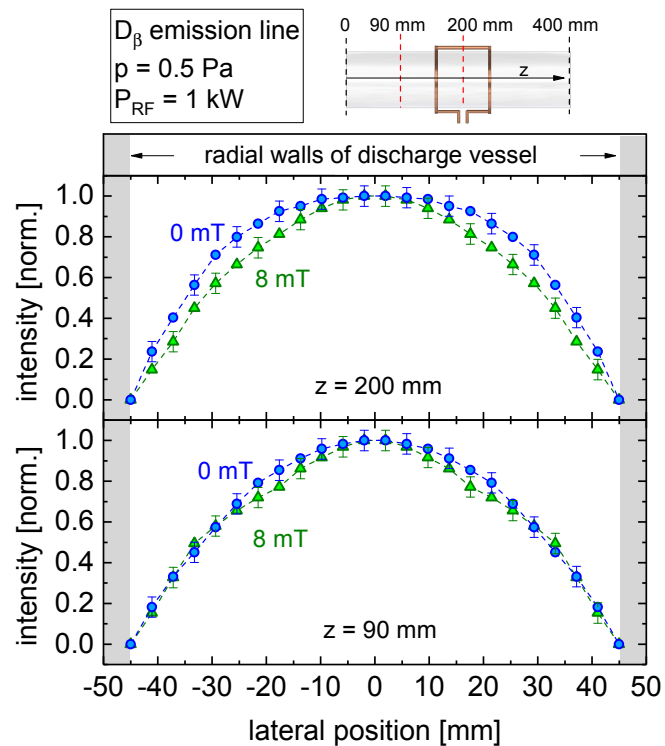


**Figure 9.5:** Examples of the normalized lateral intensity profiles of the  $D_\beta$  emission line, measured in deuterium discharges at a pressure of 0.5 Pa and a RF power of 1 kW. Depicted are profiles obtained at two different axial positions for  $B_0 = 0$  mT and  $B_0 = 8$  mT, respectively.

- which dominate the measured emission via electron impact excitation - does not change significantly in the presence of the applied magnetic fields even though the radial ambipolar diffusion is expected to be altered. This observation is considered as an indication for a changed plasma heating mechanism, an issue which is taken up again and discussed later in section 9.2.4. However, the comparison of axially averaged plasma parameters obtained at different magnetic fields remains the appropriate measure to characterize the discharges globally due to this behaviour.

### 9.2.3 Plasma parameters at varying pressure and magnetic field

The variation of the RF power absorption depending on the applied magnetic field is most pronounced between 0 and 10 mT. Accordingly, the behaviour of the plasma parameters  $n_e$  and  $T_e$  is investigated in detail in this range.

Figure 9.6 (a) shows the axially averaged electron density measured by the floating double probe at varying  $B_0$  and different pressures in deuterium. At 0 mT,  $n_e$  increases with pressure, from  $2 \times 10^{17} \text{ m}^{-3}$  at 0.3 Pa to approximately  $4 \times 10^{17} \text{ m}^{-3}$  at 1 Pa. Again, this reflects the characteristic behaviour of inductively coupled plasmas at the present parameters. Increasing the magnetic field from 0 to 8 mT leads to a steep and monotonous increase of  $n_e$  for all considered pressures. From 8 to 10 mT, this increase is weakened and the density saturates at a value of about  $8 \times 10^{17} \text{ m}^{-3}$ , virtually independent of the pressure. Compared to the case of 0 mT, the applied magnetic field consequently induces a significant enhancement of the electron density, which is stronger pronounced at lower pressure. At 0.3 Pa,  $n_e$  is increased approximately by a factor of 4, while it is roughly doubled at 1 Pa. In hydrogen, a similar enhancement is observed. However, the absolute densities in  $\text{H}_2$  are systematically between 1.5 and 2 times lower than in deuterium, in consistency with the measured power transfer efficiency.

If the behaviour of  $n_e$  is compared to the dependence of the RF power transfer efficiency presented in figure 9.3, significant differences are observed. In general,  $n_e$  is apparently no longer proportional to the absorbed power  $P_{\text{plasma}}$  if the magnetic field is varied simultaneously: for once, the monotonically increasing electron density does not exhibit a minimum around 3 mT, in contrast to  $\eta$ . A further deviation is found if the discharges at 0 mT are compared to those generated at fields of 8 mT and higher. At 1 Pa for example, about 650 W are deposited in the plasma both at 0 and 8 mT, whereas the density increases by a factor

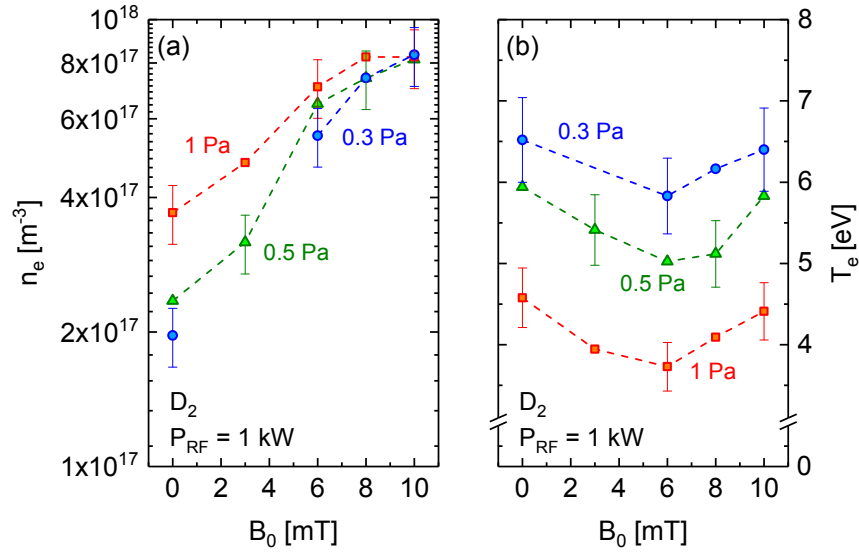


**Figure 9.6:** Electron density (a) and electron temperature (b) in deuterium at varying magnetic field and different pressures for a fixed RF power of 1 kW.

of two. To discuss this seemingly contradictory behaviour, the influence of the magnetic field on the ion diffusion has to be considered. For such an assessment, the corresponding electron temperatures of the discharges have to be taken into account first.

In figure 9.6 (b), the measured electron temperatures at varying magnetic field are depicted. Generally, the typical increase of  $T_e$  with decreasing pressure is observed: At 1 Pa, it is in the range of 4 eV, increasing to about 5.5 eV at 0.5 Pa and to roughly 6 eV at 0.3 Pa. Depending on the magnetic field, the same relative trend is observed at all pressures: in the range from 0 to 6 mT, the electron temperature decreases slightly by about 0.8 eV until a minimum is reached. If the magnetic field is increased further,  $T_e$  is again enhanced, roughly by same amount of the prior decrease. As a result,  $T_e$  is virtually equal at 0 mT and 10 mT. The same behaviour is observed in hydrogen discharges.

### Influence of the magnetic field on the ionization and power balance

The measured electron densities and temperatures can be discussed if the impact of the magnetic field on the ionization and power balance is assessed. As described in chapter 3.5, the application of a magnetic field reduces the ambipolar diffusion perpendicular to the magnetic field. Based on the equations (3.30) and (3.42), the ion confinement time  $\tau_{\text{ion}}$  in the presence of a magnetic field is calculated. As

already described in section 3.4, the evaluation of ion confinement times assuming solely ambipolar diffusion is an approximation at pressures below 1 Pa, since the ion transport in the free fall regime is neglected. The following simplified evaluation is therefore capable to illustrate the observed dependencies of  $n_e$  and  $T_e$  qualitatively, but insufficient for a quantitative assessment.

Figure 9.7 (a) shows the values of  $\tau_{\text{ion}}$  obtained by this approach at varying magnetic field. For all three pressures, the same relative trend is observed: between 0 and 6 mT, the confinement time steeply increases. Above 6 mT,  $\tau_{\text{ion}}$  only weakly increases further at 1 Pa and is almost constant at lower pressures. This saturation is caused by the anisotropy of the ambipolar diffusion: due to the magnetic field, the perpendicular diffusion is strongly reduced until around 6 mT. At higher fields, the total confinement time is increasingly dominated by the axial diffusion, which is not influenced by  $B_0$ . With rising pressure, the confinement times generally increase due to a higher collision frequency of charged particles resulting in a shorter mean free path.

In view of the ionization balance introduced in equation (3.33), the particular impact of  $\tau_{\text{ion}}$  on the electron temperature is assessed in a first step. Generally,  $T_e$  is anticipated to be inversely dependent on the ion confinement time. Regarding the behaviour at varying pressure, a good agreement with this expectation is observed: while  $\tau_{\text{ion}}$  increases at higher pressure,  $T_e$  is found to decrease. In addition, the strong increase of the confinement time between 0 and 6 mT corresponds well to the observed decrease of  $T_e$  in this region of the magnetic field. However, the magnitudes of the pressure and magnetically induced enhancements of the confinement times do not correspond to the observed differences of  $T_e$  quantitatively: according to  $\tau_{\text{ion}}$ , a much stronger reduction of  $T_e$  due to the magnetic would be expected. This is contributed to the limited quantitative applicability of ambipolar diffusion in this regime. In addition, the subsequent increase of  $T_e$  at higher fields is not reflected within the confinement times. Phenomenologically, it indicates the onset of wave heating, which will be discussed in the next chapter.

In order to evaluate the qualitative influence of the magnetic field on the electron density, the power balance of the generated discharges is discussed in the next step. Since the electron temperature exhibits a relatively weak variation in the considered range of the magnetic field, the approximation introduced in equation (3.39) is applied. Assuming a fixed plasma volume  $V_{\text{plasma}}$  given by the geometry of the discharge vessel, a proportionality of the electron density to the product of the absorbed power  $P_{\text{plasma}}$  and the ion confinement time is

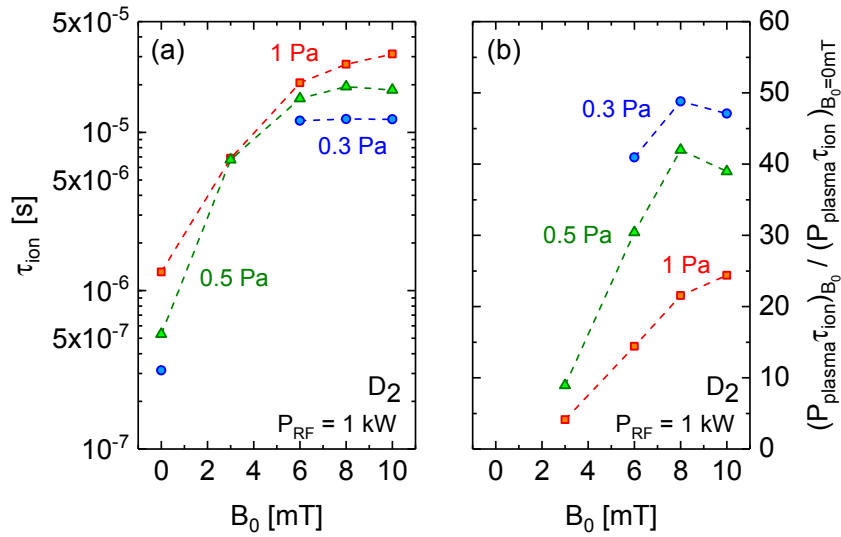


**Figure 9.7:** (a) Ion confinement time  $\tau_{ion}$  in deuterium depending on the applied magnetic field at different pressures. (a) Product of  $\tau_{ion}$  and the absorbed RF power  $P_{plasma}$  at varying magnetic field and different pressure, normalized to the value of  $P_{plasma} \tau_{ion}$  at  $B_0 = 0$  mT.

expected. Accordingly, the product  $P_{plasma} \tau_{ion}$  is calculated based on the measured data at varying magnetic field. At each pressure,  $P_{plasma} \tau_{ion}$  is normalized to its corresponding value obtained at  $B_0 = 0$  mT, in order to highlight the influence of  $B_0$ . Figure 9.7 (b) shows the result of this evaluation. For all pressures, a significant increase of  $P_{plasma} \tau_{ion}$  is observed with increasing magnetic field, mainly due to the rising confinement times. At lower pressures, the displayed increase is more pronounced.

Qualitatively, this behaviour is in good agreement with the observed dependencies of the electron density: both  $P_{plasma} \tau_{ion}$  and  $n_e$  exhibit a significant enhancement with increasing magnetic field, which is more pronounced at lower pressure. Consequently, the behaviour of  $n_e$  can be explained by reassessing the characteristics of ion diffusion in a magnetic field introduced in chapter 3.4:

- If a magnetic field is applied, the perpendicular diffusion of charged particles is reduced. On the one hand, this causes the broadening of the axial  $n_e$  profiles presented in chapter 9.2.2. On the other hand, the confinement time of ions increases globally and thus, the loss rate of ions to the wall is reduced. If the power input  $P_{plasma}$  simultaneously remains sufficiently high for the sustainment of the ionization process, the electron density in equilibrium rises.

- In a magnetized discharge, the diffusion of charged particles perpendicular to the magnetic field lines is only possible via collisions. If the pressure is decreased, the neutral particle density decreases. Consequently, collisions of charged particles with neutrals are less probable and the perpendicular diffusion is effectively hindered. This leads to a higher confinement time and thus, to a slower ion loss rate. Consequently, the enhancement of  $n_e$  due to a magnetic confinement is more pronounced at lower pressures.

In summary, the influence of the magnetic field on the ion diffusion qualitatively explains the initially described, seemingly contradictory behaviour of  $n_e$ . At  $B_0 \geq 8$  mT a higher electron density than at 0 mT is observed due to the slower ion loss rate, even though the absorbed RF power is virtually equal. Due to the decreasing collision rates, this correlation appears to be stronger at lower pressure.

However, the quantitative comparison of the magnetically induced enhancement of  $P_{\text{plasma}}\tau_{\text{ion}}$  with the measured increase of the electron density exhibits a significant deviation. The calculated values of  $P_{\text{plasma}}\tau_{\text{ion}}$  display an increase which is roughly ten times higher as the increase of  $n_e$ . Hence, the relative enhancement of  $P_{\text{plasma}}\tau_{\text{ion}}$  due to the magnetic field appears to be overestimated. This is attributed to the strong simplification that solely ambipolar diffusion is assumed for the calculation of  $\tau_{\text{ion}}$ . As already discussed in section 3.4, at the present parameters a simultaneous evaluation of the influence of the magnetic field on the free fall ion transport would be required, which is not feasible in a 0-dimensional picture. Such an analysis requires the application of numerical methods which are capable of resolving this problem spatially.

If an analogous evaluation is conducted for hydrogen discharges, the same characteristic dependencies are obtained. However, there is a weak isotopic difference, as the relative enhancement of  $n_e$  with increasing magnetic field is found to be slightly but systematically higher in hydrogen. Compared to the results in  $D_2$ , the increase of the electron density from 0 mT to 10 mT is roughly 25 % steeper in hydrogen.

### 9.2.4 RF heating by propagating waves

The considered effects of a static magnetic field on the movement of charged particles provide a conclusive description of many characteristics of the discharges generated by the Nagoya antenna, at least qualitatively. However, the measured increase of the RF power transfer efficiency at magnetic fields exceeding 3 mT and

the occurrence of a local maximum between 8 mT and 10 mT indicate a transition of the discharges from an inductively driven to a wave heated discharge. For a dedicated assessment of the heating scheme in this regime, the characteristics of helicon and TG wave modes at the present parameters are evaluated. In contrast to the inductive heating mechanism, not all mechanisms of the excitation, propagation and damping of these waves in the low field regime are fully understood up to now. As explained in section 4.3, no simplified analytical description of the heating scheme has yet been developed and the following discussions are therefore limited to a mostly phenomenological treatment.

### Boundary conditions for the propagation of helicon and TG waves

At first, the requirements for the propagation of helicon and Trievelpiece-Gould waves are assessed based on the boundary conditions presented in chapter 4.3.1. Therefore, the minimum and maximum densities relevant for the investigated discharges are estimated according to the equations (4.20) and (4.19). The axial length  $L_c$  is assumed to correspond to the discharge cylinder length of 0.4 m. Since the actual damping of waves is neglected in the deduction of  $n_{\min}(l)$  and  $n_{\max}(l)$ , these expressions have to be considered as approximations.

In figure 9.8 (a), the maximum densities  $n_{\max}(l)$  for the first four longitudinal wave modes  $l = 1..4$  at varying magnetic field are indicated by the grey parabolas. Additionally, the measured electron densities of the deuterium discharges discussed in the previous chapter are included as a reference. As deduced in chapter 4.3.1,  $n_e < n_{\max}(l)$  is a necessary condition for both helicon and TG wave propagation. Comparing the measured electron densities and the maximum densities yields that the number of longitudinal modes which are able to propagate quickly increases with increasing magnetic field. At low fields, there is still a restriction, since the condition for a propagation of the  $l = 1$  waves is not yet fulfilled. At magnetic fields of at least 6 mT, the imposed boundary condition is fulfilled for all longitudinal wave numbers and all applied pressures. Consequently, the propagation of TG waves is possible without restrictions in this regime, since  $n_e < n_{\max}(l)$  is the only boundary condition to be regarded.

For a propagation of helicon waves however,  $n_e > n_{\min}(l)$  has to be fulfilled in addition. This boundary condition is analogously illustrated in figure 9.8 (b) by the grey straight lines. Again, the first four longitudinal wave modes are included. In this case, the requirement to be fulfilled appears to be much stricter. Globally, the achieved densities fulfil only the condition for a propagation of the first two

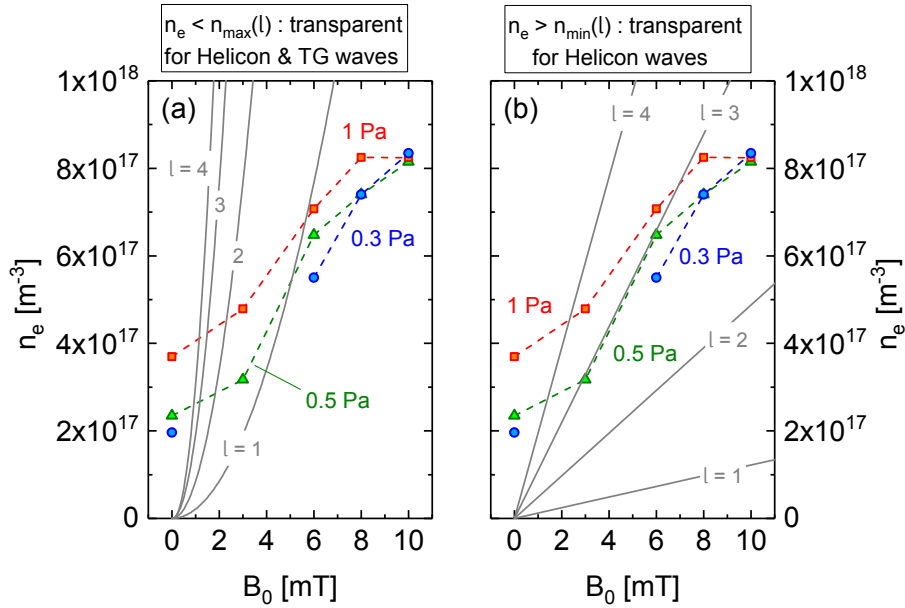


**Figure 9.8:** Illustration of the boundary conditions for the propagation of helicon and TG wave modes in deuterium discharges. Depicted are the maximum (a) and minimum (b) densities of the first four longitudinal modes depending on the applied magnetic field. Respectively, the measured electron densities at different pressures are included for a reference.

modes  $n_e > n_{\min}(1, 2)$ . Only in an intermediate region between 2 and 6 mT, the requirement for the  $l = 3$  mode is partly reached. Particularly at higher fields of  $B_0 \geq 8$  mT however, the observed increase of the density appears to be insufficient to maintain the conditions for a propagation of higher helicon modes.

To summarize, the parameters of the presently investigated discharges allow for a propagation of both helicon and TG waves in general. The number of longitudinal wave modes that fulfil the requirements for propagations increases with increasing magnetic field. If the magnetic field is sufficiently large, TG modes can propagate without limitation. However, the number of propagating helicon modes is restricted to the first few longitudinal modes and is further reduced at higher fields. If the same analysis is conducted for hydrogen discharges, a corresponding behaviour is again observed.

### Influence of helicon and TG waves on the RF power absorption

In view of these results, several characteristics of the investigated discharges which have already been attributed to the excitation of wave modes can now be reassessed.

- At first, the dependence of the **RF power transfer efficiency** on the magnetic field is discussed, which is presented in section 9.2.1. In the magnetic field regime between 3 mT and 8 mT, where the number of propagating TG and helicon wave modes increases,  $\eta$  is steeply rising as well. This correlation strongly indicates that the observed increase of the efficiency is contributed to the gradual onset of wave heating. Furthermore, the occurrence of the local maximum around 8 to 10 mT can also be qualitatively described. First, the number of TG wave modes does not increase anymore at higher fields, which already indicates that a saturation of the RF power absorption may be expected. In addition, the electron density is not increasing steeply enough at higher fields in order to maintain the requirements for the propagation of higher helicon modes. Eventually, this reduces the number of wave modes to be excited and results in the observed slow decrease of the RF power transfer efficiency at higher fields. As already introduced in section 4.3, the occurrence of such a local maximum of the power absorption depending on the magnetic field is a characteristic feature of many low field helicon discharges and, as introduced in section 4.3.2, commonly referred to as a *low field peak*.
- Since helicons are only weakly damped at the present parameters, most of the actual RF heating is considered to be carried by the highly damped TG waves. As deduced in section 4.3, those modes deposit RF power mainly at the radial plasma boundaries due to their fast decay. The assumption of a dominant role of the TG waves regarding the RF power deposition therefore correlates with the observed **lateral intensity profiles** of the generated discharges. As presented in chapter 9.2.2, there is no indication of a strong change of the radial distribution of the plasma parameters when the discharge transfers from an inductive to wave-assisted mode. This implies that region where plasma heating and ionization dominantly take place remains comparable: in both cases the heating occurs at the plasma boundaries close to the vessel walls. In case of ICPs due to the induced electric fields in the RF skin depth, in case of the wave heated discharges due to the damping of TG waves.
- The observed slight increase of the **electron temperature** at magnetic fields above 6 mT presented in figure 9.6 (b) appears to be correlated with the onset of wave heating as well. However, the magnitude of this increase is

relatively weak and only slightly exceeds the measurement error. In addition,  $T_e$  is simultaneously affected by the magnetic field due to the changed diffusion, as already discussed in section 9.2.3. Since the available data does not allow for a clear distinction between the latter and the possible influence of wave heating, this work refrains from a further dedicated assessment. However, comparable relative dependences of  $T_e$  have also been seen in other helicon discharges operated in hydrogen in the low field regime [SMO<sup>+</sup>15].

In conclusion, many of the observed properties of the investigated discharges are convincingly described if the characteristic features of helicon and TG waves are taken into account. This demonstrates that the discharges generated by the applied Nagoya antenna perform a transition to a wave heated mode if a static magnetic field is applied. In course of this mode transition, a relatively moderate increase of the RF power transfer efficiency can be achieved compared to the inductive mode at 0 mT. However, the simultaneous enhancement of the electron density due to increased radial confinement of the plasma is quite substantial. In the overall picture, the possibility to reach high plasma densities via wave heated discharges is apparently not caused by a significantly high RF power transfer efficiency. It is rather originating in their unique capability to provide enough RF power for maintaining a sufficiently high ionization rate within an axially magnetized low pressure plasma, an ability which helical ICPs lack, as described in chapter 8.4.

### 9.2.5 Atomic density and dissociation balance

As discussed in chapter 2.1, a crucial quantity for the surface production of negative hydrogen ions in an ion source is the density of hydrogen atoms. In analogy to the investigations conducted with the helical coil, the density ratio of atoms and molecules is assessed for the discharges generated by the Nagoya antenna. Both hydrogen and deuterium are investigated, since the dissociation process exhibits significant isotopic differences, as introduced in section 3.3 and already observed for ICPs.

Figure 9.9 shows the measured density ratios  $n_H/n_{H_2}$  in hydrogen (a) and  $n_D/n_{D_2}$  in deuterium (b) at varying magnetic field for a fixed RF power of 1 kW and different pressures. In hydrogen, the available data is limited due to the lower RF efficiency, preventing stable discharge operation at low pressure and low magnetic fields. The case of 0.3 Pa can therefore only be assessed in detail for

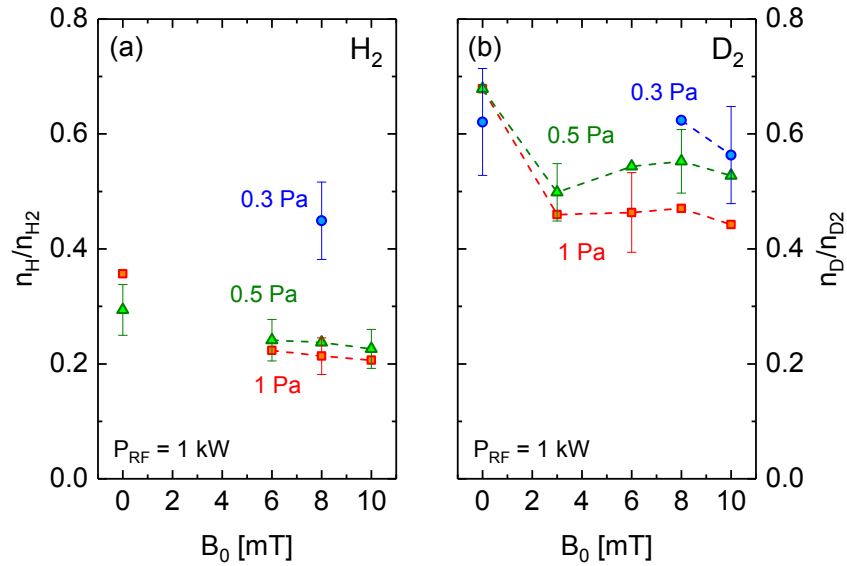


**Figure 9.9:** Density ratio of atoms and molecules at varying magnetic field and different pressure in hydrogen (a) and deuterium (b).

deuterium. In general, the characteristic deviation of hydrogen and deuterium is well observed: the density ratio in  $D_2$  (between 0.4 and 0.65) exceeds the values obtained in  $H_2$  at the same operational parameters roughly by a factor of two. Applying a magnetic field leads to a similar behaviour for both isotopes. At 0.5 and 1 Pa, increasing  $B_0$  is accompanied by a decrease of the density ratio. Between 3 and 10 mT, the density ratios display no significant changes and remain approximately constant. At 0.3 Pa in  $D_2$ , the ratio is around 0.6 at all field strengths and only a small decrease within the error bars at 10 mT occurs. In summary, a decrease of the density ratio with increasing magnetic field is generally observed, which is pronounced stronger at higher pressure. In the presence of a magnetic field,  $n_H/n_{H_2}$  and  $n_D/n_{D_2}$  systematically increase with decreasing pressure.

In order to assess these results further, the production and loss processes of hydrogen atoms introduced in chapter 3.3 have to be considered. Due to the lack of reliable data regarding the surface recombination of deuterium atoms, mainly hydrogen is treated exemplarily in the following. In a first step, only the production of atoms via electron impact dissociation in the plasma volume is considered. The effective dissociation rate  $r_{\text{diss}} = n_0 n_e X_{\text{diss}}(T_e)$  is estimated in figure 9.10 (a) based on the measured plasma parameters. Both at 0.5 Pa and 1 Pa, the dissociation rate increases with increasing magnetic field, due to its

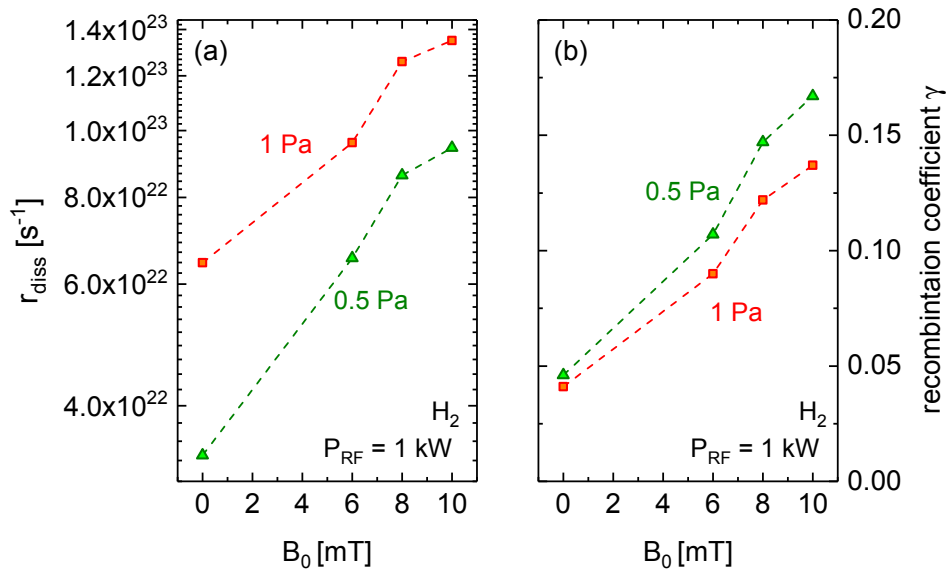


**Figure 9.10:** (a) Rate of the electron impact dissociation of hydrogen molecules at varying magnetic field in hydrogen. (b) Effective recombination coefficient required to match the measured values of  $n_H/n_{H_2}$  at varying magnetic field according to the dissociation balance.

proportionality to the electron density. Accordingly, a corresponding increase of the ratio  $n_H/n_{H_2}$  could be expected. This is obviously not the case, which implies that the loss rate of atoms has to change as well, according to the dissociation balance introduced in chapter 3.4.

The loss rate  $r_{diff,H}$  of atoms due to wall recombination depends inversely on the confinement time  $\tau_H$  of atoms within the plasma. However, the evaluation of  $\tau_H$  according to equation (3.25) yields that none of the known or measurable parameters (e.g.  $T_{gas}$ ,  $\lambda_H$ ) exhibits a dependence on the applied magnetic field - as expected, since magnetic fields do not affect the motion of neutrals. As a consequence, the only remaining parameter capable of changing the confinement time of atoms in the discharge is the recombination coefficient  $\gamma$ . Since the actual recombination coefficient at the walls of the experiment is unknown,  $\gamma$  can be treated as a free parameter. By its variation, the dissociation balance provided in equation (3.29) can be resolved in order to fit the measured values of  $n_H/n_{H_2}$ ,  $n_e$  and  $T_e$  simultaneously. The values of  $\gamma$  obtained by this approach are shown in figure 9.10 (b) at varying magnetic field. For both 0.5 and 1 Pa, the evaluated recombination coefficient at 0 mT is about 0.045. Applying a magnetic field leads to a significant increase of  $\gamma$  to about 0.15, while a slightly higher value is required

at 0.5 Pa than at 1 Pa. In conclusion, the recombination rate of hydrogen atoms at the walls is expected to rise significantly if a magnetic field is applied.

The obtained result can be evaluated in view of the literature values summarized in table 3.1. With respect to the applied discharge vessel, quartz surfaces are regarded first: the value of 0.045 obtained at 0 mT is well comparable to the value estimated for the ICPs in chapter 8.3 and located at the upper limit of the typically reported range for this material. This appears to be reasonable, especially if the axial ends of the vessel are included in the consideration. On one side of the cylindrical chamber, a partially metallic transition piece is mounted, on the other side the stainless steel expansion chamber is located. In consequence, hydrogen atoms which arrive at the ends of the quartz cylinder are likely to either hit a metallic surface ( $\gamma > 0.1$ ) or to be entirely lost within the vacuum system ( $\gamma = 1$ ). Hence, the recombination coefficient evaluated by the present 0-dimensional approach has to be regarded as an effective value in general, expected to be found somewhere in between the typical values for quartz and metal. Apart from the magnetic field, no significant variation of the recombination coefficient with any other operational parameter (e.g.  $p$ ,  $P_{\text{RF}}$ ,  $\omega_{\text{RF}}$ ) is observed for both antennas.

However, the reason for the predicted increase of the *effective* recombination coefficient in the presence of a magnetic field cannot be explained based on the available data yet. A temperature induced increase of  $\gamma$  according to equation (3.21) can be ruled out, though: if the surface temperature of the discharge vessel is assumed to be in thermal equilibrium with the heavy particles of the plasma ( $\rightarrow T_{\text{gas}}$ ) in the present case, only a slight and almost negligible increase from 500 K to about 550 K is expected with increasing  $B_0$ , leading to a correspondingly small increase of  $\gamma$  which is insufficient to explain the behaviour illustrated in figure 9.10. In contrast, a changed ion flux on the vessel walls due to the applied magnetic field, potentially changing the surface properties, may be considered as a probable cause. For a further assessment of the observed behaviour, additional investigations exceeding the contents of this work are required. Such could for example include the application of other materials within the discharge chamber, allowing to identify whether the observed behaviour is a specific feature of a quartz surface.

### 9.3 Assessment of an application to RF driven ion sources

In analogy to the case of inductive plasma heating at varying excitation frequency discussed in chapter 8.3, the potential of low field wave heated discharges in view of an application at ion sources for NNBI in view of DEMO is assessed. Again, the dependencies of the crucial parameters  $\eta$ ,  $n_e (= n_{\text{ion}})$  and  $n_{\text{H}}/n_{\text{H}_2}$  on the supplied RF power at the relevant pressure of 0.3 Pa are specifically treated for both hydrogen and deuterium. In the present case, the magnetic field is kept constant at 8 mT. This value is chosen as it represents the local maximum of the RF power transfer efficiency at low pressure and  $P_{\text{RF}} = 1$  kW. The RF power is varied in a range between 0.8 and 1.5 kW. All results obtained with the Nagoya antenna are directly compared to the reference case of inductive heating at 1 MHz, which has already been discussed in chapter 8.3.

The **RF power transfer efficiency** at varying RF power is shown in figure 9.11 for both hydrogen (a) and deuterium (b). In wave heated hydrogen discharges, it increases weakly with increasing RF power, from  $\eta = 0.4$  at 0.8 kW to almost 0.5 at 1.5 kW. In the same power range in deuterium,  $\eta$  is virtually constant at a value of 0.6, exhibiting even a slight decrease within the error bars with increasing power. In direct comparison to the inductive discharges generated by the helical coil at 1 MHz, the efficiency of the discharges applying the Nagoya antenna are globally and quite significantly lower. As indicated especially by the results obtained in  $\text{D}_2$ ,  $\eta$  apparently saturates at a relatively low level. The power transfer efficiency of the wave heated discharges does therefore not exhibit the same increase with increasing power as observed for ICPs, which also slowly saturates yet at a considerably higher level. Since the plasma resistance does not further increase with power, a maximum of 60 % (in deuterium) and 50 % (in hydrogen) of the delivered power can be coupled to the plasma. The remaining fraction is lost due to ohmic heating in the RF system and the antenna, which implies that the Nagoya antenna requires more cooling to be reliably operated than the helical ICP coil at the same RF power.

Secondly, the behaviour of the **electron density** at varying power is assessed in figure 9.12. In order to highlight the influence of the RF power transfer efficiency, the density is plotted both versus the RF power delivered by the generator (full symbols) and versus the power  $P_{\text{plasma}}$  which is actually absorbed by the plasma (open symbols). Again, results obtained both in hydrogen (a) as well as in deuterium (b) are presented. In general, the electron density within the discharges

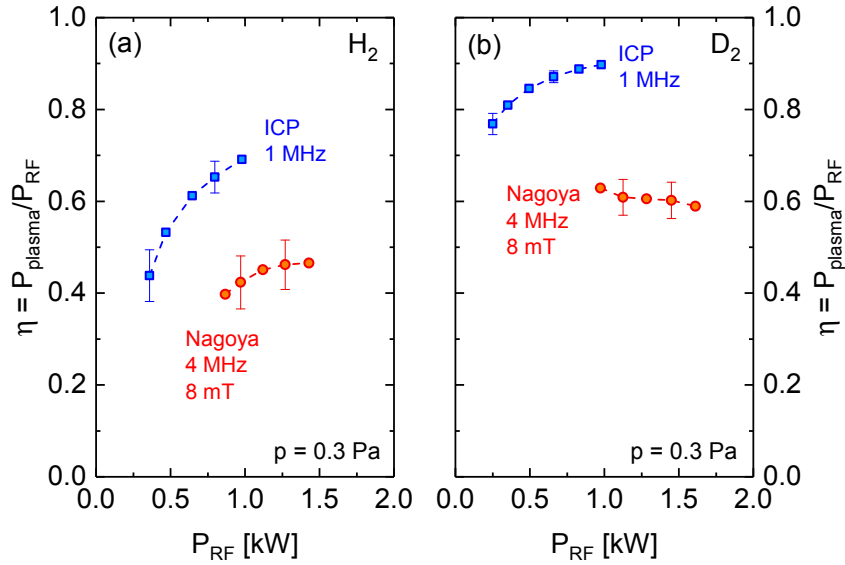


**Figure 9.11:** RF power transfer efficiency of (a) hydrogen and (b) deuterium discharges generated by the Nagoya antenna at varying RF power. For a comparison, the reference case of inductive heating at 1 MHz is included, respectively.

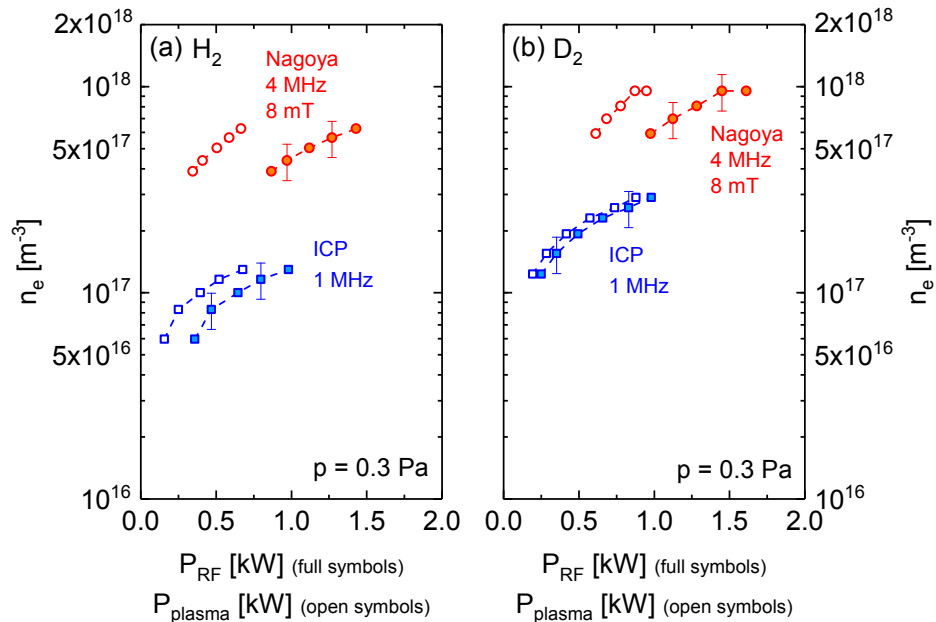


**Figure 9.12:** Electron density in (a) hydrogen and (b) deuterium discharges applying the Nagoya antenna at varying RF power  $P_{\text{RF}}$  (full symbols) and varying absorbed power  $P_{\text{plasma}}$  (open symbols). The reference case of inductive heating at 1 MHz is included for a comparison, respectively.

driven by the Nagoya antenna increases monotonically with increasing  $P_{\text{RF}}$  and  $P_{\text{plasma}}$ . Since the magnetic field (which dominates the ion losses) is kept constant, the expected proportionality of  $n_e$  on  $P_{\text{plasma}}$  according to the electron power balance can now be well observed. In hydrogen, the measured densities cover a range from  $4 \times 10^{17} \text{ m}^{-3}$  to approximately  $6 \times 10^{17} \text{ m}^{-3}$ . In comparison, the electron density in deuterium discharges is globally about 50 % higher.

If these results are directly compared with the included reference case of inductive heating at 1 MHz, the characteristics deduced in chapter 9.2.3 are again observed. At the same absorbed power  $P_{\text{plasma}}$ , the electron density in the magnetized, wave heated discharges is significantly enhanced: By a factor of 4 to 4.9 in  $\text{H}_2$  and by a factor of 2.5 to 3.3 in  $\text{D}_2$ . The difference between both discharge types is growing with  $P_{\text{plasma}}$ , due to a steeper increase of  $n_e$  observed with the Nagoya antenna compared to the ICP. This is caused by the higher ion confinement time in the presence of the magnetic field, as predicted by the electron power balance. Moreover, the increase of  $n_e$  is large enough to effectively overcompensate for the lower RF power transfer efficiency of Nagoya driven discharges: even for the same  $P_{\text{RF}}$  supplied by the generator, the density within the wave heated discharges remains considerably higher than for the ICP. At  $P_{\text{RF}} = 1 \text{ kW}$  for example, the

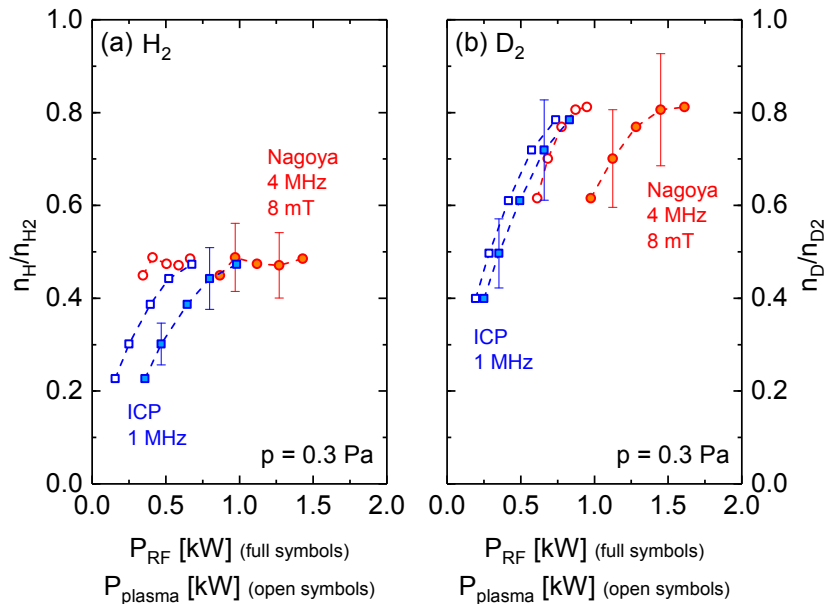


**Figure 9.13:** Atomic fractions  $n_{\text{H}}/n_{\text{H}_2}$  (a) and  $n_{\text{D}}/n_{\text{D}_2}$  (b) applying the Nagoya antenna at varying RF power  $P_{\text{RF}}$  (full symbols) and varying absorbed power  $P_{\text{plasma}}$  (open symbols). The reference case of inductive heating at 1 MHz is included for a comparison, respectively.

relative enhancement of  $n_e$  is of a factor of 3 in  $H_2$  and of a factor of 2 in  $D_2$ .

The last parameter to be addressed specifically is the **atomic fraction** within the generated discharges. Figure 9.13 shows the obtained values of  $n_H/n_{H_2}$  (a) and  $n_D/n_{D_2}$  (b) at varying RF power  $P_{RF}$  (full symbols) and at varying absorbed power  $P_{Plasma}$  (open symbols). In the wave heated hydrogen discharges, the density ratio is approximately constant at a value of 0.5. Within the measurement error, this is equal to what is measured for the ICP at the same  $P_{plasma}$ . The density ratio in deuterium is slightly increasing with the absorbed power from 0.6 to 0.8, which is again corresponding to the results obtained for the ICP at the same  $P_{plasma}$ . With respect to the actually supplied RF power  $P_{RF}$ ,  $n_H/n_{H_2}$  is hence observed to be virtually the same for both ICP and wave heated discharges. In deuterium, the density ratio  $n_D/n_{D_2}$  appears to be slightly lower for the discharges generated by the Nagoya antenna in comparison to the case of ICPs at the same  $P_{RF}$ . Therefore, the same characteristics of the atomic fraction as discussed in chapter 9.2.5 are observed also if the RF power is varied. Even though the electron density is significantly higher within the wave heated discharges (at the same  $T_e$ ), the atomic density remains on the same level as for the ICP or even decreases. Based on the presently available data, this behaviour can only be explained if the loss rate of atoms due to the wall recombination to molecules increases as well, as discussed in detail in the previous chapter. As a consequence, this result cannot be directly transferred to the scenario of larger ion sources up to now: due to the presence of the Faraday screen, the atom recombination processes at the driver walls of an ion source are severely changed compared to the present case, which has already been addressed in detail in section 8.3. The concluding discussion therefore focuses on the parameters  $n_e$  and  $\eta$ .

### Discussion and estimation of a potential power reduction

As indicated by these results, the most prominent improvement of wave heated discharges is the enhancement of the electron density compared to ICPs. In a final step, the obtained results are used to estimate the RF power which is required to sustain the same electron density with both discharge types. In addition, also the power losses corresponding to this scenario are approximated.

For the example of deuterium discharges, this is performed within figure 9.14 (a). Again, the obtained results of the electron densities with both the Nagoya antenna and the helical coil are plotted versus the provided RF power. The densities obtained with the ICP are linearly extrapolated, in order to estimate how much

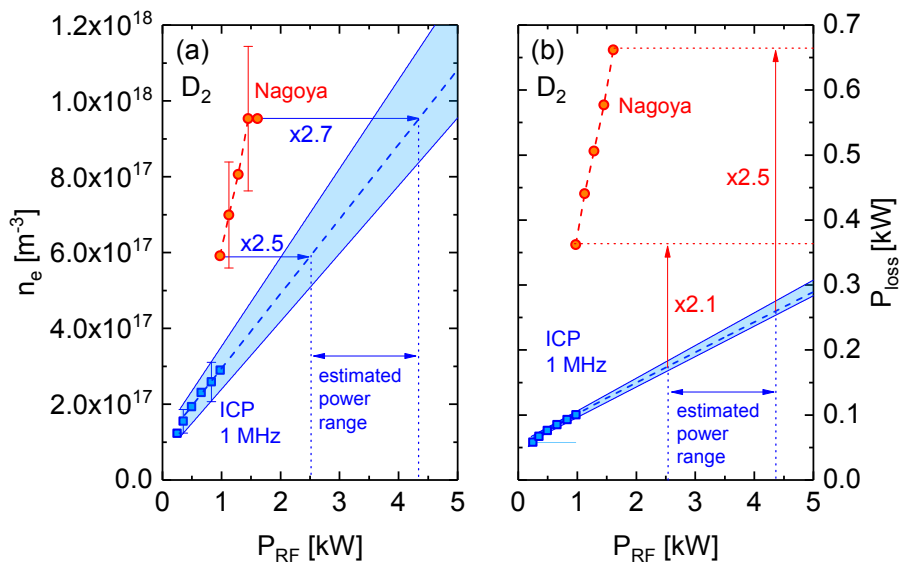


**Figure 9.14:** (a) Linear extrapolation of the electron density of ICPs at varying RF power in order to estimate the required  $P_{RF}$  to achieve the same  $n_e$  as measured with the Nagoya antenna. (b) Corresponding power losses of ICPs and wave heated discharges at varying RF power. The values of the inductively heated discharges are extrapolated to the power range obtained by the comparison in (a).

RF power might be required in this case to reach the same  $n_e$  as observed with the Nagoya antenna. A linear extrapolation of  $n_e(P_{RF})$  is a valid assumption according to the electron power balance and due the fact that  $\eta$  does not change significantly at higher powers. Obviously though, this approach remains a significant approximation that is afflicted by a high uncertainty, as indicated by the coloured area. Nevertheless, a rough power range can be estimated where the ICP is expected to achieve the same density level obtained with the Nagoya antenna. As illustrated by the vertical dotted lines, this range is roughly between 2.5 kW and 4.3 kW. Compared to the wave heated discharges, this corresponds to a significant relative increase of the required RF power of a factor between 2.5 and 2.7. If the same analysis is performed in hydrogen, an even higher factor of about 4 is obtained. In view of ion sources for NNBI, the investigated wave heated discharges therefore promise a significantly reduced RF power consumption.

On the other hand, the estimated power range can be used to analogously extrapolate the power losses  $P_{loss}$  to be expected for the ICP if such high electron densities are achieved. This estimation is visualized in figure 9.14 (b). For both discharge types, the measured power losses are displayed at varying RF power. The power losses of the ICP are extrapolated assuming a weak hyperbolic increase

of the RF power transfer efficiency, which yields an almost linear increase of  $P_{\text{loss}}$  with increasing RF power. In the power range between 2.5 kW and 4.3 kW (where the ICP is estimated to reach the same density as the wave heated discharge) the expected power losses are between 170 W and 250 W. Compared to that, the operation of the Nagoya antenna leads to losses which are between 2.1 and 2.5 times higher at the same achieved electron density. In hydrogen, a virtually equal dependence is observed, as the losses are increased for both discharge types due to the globally lower RF power transfer efficiency. Hence, the reduced overall power consumption of wave heated discharges comes at the price of higher losses due to ohmic heating within the RF circuit. Certainly, this requires for increased cooling measures and may thus negatively affect the reliability of the RF system.

In conclusion, the results presented in this work demonstrate that wave heated discharges are indeed a promising alternative to the presently applied inductive heating of an ion source plasma. Since considerably less RF power is required to reach high electron densities of almost  $10^{18} \text{ m}^{-3}$  in  $\text{H}_2/\text{D}_2$  discharges at 0.3 Pa, they entail the potential for a significantly reduced RF power consumption. Based on the performed fundamental studies - which allowed for the first time a direct and quantitative comparison with ICPs operated at 1 MHz in  $\text{H}_2/\text{D}_2$  - it is assessed that wave heated discharges qualify to be considered for further investigations. In course of these studies, the presently deduced potential drawback of increased power losses within the RF system needs to be re-evaluated in view of the required high reliability of ion sources for DEMO NNBI.

## **Outlook**

The fundamental studies within this work were specifically dedicated to the actual plasma heating regime, whereas a simplified and thus flexible laboratory setup was utilized. As already described before, the main differences of this experiment compared to an actual ion source are the different RF power density/the vessel diameter and the application of a Faraday screen. In consequence, future investigations will have to cover both aspects. While the effects of a Faraday screen on the wave heating mechanism and the wall recombination of atoms can still be studied at a (modified) laboratory setup in principle, the high power/high density operation has to be tested directly at a large and powerful ion source test bed.

In a further step towards assessing the potential of wave heated discharges, the plasma parameters and spatial distributions within the expansion region of an ion source will have to be investigated as well. The transient magnetic field of a potential wave-heated driver will influence the plasma transport towards the extraction region and will require an adaption of the magnetic filter field within the extraction region. First and fundamental investigations in this direction can also be performed at the CHARLIE experiment, due to the presence of an expansion chamber. Based on such investigations, valuable input for the next step, the envisaged application of wave heated discharges at an ion source test bed, can be gained.

## 10 Summary

For the NNBI systems at ITER, powerful RF driven ion sources operating low pressure H<sub>2</sub>/D<sub>2</sub> ICPs are required to fulfil the high demands posed on this important auxiliary heating method. In order to reach the required parameters at a filling pressure of 0.3 Pa and at an excitation frequency of 1 MHz, RF powers up to 100 kW per plasma driver have to be applied. This poses strong demands on the RF generators and circuits, requires for dedicated countermeasures and potentially limits the long term reliability of the ion source. In view of DEMO, the requirements towards the NNBI system are expected to be even higher, in order to ensure both a high wall-plug efficiency and a high general reliability. Particularly regarding the latter, a reduction of the RF power consumption of RF driven sources for NNBI is therefore highly desirable.

In order to reduce the required RF power while maintaining plasma conditions favourable for the production of negative ions, increasing the efficiency of the RF plasma generation is a promising approach. The main figures of merit of an efficient driver plasma can be summarized as follows: On the one hand, it has to provide a high positive ion density and a high density of atoms in view of the surface production mechanism of H<sup>-</sup>/D<sup>-</sup>. On the other hand, a high RF power transfer efficiency is desirable to ensure a high power absorption by the discharge in the first place and vice versa, a reduction of power losses within the RF system which might limit the source reliability. In this context, the potential of two alternatives to the currently applied ICPs driven at 1 MHz has been fundamentally assessed within this work for H<sub>2</sub> and D<sub>2</sub> discharges: ICPs driven at a higher excitation frequency than 1 MHz and wave-heated helicon discharges operated at low magnetic fields.

The investigations were conducted at a versatile laboratory experiment, where a cylindrical quartz tube with a diameter of 10 cm and a length of 40 cm serves as the discharge vessel. The experiment can be equipped with different antennas both for inductive and wave-heated helicon operation without changing the general discharge geometry. In the course of this work, a flexible RF circuit has been set

up, capable to achieve the required impedance matching with different antennas. It allows for H<sub>2</sub>/D<sub>2</sub> plasma operation at RF powers up to 2 kW at varying excitation frequency between 1 MHz and 4 MHz in the pressure range from 0.3 Pa to 10 Pa. Via a Helmholtz coil, static magnetic fields up to 12 mT oriented parallel to the cylinder axis can be applied. The setup has been equipped with a comprehensive set of diagnostic systems: based on current and voltage measurements within the RF circuit, the ohmic power losses during plasma operation can be determined. Vice versa, this allows to determine the RF power transfer efficiency of the generated discharges. The bulk plasma parameters are measured parallel and in a radial distance of one cm to the cylinder axis of the plasma vessel. The electron density, which is equal to the positive ion density due to quasineutrality, is measured both locally via a axially movable floating double probe and line of sight averaged via optical emission spectroscopy (OES). The latter also provides access to the electron temperature, the neutral gas temperature and to the ratio between the atomic and the molecular density, hence to the atomic fraction of the discharges.

At lower RF powers and smaller scale than typical for NNBI ion sources, this setup therefore allows to directly and quantitatively compare the introduced alternative plasma generation techniques with the baseline case of ICPs driven at 1 MHz, focusing on the main figures of merit of a driver plasma. This particular capability distinguishes the conducted investigations from other reported approaches aiming to increase the RF plasma generation efficiency of ion sources. The main aim of this work was to perform a first and fundamental assessment whether any of the proposed plasma generation methods may entail the potential to reduce the RF power consumption of H<sub>2</sub>/D<sub>2</sub> discharges in view of ion sources. In course of this evaluation, the fundamental characteristics of the different heating mechanisms at the present parameters had to be specifically analysed for both hydrogen and deuterium operation.

As they represent the reference case for the assessment of the alternative plasma generation methods, inductively heated discharges at 1 MHz utilizing a helical, five-turn coil were investigated in detail. At this driving frequency, the characteristics of the inductive heating mechanism of H<sub>2</sub> discharges in the pressure range from 0.3 Pa to 10 Pa were deduced.

In general, RF power deposition in an ICP occurs due to the induction of an RF plasma current leading to the collisional and collisionless heating of electrons within the RF skin depth. As it has been known from investigations conducted

in noble gases, the absorbed power within the discharge can be analytically approximated to be proportional to the effective plasma conductivity. The latter is in turn proportional to the electron density and depends furthermore on the collisionality, i.e. on the ratio of the effective electron collision frequency and the angular excitation frequency. If both frequencies are equal, the conductivity describes a maximum and hence, the power absorption by the plasma is enhanced.

Within this work, **it has been shown for the first time that this analytic approximation also provides a good description of the heating mechanisms within the investigated low pressure low temperature H<sub>2</sub>/D<sub>2</sub> ICPs.** This allowed to correlate the measured behaviour of the RF power transfer efficiency at varying pressure and RF power with the simultaneously measured plasma parameters: the RF power transfer efficiency generally increases with the applied RF power (varied in the range between 250 W and 800 W), since both the electron density (of the order of  $10^{17} \text{ m}^{-3}$ ) and the gas temperature (around 500 K) increase. The latter leads to a lower electron collision frequency due to a lower density of neutral particles. At the present parameters, a lower electron collision frequency results in a higher RF power absorption since the angular excitation frequency at 1 MHz is globally lower than the effective collision frequency of electrons. Vice versa, this implies that also a higher excitation frequency leads to a higher RF power transfer, assuming otherwise constant conditions. At varying pressure, the changing electron and neutral particle densities simultaneously influence the RF power transfer. As a result, a pronounced maximum of the measured RF power transfer efficiency at intermediate pressures between 1 Pa and 3 Pa is observed. In this region, typically more than 90 % of the provided power are absorbed by the plasma. At higher and lower pressure, the RF power transfer efficiency decreases significantly. At the ion source relevant pressure of 0.3 Pa and an intermediate RF power of 520 W, it is observed to be below 50 %.

Directly comparing hydrogen and deuterium ICPs driven at 1 MHz, **the particular role of atoms within the heating mechanisms of molecular low pressure discharges has been systematically deduced within this work for the first time.** The atoms H and D are more likely to be ionized in the present electron temperature region between 2 and 6 eV than the respective molecules, which results in higher electron densities if the atomic fraction is higher at otherwise comparable parameters. Since the molecular dissociation rate in deuterium is higher compared to hydrogen, also the atomic fraction and hence the electron density in deuterium discharges is globally higher: in D<sub>2</sub>, a density ratio between

atoms and molecules around 0.5 is typically measured, which is about two times higher than in H<sub>2</sub>. This induces a relative increase of the electron density in D<sub>2</sub> between 50 % and 100 % compared to H<sub>2</sub> at the same experimental conditions. As a consequence, also **the RF power transfer efficiency in deuterium is globally higher than in hydrogen**. The deduced correlation substantially contributes to the general understanding of the heating process within low pressure low temperature H<sub>2</sub>/D<sub>2</sub> discharges. It explains many isotopic differences empirically observed before, e.g. that deuterium discharges typically require less RF power to be ignited in the first place. Apart from this difference, the same relative behaviour of the RF power transfer efficiency and all considered plasma parameters is observed for both isotopes at varying operational parameters.

Applying 2 MHz and 4 MHz, the effect of a higher excitation frequency on inductively heated H<sub>2</sub>/D<sub>2</sub> discharges was investigated. In the considered range, **an increasing excitation frequency globally enhances the RF power absorption of the plasma**, as the difference between the electron collision frequency and the angular excitation frequency is globally reduced. In consequence, the measured RF power transfer efficiency increases monotonically with the excitation frequency at all considered pressures (between 0.3 Pa and 10 Pa) and RF powers (up to 1 kW). In addition, the position of the pressure dependent peak of the RF power transfer efficiency is shifted to about 5 Pa, where more than 95 % of the provided RF power are absorbed by the plasma for both isotopes - while it remains globally higher in deuterium compared to hydrogen. The improved power deposition at 4 MHz typically leads to a relative increase of the electron densities of about 50 % compared to 1 MHz at the same operational parameters. Consequently, also a slightly higher atomic fraction due to an increased rate of electron impact dissociation of molecules is achieved. Apart from its influence on the RF power transfer efficiency, the excitation frequency does not explicitly influence any other discharge parameters.

**At low RF power, the RF power transfer efficiency at 4 MHz is significantly enhanced at the ion source relevant pressure of 0.3 Pa**, since the difference between the effective electron collision frequency and the angular excitation frequency is small: the achieved efficiency of 85 % in H<sub>2</sub> at 520 W is a remarkable enhancement compared to the value around 50 % obtained at 1 MHz. In deuterium, a comparable yet slightly less pronounced effect is observed.

**At higher RF power, the frequency induced differences are gradually reduced:** due to the rising electron densities, the plasma is generally more capable

---

of absorbing the provided RF power and a variation of the excitation frequency by a few MHz eventually becomes irrelevant for both H<sub>2</sub> and D<sub>2</sub>. In other words, all considered excitation frequencies in the range from 1 MHz to 4 MHz are located sufficiently close to the collisionality maximum and hence, allow for a high RF power absorption at a high electron density. Applying frequencies much higher or even lower than those explicitly considered is not expected to entail any benefits regarding the RF power transfer efficiency either: a frequency well above or below the electron collision frequency will only result in reduced RF power absorption.

**In conclusion, applying a higher excitation frequency than 1 MHz in the high power regime of ion sources for NNBI does not entail the potential to decisively reduce the RF power consumption of ICPs.** In addition, a higher excitation frequency also implies that the RF voltage drop across the coil is higher. At high RF powers, this has to be considered as a disadvantage as well, as it increases the risk of electrical breakdowns and arcing between the coil windings, which needs to be avoided in view of a high source reliability. Based on the results obtained within this work, it is therefore suggested that a higher excitation frequency for ICPs can be ruled out as a promising alternative in view of ion sources for DEMO.

Beyond this, the systematic measurements conducted within this work generally provide a diverse experimental data set, characteristic for inductively heated low pressure hydrogen and deuterium discharges. Therefore, they have already proven to be ideally suited as valuable input for the benchmark of numerical codes which are dedicated to the simulation of such discharges.

Wave heated H<sub>2</sub>/D<sub>2</sub> discharges in the pressure range between 0.3 Pa and 1 Pa were investigated by operating a Nagoya type-III helicon antenna at low magnetic fields up to 12 mT at an excitation frequency of 4 MHz. At lower frequencies, no plasma ignition was possible due to the limited RF power.

In wave heated discharges, the plasma heating mechanism is fundamentally different compared to ICPs. Due to the applied static magnetic field, helicon and Trievelpiece-Gould (TG) waves can be excited to propagate. The subsequent damping of these waves leads to the deposition of power. However, many features of the plasma heating mechanism within low-field helicon discharges are not yet entirely understood. An analytical assessment of the power absorption mechanism analogous to the case of ICPs can therefore not be conducted and the

description of the heating processes is constrained to a mostly phenomenological approach. In addition, the discharge properties of wave heated discharges are severely influenced by the magnetic field, as it not only allows for the propagation of waves, but also changes the diffusion of charged particles within the plasma.

**If no magnetic field is applied, the Nagoya antenna is operated in a purely inductive mode**, which results in discharge parameters well comparable to the investigated ICPs. However, due to the low inductance of the Nagoya antenna of  $0.7 \mu\text{H}$ , the achieved RF power transfer efficiency is much lower (around 50 %) in comparison with the helical coil (inductance:  $2.4 \mu\text{H}$ ): in order to induce RF fields of the same magnitude with both antennas, a higher RF current is required with the Nagoya antenna leading to higher ohmic losses. If a very low axial magnetic field up to 3 mT is applied, the power deposition within the plasma is reduced and reaches a minimum around 20 – 30 %, since the magnetic field effectively hinders inductive heating.

**Applying magnetic fields above 3 mT, the desired transition to the wave heated mode has been achieved for both  $\text{H}_2$  and  $\text{D}_2$ .** This induces a rising RF power transfer efficiency in the region between 3 mT and 8 mT. This increase can be attributed to an increasing number of helicon and Trievelpiece-Gould (TG) wave modes which are excited and are able to propagate. The increased RF power deposition is considered to be primarily caused by a damping of excited TG waves, since the propagating axial helicon modes are only weakly damped at the present discharge conditions. At higher fields **between 8 and 10 mT, a local maximum of the RF power transfer efficiency up to 60 % is achieved, virtually independent of pressure.** This is a characteristic feature of low-field helicon discharges commonly referred to as a *low-field peak*.

Apart from its influence on the heating mechanism, **the applied magnetic field also leads to a radial plasma confinement:** due to the gyration of charged particles, the ambipolar diffusion of positive ions and electrons perpendicular to the magnetic field is strongly hindered. At applied magnetic fields above 3 mT, both the electrons and the positive ions are magnetized, i.e. their gyration radius is smaller than the vessel radius. This reduces the loss rate of charged particles towards the radial vessel walls, **which induces two changes with respect to the measured electron densities: a gradual broadening of the axial electron density profiles within the discharges and a global enhancement of the electron density.** The latter is particularly pronounced at lower pressure: for the example of deuterium at 0.3 Pa, the electron density

is increased roughly by factor of 4 from 0 to 8 mT, where it reaches a value of  $8 \times 10^{17} \text{ m}^{-3}$ . In contrast to this, the electron temperature exhibits only a weak variation at varying magnetic field and remains virtually constant between 0 and 10 mT at a value around 6 eV at 0.3 Pa. The evaluation of lateral intensity profiles indicates that the radial distribution of the electron density and temperature within the wave heated discharges remains well comparable to the case of inductive heating.

Also for the wave heated discharges, a virtually identical relative behaviour of all considered parameters is evident for both isotopes. Analogous to ICPs, a higher atomic fraction in deuterium than in hydrogen is observed. Again, this results in a higher electron density and a higher RF power transfer efficiency for  $\text{D}_2$ . Depending on the magnetic field, a comparable behaviour of the atomic fraction is observed for both isotopes: with respect to the case of 0 mT, it remains virtually constant or even decreases if a magnetic field is applied. This behaviour indicates that the probability for the surface recombination of atoms at the plasma chamber walls has to increase by about a factor of 3 in the presence of a magnetic field. Based on the available experimental data, the reason behind this observation cannot be positively explained yet.

In order to allow for a direct comparison to the ICPs driven at 1 MHz, the power dependence of the plasma parameters obtained with the wave heated discharges is evaluated in the range between 0.8 kW and 1.5 kW for both hydrogen and deuterium. This is conducted at the relevant pressure of 0.3 Pa and at a magnetic field of 8 mT, where the local maximum of the RF power transfer efficiency is observed.

With increasing delivered power, **the RF power transfer efficiency of the wave heated discharges saturates around 60 % in deuterium and around 50 % in hydrogen. This is a considerably lower efficiency than observed for the ICPs**, where more than 90 % in  $\text{D}_2$  and more than 70 % in  $\text{H}_2$  are achieved at the same RF power. In parallel, the measured electron densities are increasing monotonously. Maximum densities of  $6.5 \times 10^{17} \text{ m}^{-3}$  in  $\text{H}_2$  and of almost  $10^{18} \text{ m}^{-3}$  in  $\text{D}_2$  are achieved with the Nagoya antenna. **Compared to the ICPs, the electron density is enhanced by a factor of 2 in deuterium and by factor of 3 in hydrogen.** With the Nagoya antenna, the density ratio of atoms and molecules is virtually constant in hydrogen around 0.5 and increases slightly from 0.6 to 0.8 in deuterium. For the ICPs, virtually the same ( $\text{H}_2$ ) or slightly higher ( $\text{D}_2$ ) atomic fractions are achieved at the same conditions.

Consequently, the presently performed first direct comparison of both discharge types in H<sub>2</sub>/D<sub>2</sub> revealed that the most prominent potential benefit of wave heated discharges appears to be the enhanced electron density. For the present experimental setup, it is roughly estimated that **an inductively heated plasma would require at least 2.5 times more RF power in deuterium in order to reach the density level which is achieved with the wave heated discharges.** In hydrogen, an even higher factor around 4 is approximated. This appears as a very promising feature in view of an envisaged lower power consumption of ion sources for NNBI at DEMO. However, a possibly reduced overall power consumption of wave heated discharges comes at the price of higher ohmic losses within the RF circuit. **If the same electron density is reached with both discharge types, the RF power losses with the Nagoya antenna are up to 2.5 times higher than estimated for the ICP.** This requires for increased cooling measures and may negatively affect the reliability of the RF system.

**Based on these results, it is suggested that wave heated discharges are considered for further investigations.** In course of these studies, the main differences between the presently applied laboratory setup and large ion sources need to be addressed: the effects of a Faraday shield - which is a prerequisite at large ion sources to protect the dielectric vessel - and the discharge operation at larger plasma volume and higher RF power. While a Faraday shield can still be tested at a laboratory setup in principle, the higher power operation has to be studied directly at a large ion source test bed.

## Bibliography

- [AJS<sup>+</sup>15] A.D. Ash, T.T.C. Jones, E. Surrey, et al., *JET neutral beam duct Optical Interlock*, Fusion Engineering and Design **96-97** (2015), 396 – 399.
- [Bac06] M. Bacal, *Physics aspects of negative ion sources*, Nuclear Fusion **46** (2006), 250 – 259.
- [BC97a] D. Blackwell and F.F. Chen, *Two-dimensional imaging of a helicon discharge*, Plasma Sources Science and Technology **6** (1997), 569.
- [BC97b] R.W. Boswell and F.F. Chen, *Helicons - the early years*, IEEE Transactions on Plasma Science **25** (1997), 1229–1244.
- [BCS<sup>+</sup>12] B.D. Blackwell, J.F. Caneses, C.M. Samuell, et al., *Design and characterization of the Magnetized Plasma Interaction Experiment (MAGPIE): a new source for plasma-material interaction studies*, Plasma Sources Science and Technology **21** (2012), 055033.
- [Beh91] K. Behringer, *Diagnostics and modelling of ecrh microwave discharges*, Plasma Physics and Controlled Fusion **33** (1991), 997.
- [Bel72] A.T. Bell, *A model for the dissociation of hydrogen in an electric discharge*, Industrial & Engineering Chemistry Fundamentals **11** (1972), 209–215.
- [Ber05] P.F. Bernath, *Spectra of Atoms and Molecules*, 2nd ed., Oxford University Press, New York, NY, 2005.
- [BGR<sup>+</sup>16] S. Briefi, P. Gutmann, D. Rauner, et al., *Comparison of the B field dependency of plasma parameters of a weakly magnetized inductive and Helicon hydrogen discharge*, Plasma Sources Science and Technology **25** (2016), 035015.

- [Bit04] J.A. Bittencourt, *Fundamentals of plasma physics*, Springer, New York, NY, 2004.
- [BMR<sup>+</sup>17] S. Briefi, S. Mattei, D. Rauner, et al., *Experimental benchmark of the NINJA code for application to the Linac4 H<sup>-</sup> ion source plasma*, New Journal of Physics **19** (2017), 105006.
- [BPS75] K.H. Berkner, R.V. Pyle, and J.W. Stearns, *Intense, mixed-energy hydrogen beams for CTR injection*, Nuclear Fusion **15** (1975), 249 – 254.
- [BRF17] S. Briefi, D. Rauner, and U. Fantz, *Determination of the rotational population of H<sub>2</sub> and D<sub>2</sub> including high-N states in low temperature plasmas via the Fulcher– $\alpha$  transition*, Journal of Quantitative Spectroscopy and Radiative Transfer **187** (2017), 135 – 144.
- [Bri11] S. Briefi, *Spectroscopic Investigation of Indium Halides as Substitutes of Mercury in Low Pressure Discharges for Lighting Applications*, Dissertation, Universität Augsburg, 2011.
- [Bri17] S. Briefi, *Private communication*, Universität Augsburg, AG Experimentelle Plasmaphysik / Max-Planck-Institut für Plasmaphysik, Augsburg, 2017.
- [CB97] F.F. Chen and R.W. Boswell, *Helicons - the past decade*, IEEE Transactions on Plasma Science **25** (1997), 1245–1257.
- [CB99] F.F. Chen and D.D. Blackwell, *Upper Limit to Landau Damping in Helicon Discharges*, Phys. Rev. Lett. **82** (1999), 2677–2680.
- [CB11] P. Chabert and N. Braithwaite, *Physics of Radio-Frequency Plasmas*, Cambridge University Press, Cambridge, 2011.
- [CB16] J.F. Caneses and B.D. Blackwell, *Collisional damping of helicon waves in a high density hydrogen linear plasma device*, Plasma Sources Science and Technology **25** (2016), 055027.
- [CEZ65] Francis F. Chen, John D. Evans, and Wade Zawalski, *Electric probes*, ch. 4, pp. 113–199, Academic Press, 1965.

- [Cha87] P.J. Chantry, *A simple formula for diffusion calculations involving wall reflection and low density*, Journal of Applied Physics **62** (1987), 1141–1148.
- [Che91] F.F. Chen, *Plasma ionization by helicon waves*, Plasma Physics and Controlled Fusion **33** (1991), 339.
- [Che92] ———, *Experiments on helicon plasma sources*, Journal of Vacuum Science & Technology A: Vacuum, Surfaces, and Films **10** (1992), 1389–1401.
- [Che15] ———, *Helicon discharges and sources: a review*, Plasma Sources Science and Technology **24** (2015), 014001.
- [Cho06] S. Cho, *The resistance peak of helicon plasmas at low magnetic fields*, Physics of Plasmas **13** (2006), 033504.
- [Chr88] K. Christmann, *Interaction of hydrogen with solid surfaces*, Surface Science Reports **9** (1988), 1–163.
- [Dem13] W. Demtröder, *Experimentalphysik 2, Elektrizität und Optik*, Springer, Heidelberg Berlin, 2013.
- [Die58] G.H. Dieke, *The molecular spectrum of hydrogen and its isotopes*, Journal of Molecular Spectroscopy **2** (1958), 494 – 517.
- [DJB<sup>+</sup>96] A.W. Degeling, C.O. Jung, R.W. Boswell, et al., *Plasma production from helicon waves*, Physics of Plasmas **3** (1996), 2788–2796.
- [EB04] M. Edamura and E.C. Benck, *Effects of voltage distribution along an induction coil and discharge frequency in inductively coupled plasmas*, Journal of Vacuum Science & Technology A: Vacuum, Surfaces, and Films **22** (2004), 293–301.
- [FAA<sup>+</sup>17] T. Franke, P. Agostinetti, K. Avramidis, et al., *Heating & current drive efficiencies, TBR and RAMI considerations for DEMO*, Fusion Engineering and Design **123** (2017), 495–499.
- [FAF<sup>+</sup>17] I. Furno, R. Agnello, U. Fantz, et al., *Helicon wave-generated plasmas for negative ion beams for fusion*, EPJ Web Conf. **157** (2017), 03014.

- [FBB<sup>+</sup>15] T. Franke, E. Barbato, G. Bosia, et al., *Technological and physics assessments on heating and current drive systems for demo*, Fusion Engineering and Design **96** (2015), 468 – 472.
- [FBB<sup>+</sup>16] G. Federici, C. Bachmann, W. Biel, et al., *Overview of the design approach and prioritization of R&D activities towards an EU DEMO*, Fusion Engineering and Design **109** (2016), 1464 – 1474.
- [FF13] U. Fantz and P. Franzen, *Feasibility and R&D Needs of a Negative Ion Based Neutral Beam System for DEMO*, 24th IAEA Fusion Energy Conference (USA), International Atomic Energy Agency (2013).
- [FFF<sup>+</sup>06] U. Fantz, H. Falter, P. Franzen, et al., *Spectroscopy - a powerful diagnostic tool in source development*, Nuclear Fusion **46** (2006), 297–306.
- [FH98] U. Fantz and B. Heger, *Spectroscopic diagnostics of the vibrational population in the ground state of H<sub>2</sub> and D<sub>2</sub> molecules*, Plasma Physics and Controlled Fusion **40** (1998), 2023–2032.
- [FHF<sup>+</sup>18] U. Fantz, C. Hopf, R. Friedl, S. Cristofaro, B. Heinemann, S. Lishev, and A. Mimo, *Technology developments for a beam source of an NNBI system for DEMO*, Fusion Engineering and Design (2018).
- [Fri13] R. Friedl, *Experimental Investigations on the caesium dynamics in H<sub>2</sub>/D<sub>2</sub> low temperature plasmas*, Dissertation, Universität Augsburg, 2013.
- [Fru09] A. Fruchtman, *Ambipolar and nonambipolar cross-field diffusions*, Plasma Sources Science and Technology **18** (2009), 025033.
- [FSC85] R.S. Freund, J.A. Schiavone, and H.M. Crosswhite, *The Electronic Spectrum and Energy Levels of the Deuterium Molecule*, Journal of Physical and Chemical Reference Data **14** (1985), 235–383.
- [FSW<sup>+</sup>13] U. Fantz, L. Schiesko, D. Wunderlich, et al., *A comparison of hydrogen and deuterium plasmas in the IPP prototype ion source for fusion*, AIP Conference Proceedings **1515** (2013), 187–196.

- [FW06] U. Fantz and D. Wunderlich, *Franck-Condon factors, transition probabilities, and radiative lifetimes for hydrogen molecules and their isotopomers*, Atomic Data and Nuclear Data Tables **92** (2006), 853–973.
- [GCR<sup>+</sup>17] R.H. Goulding, J.B.O. Caughman, J. Rapp, et al., *Progress in the Development of a High Power Helicon Plasma Source for the Materials Plasma Exposure Experiment*, Fusion Science and Technology **72** (2017), 588–594.
- [GJL<sup>+</sup>59] M. Green, K.R. Jennings, J.W. Linnett, et al., *Recombination of atoms at surfaces. Part 7.-Hydrogen atoms at silica and other similar surfaces*, Trans. Faraday Soc. **55** (1959), 2152–2161.
- [GMS95] V.A. Godyak, V.P. Meytlis, and H.R. Strauss, *Tonks-Langmuir problem for a bi-Maxwellian plasma*, Plasma Science, IEEE Transactions on **23** (1995), 728–734.
- [GP90] V. A. Godyak and R. B. Piejak, *In situ simultaneous radio frequency discharge power measurements*, Journal of Vacuum Science & Technology A **8** (1990), 3833–3837.
- [GPA92] V.A. Godyak, R.B. Piejak, and B.M. Alexandrovich, *Measurement of electron energy distribution in low-pressure RF discharges*, Plasma Sources Science and Technology **1** (1992), 36–58.
- [GPA99] V.A. Godyak, R.B. Piejak, and B.M. Alexandrovich, *Experimental setup and electrical characteristics of an inductively coupled plasma*, Journal of Applied Physics **85** (1999), 703–712.
- [Gut14] P. Gutmann, *Vergleich zylindrischer Wasserstoffplasmen ( $H_2$ ,  $D_2$ ) im ICP- und Helikon-Setup*, Master thesis, Universität Augsburg, 2014.
- [HDG<sup>+</sup>09] R. Hemsworth, H. Decamps, J. Graceffa, et al., *Status of the ITER heating neutral beam system*, Nuclear Fusion **49** (2009), 045006.
- [Her50] G. Herzberg, *Molecular spectra and molecular structure, I. Spectra of diatomic molecules*, 2nd ed., D. van Nostrand Company, New York, NY, 1950.

- [HK81] J. Harris and B. Kasemo, *On precursor mechanisms for surface reactions*, Surface Science **105** (1981), L281 – L287.
- [Hop94] J. Hopwood, *Planar RF induction plasma coupling efficiency*, Plasma Sources Science and Technology **3** (1994), 460–466.
- [Hor83] C. M. Horwitz, *Radio frequency sputtering and the significance of power input*, Journal of Vacuum Science & Technology A **1** (1983), 1795–1800.
- [IAE02] IAEA, *ITER technical basis*, ITER EDA documentation series 24, International Atomic Energy Agency, Vienna (2002).
- [IKS92] J.D. Isenberg, H.J. Kwon, and M. Seidl, *Surface production of  $H^-$  ions by backscattering of  $H^+$  and  $H_2^+$  ions in the 3-50 eV ion energy range*, AIP Conference Proceedings **287** (1992), 38–47.
- [Iti74] Y. Itikawa, *Momentum-transfer cross sections for electron collisions with atoms and molecules*, Atomic Data and Nuclear Data Tables **14** (1974), 1 – 10.
- [Jac99] J.D. Jackson, *Classical electrodynamics*, Wiley, New York, NY, 3<sup>rd</sup> edition, 1999.
- [JLE<sup>+</sup>87] R.K. Janev, W.D. Langer, K. Evans, et al., *Elementary processes in hydrogen-helium plasmas: cross sections and reaction rate coefficients*, vol. 4, Springer, Berlin, 1987.
- [JM50] E.O. Johnson and L. Malter, *A floating double probe method for measurements in gas discharges*, Phys. Rev. **80** (1950), 58–68.
- [JRS03] R.K. Janev, D. Reiter, and U. Samm, *Report Jül-4105*, Forschungszentrum Jülich (2003), Available online: [www.eirene.de/report\\_4105.pdf](http://www.eirene.de/report_4105.pdf) (accessed on 09 December 2017).
- [KB91] Y.C. Kim and M. Boudart, *Recombination of oxygen, nitrogen, and hydrogen atoms on silica: kinetics and mechanism*, Langmuir **7** (1991), 2999–3005.

- [KB96] I.V. Kamenski and G.G. Borg, *An evaluation of different antenna designs for helicon wave excitation in a cylindrical plasma source*, Physics of Plasmas **3** (1996), 4396–4409.
- [Kov69] I. Kovács, *Rotational structure in the spectra of diatomic molecules*, Adam Hilger, London, 1969.
- [Kra08] E. A. Kralkina, *Low-pressure radio-frequency inductive discharge and possibilities of optimizing inductive plasma sources*, Physics-Uspekhi **51** (2008), 493.
- [KRP<sup>+</sup>16] E.A. Kralkina, A.A. Rukhadze, V.B. Pavlov, et al., *RF power absorption by plasma of a low-pressure inductive discharge*, Plasma Sources Science and Technology **25** (2016), 015016.
- [KRR18] A. Kramida, Y. Ralchenko, and J. Reader, and NIST ASD Team, NIST Atomic Spectra Database (ver. 5.5.2), National Institute of Standards and Technology, Gaithersburg, MD., Online Available: <https://physics.nist.gov/asd> , 2018.
- [KS98] P.S. Krstic and D.R. Schultz, *Atomic and plasma-material interaction data for fusion 8*, International Atomic Energy Agency, Vienna, 1998.
- [LBB<sup>+</sup>91] P.K. Loewenhardt, B.D. Blackwell, R.W. Boswell, et al., *Plasma production in a toroidal heliac by helicon waves*, Phys. Rev. Lett. **67** (1991), 2792–2794.
- [Lid05] D.R. Lide (ed.), *CRC Handbook of Chemistry and Physics*, CRC Press, Boca Raton, FL, 2005.
- [LL05] M.A. Lieberman and A.J. Lichtenberg, *Principles of plasma discharges and materials processing, 2nd edition*, John Wiley & Sons, Hoboken, New Jersey, 2005.
- [LS92] B.S. Lee and M. Seidl, *Surface production of  $H^-$  ions by hyperthermal hydrogen atoms*, Applied Physics Letters **61** (1992), 2857–2859.
- [MAD<sup>+</sup>17] C. Marini, R. Agnello, B.P. Duval, et al., *Spectroscopic characterization of  $H_2$  and  $D_2$  helicon plasmas generated by a resonant antenna for neutral beam applications in fusion*, Nuclear Fusion **57** (2017), 036024.

- [Mat17] S. Mattei, *H<sup>-</sup> ion source for CERN's Linac4 accelerator: simulation, experimental validation and optimization of the hydrogen plasma*, Dissertation, Swiss Plasma Center, Ecole Polytechnique Federale de Lausanne, 2017.
- [McA14] Roy McAdams, *Beyond ITER: Neutral beams for a demonstration fusion reactor (DEMO)(invited)*, Review of Scientific Instruments **85** (2014), 02B319.
- [MDCK<sup>+</sup>09] P. McNeely, S.V. Dudin, S. Christ-Koch, et al., *A Langmuir probe system for high power RF-driven negative ion sources on high potential*, Plasma Sources Science and Technology **18** (2009), 014011.
- [MDZ99] M. Mozetič, M. Drobnič, and A. Zalar, *Recombination of neutral hydrogen atoms on AISI 304 stainless steel surface*, Applied Surface Science **144-145** (1999), 399 – 403.
- [MER97] A.W. Molvik, A.R. Ellingboe, and T.D. Rognlien, *Hot-Electron Production and Wave Structure in a Helicon Plasma Source*, Phys. Rev. Lett. **79** (1997), 233–236.
- [MHL77] G.R. Möhlmann, F.J. De Heer, and J. Los, *Emission cross sections of balmer- $\alpha, \beta, \gamma$  radiation for electrons (0-2000 eV) on H2 and D2*, Chemical Physics **25** (1977), 103 – 116.
- [MM71] G.A. Melin and R.J. Madix, *Energy accommodation during hydrogen atom recombination on metal surfaces*, Trans. Faraday Soc. **67** (1971), 2711–2719.
- [MM88] E.A. Mason and E.W. McDaniel, *Transport properties of ions in gases*, John Wiley & Sons, Inc, New York, 1988.
- [MNO<sup>+</sup>17] S. Mattei, K. Nishida, M. Onai, et al., *A fully-implicit Particle-In-Cell Monte Carlo Collision code for the simulation of inductively coupled plasmas*, Journal of Computational Physics **350** (2017), 891 – 906.
- [Möl93] W. Möller, *Plasma and surface modeling of the deposition of hydrogenated carbon films from low-pressure methane plasmas*, Applied Physics A **56** (1993), 527–546.

- [MSL26] H.M. Mott-Smith and I. Langmuir, *The theory of collectors in gaseous discharges*, Phys. Rev. **28** (1926), 727–763.
- [MTG72] W.T. Miles, R. Thompson, and A.E.S. Green, *Electron-Impact Cross Sections and Energy Deposition in Molecular Hydrogen*, Journal of Applied Physics **43** (1972), 678–686.
- [MW<sup>+</sup>11] P. McNeely, D. Wunderlich, et al., *Neutral depletion in an  $H^-$  source operated at high RF power and low input gas flow*, Plasma Sources Science and Technology **20** (2011), 045005.
- [OOR<sup>+</sup>89] D.K. Otorbaev, V.N. Ochkin, P.L. Rubin, et al., *Electron-impact excitation levels of the rotational levels of molecular electron states in gas discharges*, in: Electron-excited Molecules in Nonequilibrium Plasma (N. N. Sobolev, ed.), Nova Science Publishers, Commack, NY (1989).
- [PGA92] R.B. Piejak, V.A. Godyak, and B.M. Alexandrovich, *A simple analysis of an inductive RF discharge*, Plasma Sources Science and Technology **1** (1992), 179.
- [Phe90] A.V. Phelps, *Cross Sections and Swarm Coefficients for  $H^+$ ,  $H_2^+$ ,  $H_3^+$ ,  $H$ ,  $H_2$ , and  $H^-$  in  $H_2$  for Energies from 0.1 eV to 10 keV*, Journal of Physical and Chemical Reference Data **19** (1990), 653–675.
- [PT01] S. Pfau and M. Tichy, *Langmuir probe diagnostics of low-temperature plasmas*, Wiley-VCH, Berlin, 2001.
- [RBB<sup>+</sup>12] F. Romanelli, P. Barabaschi, D. Borba, et al., *Fusion electricity - a roadmap to the realisation of fusion energy*, European Fusion Development Agreement (EFDA) (2012).
- [RBF17] D. Rauner, S. Briefi, and U. Fantz, *RF power transfer efficiency of inductively coupled low pressure  $H_2$  and  $D_2$  discharges*, Plasma Sources Science and Technology **26** (2017), 095004.
- [SAB<sup>+</sup>16] A. Simonin, R. Agnello, S. Bechu, et al., *Negative ion source development for a photoneutralization based neutral beam system for future fusion reactors*, New Journal of Physics **18** (2016), 125005.

- [SAB<sup>+</sup>17] P. Sonato, P. Agostinetti, T. Bolzonella, et al., *Conceptual design of the DEMO neutral beam injectors: main developments and R&D achievements*, Nuclear Fusion **57** (2017), 056026.
- [SBJ<sup>+</sup>12] E. Surrey, A. Benn, I. Jenkins, et al., *The influence of neutral beam optimization for DEMO on injector design*, Fusion Engineering and Design **87** (2012), 373 – 383.
- [SCF<sup>+</sup>99] E. Speth, M. Ciric, J.H. Feist, et al., *Rf ion sources for fusion applications: design, development and performance*, Fusion Engineering and Design **46** (1999), 383 – 388.
- [SCI<sup>+</sup>96] M. Seidl, H.L. Cui, J.D. Isenberg, et al., *Negative surface ionization of hydrogen atoms and molecules*, Journal of Applied Physics **79** (1996), 2896–2901.
- [SCM<sup>+</sup>07] M. Shimada, D.J. Campbell, V. Mukhovatov, et al., *Progress in the ITER Physics Basis, Chapter 1: Overview and summary*, Nuclear Fusion **47** (2007), S1–S17.
- [SEG87] M.B. Shah, D.S. Elliott, and H.B. Gilbody, *Pulsed crossed-beam study of the ionisation of atomic hydrogen by electron impact*, Journal of Physics B: Atomic and Molecular Physics **20** (1987), 3501.
- [Sei17] D. Seibold, *Automatisierung des Messverfahrens zur Bestimmung der Kopplungseffizienz in induktiven HF-Plasmen*, Bachelor thesis, Universität Augsburg, 2017.
- [SFF<sup>+</sup>06] E. Speth, H.D. Falter, P. Franzen, et al., *Overview of the RF source development programme at IPP Garching*, Nuclear Fusion **46** (2006), S220.
- [Sha70] T.E. Sharp, *Potential-energy curves for molecular hydrogen and its ions*, Atomic Data and Nuclear Data Tables **2** (1970), 119–169.
- [Sha71] ———, *Erratum: Potential-energy curves for molecular hydrogen and its ions*, Atomic Data and Nuclear Data Tables **3** (1971), 299.
- [SL49] K.E. Shuler and K.J. Laidler, *The Kinetics of Heterogeneous Atom and Radical Reactions. I. The Recombination of Hydrogen Atoms on Surfaces*, The Journal of Chemical Physics **17** (1949), 1212–1217.

- [SMF<sup>+</sup>12] L. Schiesko, P. McNeely, P. Franzen, et al., *Magnetic field dependence of the plasma properties in a negative hydrogen ion source for fusion*, Plasma Physics and Controlled Fusion **54** (2012), 105002.
- [SMO<sup>+</sup>15] J. Santoso, R. Manoharan, S. O’Byrne, et al., *Negative hydrogen ion production in a helicon plasma source*, Physics of Plasmas **22** (2015), 093513.
- [SNO<sup>+</sup>98] K. Suzuki, K. Nakamura, H. Ohkubo, et al., *Power transfer efficiency and mode jump in an inductive RF discharge*, Plasma Sources Science and Technology **7** (1998), 13.
- [ST96] K.P. Shamrai and V.B. Taranov, *Volume and surface rf power absorption in a helicon plasma source*, Plasma Sources Science and Technology **5** (1996), 474.
- [Sti92] T.H. Stix, *Waves in plasmas*, Springer, New York, 1992.
- [TL29] L. Tonks and I. Langmuir, *A General Theory of the Plasma of an Arc*, Phys. Rev. **34** (1929), 876–922.
- [TS63] T. Takaishi and Y. Sensui, *Thermal transpiration effect of hydrogen, rare gases and methane*, Transactions of the Faraday Society **59** (1963), 2503–2514.
- [TT02a] C.S. Trevisan and J. Tennyson, *Calculated rates for the electron impact dissociation of molecular hydrogen, deuterium and tritium*, Plasma Physics and Controlled Fusion **44** (2002), 1263.
- [TT02b] ———, *Calculated rates for the electron impact dissociation of molecular hydrogen: mixed isotopomers and scaling laws*, Plasma Physics and Controlled Fusion **44** (2002), 2217.
- [Tur93] M.M. Turner, *Collisionless electron heating in an inductively coupled discharge*, Phys. Rev. Lett. **71** (1993), 1844–1847.
- [VLD<sup>+</sup>95] V. Vahedi, M.A. Lieberman, G. DiPeso, et al., *Analytic model of power deposition in inductively coupled plasma sources*, Journal of Applied Physics **78** (1995), 1446–1458.
- [Wei67] E.S. Weibel, *Anomalous Skin Effect in a Plasma*, The Physics of Fluids **10** (1967), 741–748.

- [WF16] D. Wunderlich and U. Fantz, *Evaluation of State-Resolved Reaction Probabilities and Their Application in Population Models for He, H, and H<sub>2</sub>*, *Atoms* **4** (2016), 26.
- [WGF09] D. Wunderlich, R. Gutser, and U. Fantz, *PIC code for the plasma sheath in large caesiated RF sources for negative hydrogen ions*, *Plasma Sources Science and Technology* **18** (2009), 045031.
- [WHK<sup>+</sup>78] T. Watari, T. Hatori, R. Kumazawa, et al., *Radio-frequency plugging of a high density plasma*, *The Physics of Fluids* **21** (1978), 2076–2081.
- [WSM<sup>+</sup>12] D. Wunderlich, L. Schiesko, P. McNeely, et al., *On the proton flux toward the plasma grid in a RF-driven negative hydrogen ion source for ITER NBI*, *Plasma Physics and Controlled Fusion* **54** (2012), 125002.
- [WW61] B.J. Wood and H. Wise, *Kinetics of hydrogen atom recombination on surfaces*, *The Journal of Physical Chemistry* **65** (1961), 1976–1983.
- [WW62] ———, *The kinetics of hydrogen atom recombination on pyrex glass and fused quartz*, *The Journal of Physical Chemistry* **66** (1962), 1049–1053.
- [YKK<sup>+</sup>10] J.-S. Yoon, Y.-W. Kim, D.-C. Kwon, et al., *Electron-impact cross sections for deuterated hydrogen and deuterium molecules*, *Reports on Progress in Physics* **73** (2010), 116401.
- [YSH<sup>+</sup>08] J.-S. Yoon, M.-Y. Song, J.-M. Han, et al., *Cross Sections for Electron Collisions with Hydrogen Molecules*, *Journal of Physical and Chemical Reference Data* **37** (2008), 913–931.
- [ZB91] P. Zhu and R.W. Boswell, *Observation of nonthermal electron tails in an rf excited argon magnetoplasma*, *Physics of Fluids B: Plasma Physics* **3** (1991), 869–874.
- [Zie17] D. Zielke, *Simulation of inductive RF coupling in a low pressure low temperature hydrogen plasma*, Master thesis, Universität Augsburg, 2017.
- [Zim00] G. Zimmer, *Hochfrequenztechnik*, Springer, Berlin Heidelberg, 2000.

# Acknowledgements

Hiermit möchte ich mich bei allen bedanken, die zum Entstehen dieser Arbeit beigetragen haben. Insbesondere gilt mein Dank:

- Frau **Prof. Dr.-Ing. Ursel Fantz** für die Möglichkeit, diese Doktorarbeit in der AG Experimentelle Plasmaphysik bzw. am Max-Planck-Institut für Plasmaphysik durchzuführen, sowie für das hohe Niveau der wissenschaftlichen Ausbildung und die hervorragende Betreuung während der gesamten Arbeit.
- Herrn **Prof. Dr. Wolfgang Brütting** für die Übernahme des Zweitgutachtens.
- Herrn **Dr. Stefan Briefi** für die hervorragende, motivierende und lehrreiche Unterstützung, die großartige und freundschaftliche Zusammenarbeit, die vielen spannenden Diskussionen und nicht zuletzt für das Korrekturlesen der Arbeit in einer für dich/euch ohnehin schon sehr spannenden und (erfreulich) ereignisreichen Zeit. Auf diesem Wege, euch allen weiterhin nur das Beste!!
- den Herren **Dr. Roland Friedl** und **Dr. Uwe Kurutz** für die großartige, freundschaftliche, erfahrungs- und lehrreiche Zusammenarbeit und die vielen wissenschaftlichen (und unwissenschaftlichen) Diskussionen im Laufe der vergangenen Jahre.
- allen weiteren aktuellen und ehemaligen Mitgliedern der AG Experimentelle Plasmaphysik, insbesondere den Damen **Sofia Cristofaro** und **Caecilia Fröhler** sowie den Herren **Adrian Heiler**, **Frederick Merk**, **Dominik Seibold** und **Dominikus Zielke** für die großartige und freundschaftliche Zusammenarbeit und tatkräftige Unterstützung.
- dem gesamten ITED-NNBI-Team für die gute Zusammenarbeit und stetige Unterstützung und Hilfsbereitschaft, insbesondere den Herren **Bernd Heinemann**, **Dr. Werner Kraus**, **Dr. Christian Wimmer**, und **Dr. Dirk Wunderlich**.
- der **feinmechanischen Werkstatt** und der **Elektronikwerkstatt** des Physik-Instituts für die Unterstützung und die Herstellung zahlreicher Komponenten.

Im Besonderen möchte ich mich schließlich noch bei meiner Familie bedanken, ohne deren Unterstützung mein gesamtes Studium und somit auch diese Arbeit gar nicht möglich gewesen wären. Zu guter Letzt - aber nicht minder wichtig - danke ich meiner Freundin. Deine verständnisvolle Unterstützung und Geduld, speziell während der letzten Monate, waren und sind mir ein großartiger Rückhalt.